FACULTY OF SCIENCES

EMERGENT COLLECTIVE MOTION FROM LOCAL INTERACTIONS

Corneel Casert

Department of Physics and Astronomy

Academic Year 2016-2017

Promotor: Prof. Dr. Jan Ryckebusch
Supervisor: Andrés Belaza

Thesis submitted for the degree of
Master of Science in Physics and Astronomy

GHENT UNIVERSITY

First, a heartfelt thanks to professor Ryckebusch for giving me the opportunity to work on this project, and for the assistance he has given me throughout this semester.

Andrés, thank you for your guidance, steadfast support – and the many amicable chats in between.

Olivier, thanks for standing by me and for your backing throughout.

To my sister and parents, thanks for all the support you've given me over the past 5 years and for proofreading this work.

Contents

1 Introduction

1.1 Complexity and Emergent Collective Behaviour

Complexity describes how, for some systems, local interactions between the parts can account for emergent global behaviour [BY02]. In general, a complex system consists of many components that interact with one another locally. Rather than being governed by a central mechanism, the behaviour of complex systems follows out of the interactions between the parts and with the environment. Complex systems are often non-linear so that small changes in their state can have a drastic effect on their behaviour [Cha01]. Our world is rife with examples of complex systems: neural systems, social media, human cultures, stock markets and so on [Say15].

For a system to be complex, it must show emergent behaviour. Emergence connects the relation between properties of the system on different scales – the macroscopic behaviour of a complex system cannot be predicted from the behaviour of every component in isolation. The whole is more than the sum of its parts. Complex systems often self-organize, as they spontaneously order themselves and often display a certain symmetry. Examples of emergent behaviour are ant colonies, consciousness emerging from the interaction of neurons, ecosystems, traffic patterns and – the topic of this work – collective motion [Cha01].

1.2 Phase Transitions

The theory of phase transitions describes how a system changes its properties as it goes to a different phase under the influence of an external process. The best-known example is the transition from the solid to liquid to gas phase in a material as a result of changes in temperature and/or pressure. Many physicists are also well-acquainted with the phase transition between order and disorder in ferromagnetic models such as the Ising model. In general, a

phase transition can be described by an order and a control parameter. The former is used to characterize the nature of the phase transition and should be markedly different for both phases. The order parameter is often defined so that it is zero in one phase and non-zero in the other phase. Common examples of order parameters are the average magnetization per spin in the Ising model and the difference between liquid and gas density in the liquid-gas transition. The control parameter is the external variable that determines the phase of the system, e.g. the temperature in the Ising model. Around the transition point – where the change in the a system's phase occurs –, a small change in the control parameter can drastically change the physical properties, as well as the symmetry, of the system.

A phase transition is categorized depending on how the order parameter changes between the two phases. If the change is continuous, the transition is said to be a "second-order" (or continuous) transition. On the other hand, if the order parameter has a discontinuity at the transition point, the transition is "first-order" (or discontinuous). Both phases coexist at this point. Assessing whether a phase transition is continuous or discontinuous is often hampered by the limited size of systems under study. If this is the case, one has to resort to measuring functions derived from the order parameter.

1.3 Collective Motion

Collective motion is ubiquitous in nature. One of the most eye-catching examples is the formation of murmurations, in which thousands of starlings flock together (Fig. 1.1a). Birds in such a flock collectively make the decision to change their direction or land to feed. Fish can form highly mobile schools to evade nearby predators (Fig. 1.1b). Another notable example is the mass migration of insects such as locusts (Fig. 1.1c). This kind of collective behaviour is also observed in humans – pedestrian behaviour, car traffic and even heavy metal fans [Sil+13] are all examples. However, collective motion is not limited to the animal kingdom: bacterial colonies, such as E. coli (Fig. 1.1d), and other types of cells also display it. The observation of collective motion in *non-living* systems is even more astonishing. For instance, collective motion is observed in self-propelled particles such as light-powered micromotors in water [Ibe+09] and in vibrated granular rods [Bla+03].

(a)

(b)

(c)

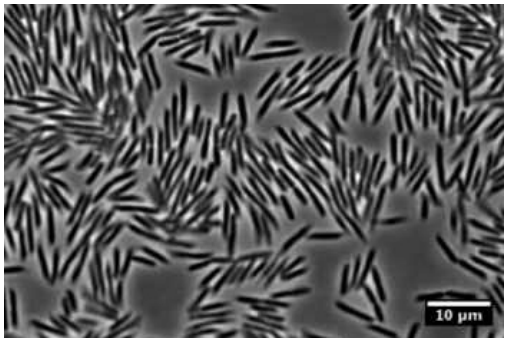

(d)

Fig. 1.1.: Examples of systems displaying collective motion: (a) the flocking of starlings, (b) a school of yellowstripe scad, (c) a locust swarm, (d) an E. coli colony.

The origin of the establishment of collective motion is different in each of these examples. Units can form groups out of self-defence, for improved decision making or more efficient exploration [VZ12]. While interesting in its own right, if the patterns of motion would be distinct for every example mentioned previously, the system-specific study of them would perhaps be better suited to specialized branches of biology, sociology or chemistry. One could think that the establishment of collective motion is dependent on the collective goal, the way of communication and information transfer between the units, the nature of the interactions and so on.

Surprisingly, observations indicate that – even though the systems studied here are so different – the patterns of collective motion can be divided into a few distinct regimes, which makes the study of collective motion attractive to physicists [Vic08]. Following a bottom-up approach, a more general underlying mechanism could explain why the same patterns are observed on such different size scales. The search for an explanation of this apparently

universal behaviour has led to the creation of a great many models over the past decades, some of which are discussed in the following section.

1.4 Modelling Approaches

The Lagrangian (or individual-based) approach is a natural way of modelling a phenomenon that occurs due to the interaction between many particles. It is important to mention that obtaining analytical results is very difficult with this method, and one has to resort to extensive numerical studies. These are often computationally expensive and not always optimal to gain a deep understanding of the general behaviour of the system [RSG12]. Because of this, mesoscopic descriptions have been attempted for collective motion, relying on models of hydrodynamics. Though they are more rigorous, the possible analytical deductions for a complex system are limited.

While the units involved can appear to be quite simple, setting up a detailed and faithful model is still incredibly complicated. Instead, to study collective motion a minimal model is employed. This is a model with as little detail as possible, only equipped with the basic features to produce collective motion [Gré+03; Gin16]. Such a model is optimal for studying the behaviour at large wavelengths and frequencies.

Most models for collective motion involve a 'social' force, which aligns a particle's velocity with the average velocity of the particles in its neighbourhood. This neighbourhood can either be the metric or the topological neighbourhood. With a metric neighbourhood, particles only interact with others if they are within a certain distance of each other. In the most common implementation of the topological neighbourhood, every particle interacts with a fixed amount of neighbouring particles.

The first popular model implementing such an alignment rule was the "boids" model (short for bird-oid object) by Craig Reynolds that aimed to capture the motion patterns of small flocks of birds [Rey87]. The boids in this model move according to three simple rules: they aim to avoid collisions with neighbouring particles, change their velocity to match the velocity of their neighbours and tend to move towards the center-of-mass of the flock to which they belong.

While the boids model, with its three simple rules, already displays the patterns observed in nature, it does not allow for a quantitative study. To this aim, Vicsek et al. established a model following a statistical physics approach, which is now widely known as the Vicsek model [Vic+95]. In this model, particles also align their velocity to the mean velocity of their neighbours, but an additional stochastic component is added to this average. This noise represents the error a unit can make in estimating the average velocity of its neighbours or in choosing its own direction. The competition between the noise and the velocity-aligning force determines whether collective motion can be established in the system. In the absence of noise, the particles will align perfectly. If, on the other hand, the noise is too strong, the particles will not be able to match their velocity, resulting in random movement. As the Vicsek model is central to this thesis, it will be discussed in depth in the following chapter.

Models involving an explicit alignment rule are most common, but it is important to mention that some of the patterns of collective motion can also be found in models where the alignment occurs *indirectly*, for instance in a system of self-propelled particles that are attracted to the center-of-mass of their neighbours [Str11].

The Vicsek Model

2

2.1 Description of the Model

As mentioned in the first chapter, the Vicsek model is a minimal model that was pivotal in the development of the study of collective motion [Vic+95]. The model describes a system consisting of a great many 'active' or self-propelled Brownian particles. Active particles are capable of developing motion, for instance by converting the energy from their surroundings or through an internal mechanism. As a result, they move at an average speed $v_0 \neq 0$. The original Vicsek model studies overdamped active Brownian particles, which means that their speed is the constant v_0.

The particles in this model are subjected to short-range interactions that seek to align the directions of motion to those of the neighbouring particles. Vicsek introduced a 'temperature' component to the model by adding a stochastic element to the alignment interaction between the particles. In the original Vicsek model, which describes a 2D system, the propagation of the particle positions and the directions of their velocity over a time step Δt is given by

$$\begin{aligned} \boldsymbol{x}_i(t + \Delta t) &= \boldsymbol{x}_i(t) + \boldsymbol{v}_i(t)\Delta t, \\ \theta_i(t + \Delta t) &= \langle \theta(t) \rangle_{i,R_0} + \Delta\theta, \end{aligned} \tag{2.1}$$

where the magnitude of the velocity for each particle is equal to v_0 so that $\boldsymbol{v}_i(t) = v_0 e^{i\theta_i(t)}$. Here, $\langle \theta(t) \rangle_{i,R_0}$ is the direction of the average velocity of all the particles within a metric[1] distance R_0 of particle i. The term $\Delta\theta$ denotes the stochastic component of this model. It is a uniformly distributed number within the interval $[-\eta\pi, \eta\pi]$ and represents the error agents make in deciding on their new direction. Note that momentum is not conserved under the alignment interactions. Galilean invariance is broken in the Vicsek model, as the particles are defined to move at a speed v_0 with regard to the reference frame.

[1] Additionally, a topological version of the Vicsek model also exists, with an alternate choice for the definition of the neighbourhood. This is discussed in section 2.7.

The Vicsek model can be defined by only three parameters: the particle density ρ, the speed of the particles v_0 and the magnitude of the noise η. It is essentially the competition between the short-range velocity-aligning 'social' forces and the stochastic element (temperature or noise) that determines which flow regime is observed in the system: randomly moving particles or collective motion. In the absence of noise, the particles align perfectly and the combined macroscopic velocity equals the microscopic velocity. When subjected to strong noise, the particles are unable to align their velocities and follow a random walk. The macroscopic velocity equals zero as the individual microscopic velocities are randomly distributed and cancel each other out. The establishment of collective motion can be studied by measuring the order parameter $\Lambda(t) = \left|\frac{1}{Nv_0}\sum_{i=1}^{N} \boldsymbol{v}_i(t)\right|$. This scalar parameter corresponds to the direction of motion of the flock's center-of-mass. Once the social forces overcome the effect of the noise, spontaneous symmetry breaking occurs as the initially isotropic system develops collective motion and Λ adopts a finite value [Gin16].

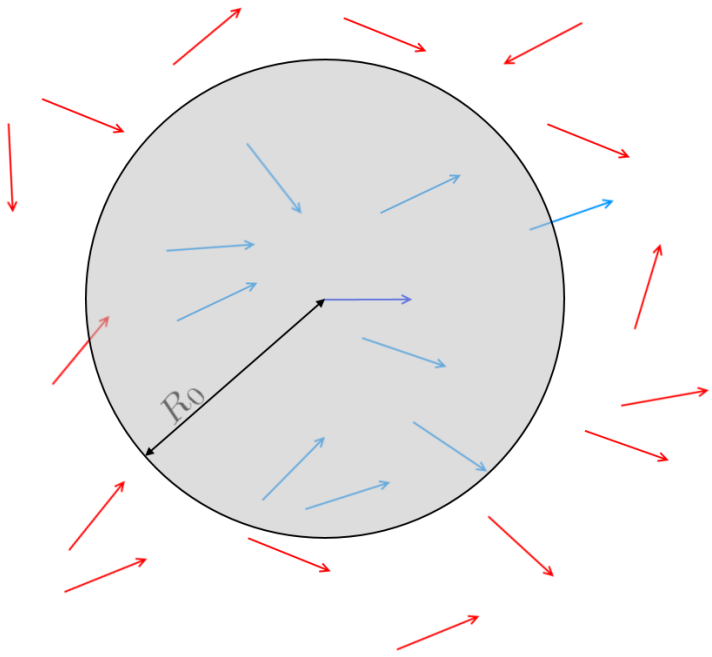

Fig. 2.1.: Representation of the alignment force in the metric Vicsek model: the central particle (dark blue) interacts with every particle in its neighbourhood of radius R_0.

This model is analogous to the spin models of ferromagnetism, albeit in a non-equilibrium situation. The rules to update the direction of motion

in the Vicsek model are similar to the Hamiltonian that aligns the spins in the ferromagnetic systems, and the magnitude of the noise in the Vicsek model can be be related to the temperature in the case of the ferromagnetic equivalent [CV00]. The Vicsek model is closest to the XY model – a lattice model in which the orientation of the spins takes on continuous values and becomes aligned with the orientation of its neighbours. The Hamiltonian for such a 2D system with nearest-neighbour interactions and no external fields is given by [Jen03]

$$\begin{aligned} H &= -J \sum_{\langle i,j \rangle} \boldsymbol{s}_i \cdot \boldsymbol{s}_j \\ &= -J \sum_{\langle i,j \rangle} \cos\left(\theta_i - \theta_j\right), \end{aligned} \tag{2.2}$$

where the summation is over all the neighbouring lattice sites, $\boldsymbol{s}$ is a 2D unit vector, the constant J denotes the strength of the coupling between spins and θ is the angle of the spin. This Hamiltonian tries to align the spins, just like the alignment force in the Vicsek model tries to align the direction of motion of the particles.

The emergence of long-range order in the Vicsek model, present in the collectively moving phase, is not trivial. The Mermin-Wagner Theorem (MWT) states that, in dimensions of two or less, the breaking of a continuous symmetry in an equilibrium system cannot produce long-range order [MW66]. For the Vicsek model, in contrast, the non-equilibrium nature allows for the establishment of collective motion – even in 2D systems. The movement of particles is the only major difference between the Vicsek model and equilibrium spin systems. Hence, the answer as to why long-range order is observed in 2D systems must be explained by it. While theoretical considerations using renormalization groups have accounted for this difference [Ton+05], it is instructive to compare how errors in alignment caused by thermal fluctuations spread throughout the system [Gin16].

With a lattice model, such as the XY model, spreading of the fluctuations is a diffusive process [Gin16]. For such a process in 2D, it can be proven that the correlation between two spins decays algebraically (i.e., like a power-law) to zero with distance, so that long-range order cannot be established. Note that in the 2D XY model, the correlation function decreases like a power-law with distance for a set of temperature values. The system is then said to be quasi-ordered. On the other hand, the motion of a particle in the Vicsek

model introduces a different mechanism for the spreading of information throughout the system. As an error on a particle's orientation causes particles to move further apart, both diffusion and particle motion can account for the dispersion of fluctuations. It can be shown that for systems with a dimension less than 4, the effect of particle motion dominates over the diffusive process [Gin16]. The spreading of the error on a particle's orientation due to motion results in the disappearance of fluctuations on a large spatial scale for $d > 1$, and long-range order can be established.

2.2 Limiting Cases

Several interesting limiting cases exist for the Vicsek model [Gin16]. In the limit of $v_0 \to 0$, the XY model of ferromagnetism is recovered, as the positions of the particles – and hence their neighbours – are fixed. In the limit of $v_0 \to \infty$, the neighbours of a particle change at every time step so that, from a network perspective, the connectivity matrix is randomly rewired. When $R_0 \to \infty$, the connectivity matrix is static, as all particles interact with one another. Hence, in these limits motion is decoupled from alignment. These limiting cases were shown to be singular [Cha+07] and no conclusions for the general behaviour of the Vicsek model can be drawn from their properties. As will be explained in section 2.4, a strong feedback mechanism exists between local density and order, induced by the motion of the particles. A static or randomly rewired connectivity matrix cannot account for the effect caused by the motion of the particles.

2.3 Angular versus Vectorial Noise

Changing the implementation of adding noise to the motion of the particles was vital in determining the nature of the phase transition. This modification was first introduced by Grégoire and Chaté [GC04]. Instead of adding to the noise the new direction of the agents (dubbed "angular noise"), they opted for "vectorial noise". Here, the stochastic part is added to the calculation of the local average direction of motion, which the authors deemed more realistic. This is in contrast to the original Vicsek model, where every unit could perfectly calculate the average direction of its neighbours, but made

an error on choosing its own new direction. The updating rule for every particle's orientation is then given by

$$\theta_i(t+\Delta t) = \arg\left[\sum_{j\in\Omega_{R_0}(\boldsymbol{x}_i)} e^{i\theta_j(t)} + \eta N_{R_0}(i) e^{i\xi_i(t)}\right], \tag{2.3}$$

where the summation runs over every particle within radius R_0 of the central particle i, $N_{R_0}(i)$ is the current number of these neighbours, ξ is delta-correlated white noise between $-\pi$ and π and η is again the noise strength [GC04]. It is important to mention that this new implementation of the noise is not merely a different convention. With this updating rule, locally ordered regions will be subjected to relatively weaker noise than disordered regions in comparison with the angular noise Vicsek model.

2.4 The Nature of the Phase Transition

In the Vicsek model, a discontinuous phase transition occurs between a disordered state with no net current and a state with long-range order and collective motion. Many papers have been devoted to the nature of this phase transition. At first, the transition between order and disorder was believed to be continuous. Vicsek et al. derived critical exponents for this phase transition in their original paper on the model [Vic+95]. The continuous nature of the phase transition was later cast in doubt, and this crucial problem took more than a decade of active research to resolve (see e.g. [Ald+07; BA08; BA09a; BA09b; Cha+08a; Gré+03; GC04; Nag+07]).

The first indications of a discontinuous transition were provided by Grégoire and Chaté, who first used the vectorial implementation of the noise [GC04]. Further questions were then raised on whether the discontinuity in the phase transition was an artefact of the new noise implementation or really a feature of the Vicsek model. Nagy et al. and Aldana et al. both refuted the claim of a discontinuous transition in the original Vicsek model [Nag+07; Ald+07]. The former concluded from numerical results that the nature of the phase transition depends on the preferred velocity v_0 of the agents, while the latter used network theory to make a case for the distinction between the two types of noise in the system. In the network version of the Vicsek model, agents were allowed to interact with a fixed set of other agents. They applied the updating rules of the Vicsek model, both for vectorial and angular noise,

coming to the conclusion that the nature of the phase transition is dependent on the way the noise is introduced into the system. As mentioned earlier, this last study is a singular case and conclusions cannot be drawn from it since it ignores the crucial coupling between local density and order [Cha+07].

In fact, through extensive numerical simulations, Chaté et al. showed that a "crossover" system size L^* exists for the Vicsek model, beyond which a minimum can be observed in the Binder cumulant, characteristic for discontinuous phase transitions (for a discussion on the Binder cumulant, see section 3.2)[Cha+08a]. L^* is highly dependent on whether the vectorial or scalar noise is implemented. In the case of Vicsek's angular noise, the speed v_0 is also a deciding factor for the nature of the phase transition. While the discontinuous nature is easily observed in the vectorial noise model, the angular noise model requires very large systems and hence extensive numerical studies for it to be evident. The conclusions drawn from the simulations by Chaté et al. are that, while both implementations of the noise in the system display different finite size behaviour, they yield the same asymptotic results: the phase transition in the Vicsek model is discontinuous.

For systems larger than L^*, phase separation can be observed. This phase separation can be understood by considering the feedback between local order and local density for moving particles. In zones with higher local density, particles will find it easier to align their velocities, while particles in lower density zones in the same system move in a disorderly fashion. This shows that increased density has a positive feedback on the alignment between units. Hydrodynamic models have shown that it is this feedback that leads to phase separation near the onset of collective motion [Ber+09], as a long-wavelength instability appears around this point. The long-wavelength instability also explains why the transition appears to be continuous in smaller systems since the cross-over size L^* must be larger than the instability wavelength for phase separation to appear. Phase separation is clearest when looking at travelling bands (2D) or sheets (3D): high-density zones that are ordered internally and travel collectively across the system, stretched perpendicular to the direction of motion. These are surrounded by zones of lower density, where particles move in a disorderly fashion. On very long time scales, the bands are regularly spaced (micro-phase separation) and have well-defined density profiles [Sol+15].

Recent research by Solon et al. on this phase transition has indicated that it is possible to describe it as a liquid-gas transition [Sol+15]. The phase at high noise and low density can be seen as a disordered gas, while a polar liquid is found at low noise and high density values. Similarly to the liquid-gas transition, an intermediate region is found in the phase diagram where the two phases coexist – here, it takes the form of the ordered bands travelling through a disordered gas. However, as shown in Fig. 2.2, it is not possible to go continuously from the liquid to the gas phase. The critical point of the liquid-gas transition is then found at $\rho_c = \infty$.

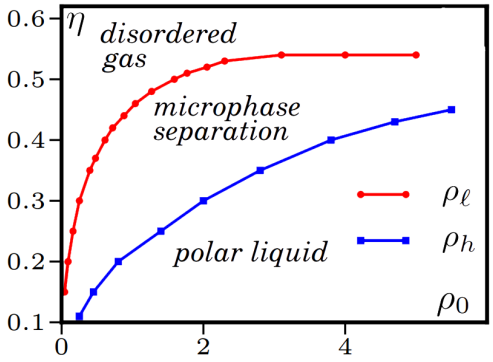

Fig. 2.2.: Phase diagram for the Vicsek model, taken from [Sol+15]. The two binodals ρ_l and ρ_h bound the region where phase coexistence occurs.

To conclude, the diagram of the discontinuous phase transition in the Vicsek model has three distinct regions. At high noise values, the system shows disorder and particles move randomly. At low noise values, the rotational symmetry of the system is broken and the system displays order with collective motion. In between these phases, a region of micro-phase separation exists, and the system displays ordered bands (2D) or sheets (3D) moving through a disorderly gas. The system is bistable at the transition point and can quickly jump between disorder and a single moving band or sheet. This transition is schematically visualized in Fig. 2.3.

If long-range order is to arise, it is necessary that information gets transferred throughout the whole system. The interactions between the particles allow for information transfer, but the stochastic force impedes the communication between the agents in a local neighbourhood. In the case of dilute systems, a simple relation marks the transition point between disorderly and collective motion: the persistence length for isolated particles, which is the distance they can travel without 'forgetting' their initial motion, varies as v_0/η, while the interparticle distance scales as $1/\rho^{1/d}$ [Cha+08a]. If an ordered state is to

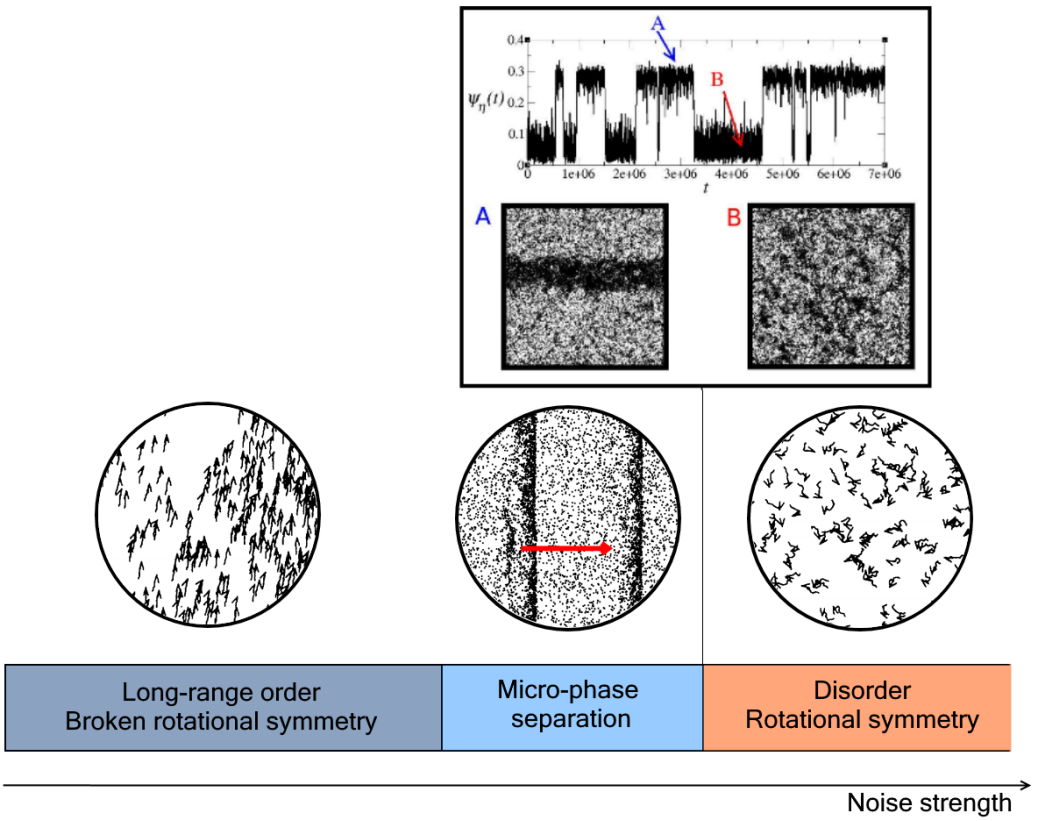

Fig. 2.3.: Schematic summary of the phases in the Vicsek model. The figures of the ordered and disordered phases are taken from [Vic+95], the micro-phase separation from [Cha+08b] and the plot showing the bistability from [Ald+09].

occur, the persistence length must be greater than the average interparticle distance. Hence, the transition noise amplitude is expected to scale as

$$\eta_c \sim v_0 \rho^{1/d}, \tag{2.4}$$

which has been verified in both the 2D and 3D case.

2.5 Role of the Boundary Conditions

The patterns of collective motion appearing in the Vicsek model are highly dependent on the choice of boundary conditions. In the original Vicsek model, periodic boundary conditions (PBC) are applied to mitigate edge effects. This means that, for a 2D system, the particles move on a torus. For open boundary conditions, the system displays no collective motion on large

time scales. Indeed, fluctuations tend to diffuse the particles over a larger and larger distance scale [GC04; Gré+03]. To study collective motion with open boundary conditions, the addition of a short-range force that causes attraction between the particles is required. This will be briefly discussed in section 2.7.

Boundary conditions play an important role in the behaviour of the bands that form for values of the coupling factor right above the transition point. While bands are formed easier in systems with PBC – and preferably travel parallel or diagonally to one of the boundaries – frustrating boundaries such as reflective boundaries will disintegrate these bands. However, they still appear in the bulk of the system [Gin16]. Conversely, reflective boundaries facilitate the formation of vortices which are for instance observed in some bacterial colonies [Czi+96].

2.6 Langevin Description

The stochastic updating rules used in the previous sections already demonstrated how collective motion can be established with active particles. It is often useful from a physics point of view to work with continuous-time equations of motion for the particles under study. Such a framework allows for the introduction of physical quantities such as temperature and entropy into the Vicsek model. Furthermore, allowing some fluctuations around the speed v_0 eases the constraint that all the agents should move at the same speed. To model these last two features, an underdamped equivalent of the original Vicsek model's updating rules was set up, following Langevin dynamics. Langevin dynamics describe the motion of a Brownian particle using stochastic differential equations. The equation of motion for particle i is given by [Gro+12]

$$\begin{cases} \dfrac{\mathrm{d}\boldsymbol{x}_i}{\mathrm{d}t} = \boldsymbol{v}_i, & \text{(2.5a)} \\ m\dfrac{\mathrm{d}\boldsymbol{v}_i}{\mathrm{d}t} = \boldsymbol{F}_i - \gamma(|\boldsymbol{v}_i|)\boldsymbol{v}_i + \sqrt{2D}\boldsymbol{\xi}_i. & \text{(2.5b)} \end{cases}$$

The first term in Eq. (2.5b) describes the velocity-aligning force acting on particle i. A frequently used form of this force is

$$\boldsymbol{F}_i = \Gamma(\boldsymbol{f}_{i,R_0} - \boldsymbol{v}_i), \tag{2.6}$$

where $\boldsymbol{f}_{i,R_0}$ is the average velocity of all particles within distance R_0 of particle i. The parameter Γ indicates the strength of the alignment force and describes how fast the particles can align their direction of motion to the direction of their neighbourhood.

The second term in Eq. (2.5b) is a frictional force. As the particles described here are active, the frictional coefficient γ depends on $|\boldsymbol{v}_i|$ and can adopt positive and negative values. If the speed of a particle is lower than preferred, $\gamma(|\boldsymbol{v}_i|)$ becomes negative and accelerates the particle until its speed reaches v_0. Likewise, for speeds higher than v_0, $\gamma(|\boldsymbol{v}_i|)$ is positive and reduces the speed of the particle. Several forms of the frictional force are possible [Rom+12]. The Rayleigh-Helmholtz friction is defined as

$$-\gamma(|\boldsymbol{v}_i|)\boldsymbol{v}_i = (\alpha - \beta\boldsymbol{v}_i^2)\boldsymbol{v}_i, \tag{2.7}$$

where α and β are positive constants so that $v_0 = \sqrt{\alpha/\beta}$. The term proportional to α causes the acceleration of low-speed particles, and the term proportional to β is the damping for faster-moving particles. This is a nonlinear frictional force. A linear frictional force that describes active particles is also possible, such as the Schienbein–Gruler friction:

$$-\gamma(|\boldsymbol{v}_i|)\boldsymbol{v}_i = -\alpha\left(1 - \frac{v_0}{|\boldsymbol{v}_i|}\right)\boldsymbol{v}_i. \tag{2.8}$$

Finally, the last term in Eq. (2.5b) is the stochastic force in this equation of motion. It is a Gaussian white noise, with its magnitude depending on the diffusion coefficient D, and with uncorrelated components $\xi_k(t)$ such that $\langle\xi_k(t)\rangle = 0$ and $\langle\xi_k(t)\xi_l(t')\rangle = \delta_{kl}\delta(t-t')$.

2.7 Extensions

The Vicsek model served as inspiration for many studies that combine modelling and experimental results. While the original Vicsek model already

displays the patterns found in many natural systems, its minimal nature is limiting when it is compared to experimental data. As mentioned earlier, it fails to describe collective motion in systems with open boundary conditions. Early attempts to include cohesion between the agents were made using long-range – or even global – attractive forces, which pull the units to the group's center-of-mass [Shi+96]. However, it turned out that this – perhaps unrealistic – long-range interaction is not required to keep the flock together: adding a Lennard-Jones-type short-range force proved sufficient to explain how cohesive flocks can form in nature [GC04; Gré+03]. To this aim, the updating rule of Eq. (2.3) was modified to

$$\theta_i(t+\Delta t) = \arg\left[\alpha \sum_{j\in\Omega_R(\boldsymbol{x}_i)} e^{i\theta_j(t)} + \beta \sum_{j\in\Omega_R(\boldsymbol{x}_i)} f_{ij} e^{i\theta_{ij}(t)} + \eta N_R(i) e^{i\xi_i(t)}\right], \quad (2.9)$$

where α and β denote the strength of the alignment and the Lennard-Jones-type force, and θ_{ij} is the direction of the vector that links particle i and j. The force f_{ij} acting on particles separated by a distance r_{ij} is given by

$$f_{ij} = \begin{cases} -\infty & r_{ij} < r_c, \\ \dfrac{1}{4}\dfrac{r_{ij} - r_e}{r_a - r_e} & r_c < r_{ij} < r_a, \\ 1 & r_a < r_{ij} < r_0, \end{cases} \quad (2.10)$$

where the modelling choices $r_c = 0.2$, $r_e = 0.5$, $r_a = 0.8$ and $r_0 = 1.0$ were made. This force has a hard core for distances less than r_c: after taking the argument as in Eq. (2.9), the $-\infty$ term in the force (2.10) ensures that particles separated by a distance less than r_c will move in the opposite direction in the next time step. The particles in this model have a physical size, unlike the point-particles in Vicsek's original model. The force is repulsive for distances less than an equilibrium distance r_e. At the equilibrium distance, no cohesive force is exerted on the particles. For separations greater than the equilibrium distance, the force is attractive up to the cut-off interaction range r_0. For a fixed noise strength, the collective behaviour observed in the system is dependent on the parameters α and β. For small values of β, cohesion cannot be maintained and, in an open system, the flock eventually disintegrates for any value of α. For large enough values of β, a flock can take on either a gas, liquid or solid form. In this case, the value of α decides whether this cohesive group is static or in motion. Note that this transition

point depends on the phase of the flock. The phase diagram drawn from this is shown in Fig. 2.4 [Gré+03].

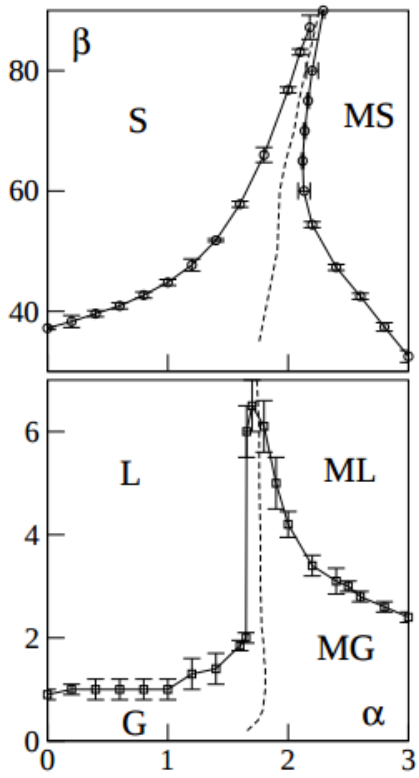

Fig. 2.4.: Phase diagram for collective motion with cohesion, taken from [Gré+03], in function of the parameters α and β. G, L and S denote the gas, liquid and solid phase. The dashed line shows the transition to collective motion (M).

Recently, experimental studies on flocks of starlings have shown that the interaction between these birds may not be dependent on their metric distance, as in the original Vicsek model [Bal+08]. Instead, the nature of the interactions could be topological: every starling only considers its six or seven nearest neighbours. A version of the Vicsek model with such interactions was studied by Ginelli and Chaté [GC10]. In this topological model, the system is divided into cells using Voronoi tessellation and particles interact with those in neighbouring cells. The topological Vicsek model shows markedly different behaviour when compared to the metric version. As the strong feedback between local density and order is no longer present, phase coexistence does not occur at the transition point and the phase transition becomes continuous.

The two modifications discussed above can be seen as vital for modelling natural systems. Many more extensions to the Vicsek model have been made resulting in more realistic behaviour and a better fit to experimental observations. Examples include, but are far from limited to, adding informed individuals to the group [Cou+05], studying the effect of turbulence in the ambient fluid [Cha+08b] and the role of dissenters in breaking up ordered swarms [YM17].

3 Collective Motion without Self-Propulsion

3.1 The Vicsek Model for Passive Particles

Although self-propulsion was long deemed a vital component of collective motion, the question was raised whether a system of passive particles can also show this emergent feature. Furthermore, observations have shown that the overdamped approximation for the trajectories of the agents in these systems is not always justified and inertia can play a role in the establishment of collective motion [Nag+15]. Sevilla et al. developed a model with passive Brownian particles following Langevin dynamics [Sev+14]. Similarly to the discussion in section 2.6, the stochastic differential equation describing such a system is given by

$$\begin{cases} \dfrac{\mathrm{d}\boldsymbol{x}_i}{\mathrm{d}t} = \boldsymbol{v}_i, & \text{(3.1a)} \\ m\dfrac{\mathrm{d}\boldsymbol{v}_i}{\mathrm{d}t} = \boldsymbol{F}_i - \gamma(v)\boldsymbol{v}_i + \boldsymbol{\xi}_i. & \text{(3.1b)} \end{cases}$$

The second term on the right-hand side of Eq. (3.1b) is the dissipative friction term. In the case of passive Brownian particles, the frictional coefficient is given by $\gamma(v) = \gamma$. The vector $\boldsymbol{\xi}_i$ is the stochastic term of this model. Its components, $\xi_{i,\mu}(t)$, are Gaussian white noises with zero mean and an autocorrelation function of

$$\langle \xi_{i,\mu}(t)\xi_{j,\nu}(t+\tau)\rangle = 2\gamma k_B T \delta_{i,j}\delta_{\mu,\nu}\delta(\tau), \tag{3.2}$$

where k_B is the Boltzmann constant and T is the temperature of the heat bath. The diffusion coefficient D is here given by $\gamma k_B T$, according to the fluctuation-dissipation theorem.

In the model by Sevilla et al., the short-range social force is given by

$$\boldsymbol{F}_i = \Gamma \hat{\boldsymbol{v}}_i \times (\boldsymbol{f}_i \times \hat{\boldsymbol{v}}_i) \tag{3.3}$$

$$= \Gamma[\boldsymbol{f}_i - \hat{\boldsymbol{v}}_i(\hat{\boldsymbol{v}}_i \cdot \boldsymbol{f}_i)]. \tag{3.4}$$

Γ is a coupling factor that controls the rate at which particles align their direction to the direction of their neighbours. $\hat{\boldsymbol{v}}_i$ is the unit vector of $\boldsymbol{v}_i$ and $\boldsymbol{f}_i$ corresponds to the average direction of motion of particles within the neighbourhood $\Omega_R(\boldsymbol{x}_i)$ of a radius R of particle i:

$$\boldsymbol{f}_i = \frac{1}{N_R(i)} \sum_{j \in \Omega_R(\boldsymbol{x}_i)} \hat{\boldsymbol{v}}_j. \tag{3.5}$$

The denominator $N_R(i)$ equals the number of neighbours of particle i. This force was chosen as it turns every particle's direction of motion towards the average direction of their neighbours, but does not impose any self-propelling effect. The non-propelling nature of this force can be verified, as $\boldsymbol{F}_i \cdot \boldsymbol{v}_i = 0$. Hence, the force on each particle is perpendicular to its velocity and does no work. By denoting the angle between $\hat{\boldsymbol{v}}_i$ and $\boldsymbol{f}_i$ as θ, the magnitude of the force $\boldsymbol{F}_i$ can be written as

$$\begin{aligned} |\boldsymbol{F}_i| &= \Gamma \sqrt{|\boldsymbol{f_i}|^2(1 - \cos^2(\theta))} \\ &= \Gamma |\boldsymbol{f_i}| |\sin(\theta)|. \end{aligned} \tag{3.6}$$

This implies that when the velocity of a particle and the mean velocity of its neighbours are anti-aligned, no force is exerted on the agent. However, this is not a stable state as the thermal fluctuations lead to the eventual alignment of the velocities if the coupling factor is high enough.

By rewriting the equation of motion Eq. (3.1b) in polar coordinates [DS15], it becomes clear that one can speak of thermal propulsion instead of self-propulsion:

$$m \frac{\mathrm{d}v_i}{\mathrm{d}t} = -\gamma v_i + \frac{k_B T \gamma}{m} \frac{1}{v_i} + \xi_{v_i}, \tag{3.7}$$

$$m v_i \frac{\mathrm{d}\phi_i}{\mathrm{d}t} = \frac{\Gamma}{N_R(i)} \sum_{j \in \Omega_R(\boldsymbol{x}_i)} \sin(\phi_j - \phi_i) + \xi_{\phi_i}. \tag{3.8}$$

The Gaussian white noises ξ_{v_i} and ξ_{ϕ_i} are obtained from a rotation of the Cartesian components of $\boldsymbol{\xi_i}$. The second term in Eq. (3.7) is obtained from Ito calculus and indicates the thermal propulsion.

The number of independent parameters in this model can be reduced by introducing dimensionless variables:

$$\tilde{t} = \frac{t}{t_0},\ \tilde{\boldsymbol{v}} = \frac{\boldsymbol{v}}{v_0} \text{ and } \tilde{\boldsymbol{r}} = \frac{\boldsymbol{r}}{r_0} = \frac{\boldsymbol{r}}{v_0 t_0}, \tag{3.9}$$

where

$$t_0 = \frac{m}{\gamma} \text{ and } v_0 = \sqrt{\frac{2k_B T}{m}}. \tag{3.10}$$

The original equation of motion (3.1b) can now, after dividing by γv_0, be reduced to

$$\frac{d\tilde{\boldsymbol{v}}_i}{d\tilde{t}} = \tilde{\Gamma}[\boldsymbol{f}_i - \hat{\boldsymbol{v}}_i(\hat{\boldsymbol{v}}_i \cdot \boldsymbol{f}_i)] - \tilde{\boldsymbol{v}}_i + \sqrt{\delta(\tilde{\tau})}N(0,1), \tag{3.11}$$

where $\tilde{\Gamma} = \dfrac{\Gamma}{\gamma v_0}$ and $N(0,1)$ is a number drawn from a Gaussian distribution with zero mean and unit variance. This dimensionless version of the coupling factor describes the ratio between two different time scales: one for the alignment rate between the particles and the other corresponding to the stochastic motion of the Brownian particles. As such, it is a logical choice for the control parameter when modelling this system at a fixed density.

By switching to dimensionless variables, only three independent parameters remain: the dimensionless coupling constant $\tilde{\Gamma}$, the dimensionless density $\tilde{\rho} = \frac{N}{L^d}$ and the dimensionless interaction range R_0. Here, the dimensionless version of the system size $\mathscr{L}$ is given by $L = \frac{\mathscr{L}}{r_0}$ and d is the dimension. The dimensionless interaction range is $R_0 = \frac{R}{r_0}$. From here on out, $R_0 = 1$ is fixed without any loss of generality, as the spatial dimensions can always be rescaled to obtain this value for the interaction range.

The system is initialized with positions uniformly distributed over the coordinate space and velocities drawn from a Maxwell-Boltzmann distribution: each component of the velocity vector is drawn from a Gaussian distribution with zero mean and variance $\frac{kT}{m}$. This is the equilibrium distribution in the case of $\Gamma = 0$.

3.2 Observables

Order parameter

To monitor the different phases in the system, the accumulated order parameter $\langle\Lambda\rangle$ is assessed. This is the time-averaged value of the instantaneous order parameter $\Lambda(t) = \frac{1}{N}|\sum_{i=1}^{N} \hat{\boldsymbol{v}}_i(t)|$. For an infinite system, Λ equals zero as the particles move disorderly and the directions of the velocity cancel each other out. $\langle\Lambda\rangle$ adopts a positive value when collective motion has been established. For the systems simulated here, the directions do not exactly cancel each other out and $\langle\Lambda\rangle \propto \sqrt{\frac{1}{N}}$ in the disordered phase.

The way in which $\langle\Lambda\rangle$ changes from zero to a positive value depends on the nature of the phase transition. For a continuous phase transition, the change is smooth. For a discontinuous phase transition, $\langle\Lambda\rangle$ shows a discontinuity at the transition value, which is marked by the coexistence of both phases. As in the active Vicsek model, size effects play an important role in these simulations, making it difficult to determine the nature of the phase transition. The following three observables help in making the distinction between the two types of transitions.

Distribution of the order parameter

One method to determine the nature of the phase transition is to look at the distribution of Λ when the coupling factor's value is around the transition point $\tilde{\Gamma}_c$. For a first-order phase transition, the coexistence of two phases implies that the distribution of the order parameter becomes bimodal at this point. For a second-order phase transition, a single peak is observed at the transition point.

Binder cumulant

The Binder cumulant G plays an important role in deciding whether the phase transition is continuous or discontinuous [Bin81]. It is defined as

$$G = 1 - \frac{\langle\Lambda^4\rangle}{3\langle\Lambda^2\rangle^2}, \tag{3.12}$$

where $\langle\Lambda^2\rangle$ and $\langle\Lambda^4\rangle$ are the second and fourth moments of the distribution of the instantaneous order parameter Λ. As for a Gaussian distribution $\langle\Lambda^4\rangle = 3\langle\Lambda^2\rangle^2$ so that $G = 0$, the Binder cumulant is a measure of how much the distribution of the order parameter deviates from a Gaussian distribution.

For the disordered phase, the velocity components are random vectors with components drawn from a zero-mean Gaussian with standard deviation $\sigma = \sqrt{k_b T/m}$. The norm of d standard normally distributed variables is a χ-distribution with d degrees of freedom, so that its probability density function is

$$P(x,d) = \frac{2^{1-\frac{d}{2}} x^{d-1} e^{-\frac{d^2}{2}}}{\Gamma\left(\frac{d}{2}\right)}, \tag{3.13}$$

for which $\langle x^4\rangle = d(d+2)$ and $\langle x^2\rangle = d$. After rescaling the velocity components by σ so that the standard deviation on the components also becomes unity, it follows that $\sigma\Lambda$ is distributed according to Eq. (3.13). This implies that the Binder cumulant is $\frac{1}{3}$ in the disordered phase of a 2D system. It is expected that $\langle\Lambda^4\rangle = \langle\Lambda^2\rangle^2$ for high values of the coupling factor, because the noise has little effect in this regime. Consequently, $G \approx \frac{2}{3}$ for these values of Γ.

In between these two extremal cases, the value of the Binder cumulant depends on the nature of the phase transition. If the transition is continuous, the Binder cumulant varies smoothly between its values for order and disorder. At the critical point of a continuous transition, G takes on a universal value independent of system size. For a discontinuous phase transition, the appearance of two peaks in the distribution of the order parameter at the transition point causes $\langle\Lambda^4\rangle$ to take on a higher value than $3\langle\Lambda^2\rangle^2$ so that the Binder cumulant shows a distinct minimum at the transition between the two phases [Ach99].

Susceptibility

For the Vicsek model, the susceptibility of the order parameter is defined as

$$\chi = L^d\left(\left\langle\Lambda^2\right\rangle - \langle\Lambda\rangle^2\right) = L^d\,\mathrm{Var}(\Lambda). \tag{3.14}$$

While its interpretation is different from the susceptibility in equilibrium systems, it has been shown that for non-equilibrium systems the phase transition also occurs at its peak value and its shape is also determined by the nature of this transition [Sid+98].

3.3 Results

To verify the results obtained by Dossetti and Sevilla [DS15], the accumulated order parameter $\langle\Lambda\rangle$ is plotted against the dimensionless coupling factor $\tilde{\Gamma}$ in Fig. 3.1 for a density $\tilde{\rho} = 2$ and in Fig. 3.2 for $\tilde{\rho} = 4$. These results were obtained by averaging over 3-7 initial configurations and $4\text{-}10 \cdot 10^6$ time steps after reaching the steady state, depending on how close the coupling factor is to the transition value. Details on the numerical integration of the equation of motion can be found in section A.1. It is clear that the development of collective motion requires a larger coupling factor as the density decreases. This can be expected, since higher density implies more interactions (i.e. passing of information), which facilitates the establishment of long-range order. The scaling of $\langle\Lambda\rangle$ with the system size L is also shown. For lower values of L, finite size effects are apparent. This results in the 'rounding' of the curve for small systems. Similarly to the original Vicsek model, the discontinuous nature only becomes visible for larger system sizes.

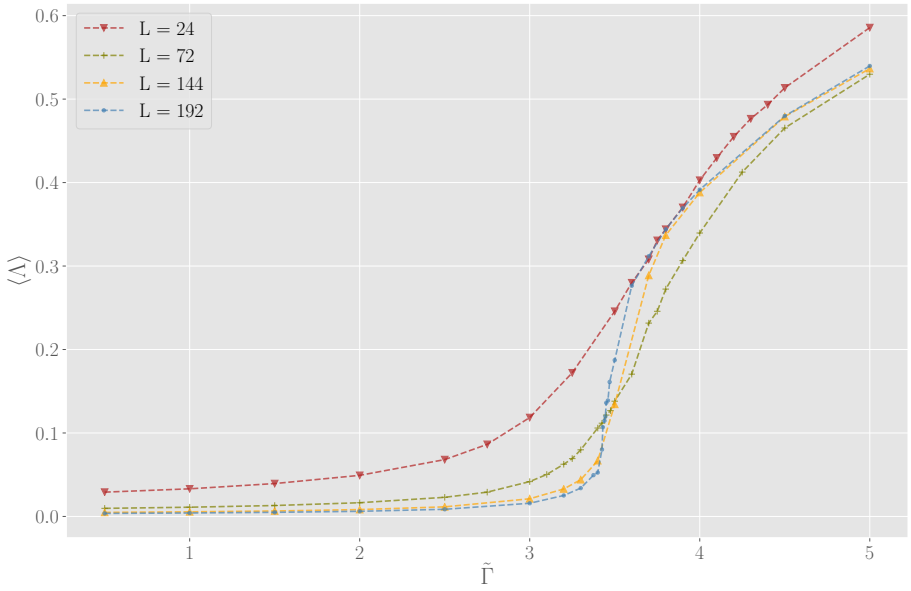

Fig. 3.1.: Time-averaged order parameter $\langle\Lambda\rangle$ in function of the dimensionless coupling factor $\tilde{\Gamma}$ for $\tilde{\rho} = 2$.

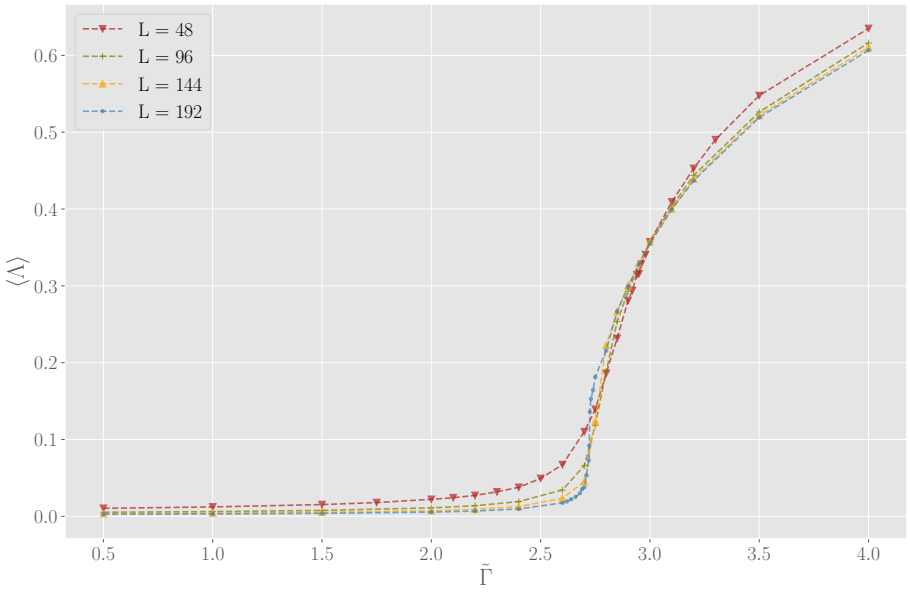

Fig. 3.2.: Time-averaged order parameter $\langle\Lambda\rangle$ in function of the dimensionless coupling factor $\tilde{\Gamma}$ for $\tilde{\rho} = 4$.

The discontinuous nature of the phase transition is at its clearest when looking at the Binder cumulant (Fig. 3.3 and 3.4) and the distribution of the order parameter (Fig. 3.5). While the Binder cumulant remains continuous for the smaller system sizes, a distinct minimum ($G \ll 1/3$) appears for the largest system size ($L = 192$) under study. This implies that, similarly to the case of active particles, the discontinuity of the phase transition only becomes apparent for very large system sizes. The distribution of the order parameter is bimodal around the transition point for the largest system sizes, as the system is bistable and alternates between disorder and a single moving band. This can be identified in the time evolution of the order parameter.

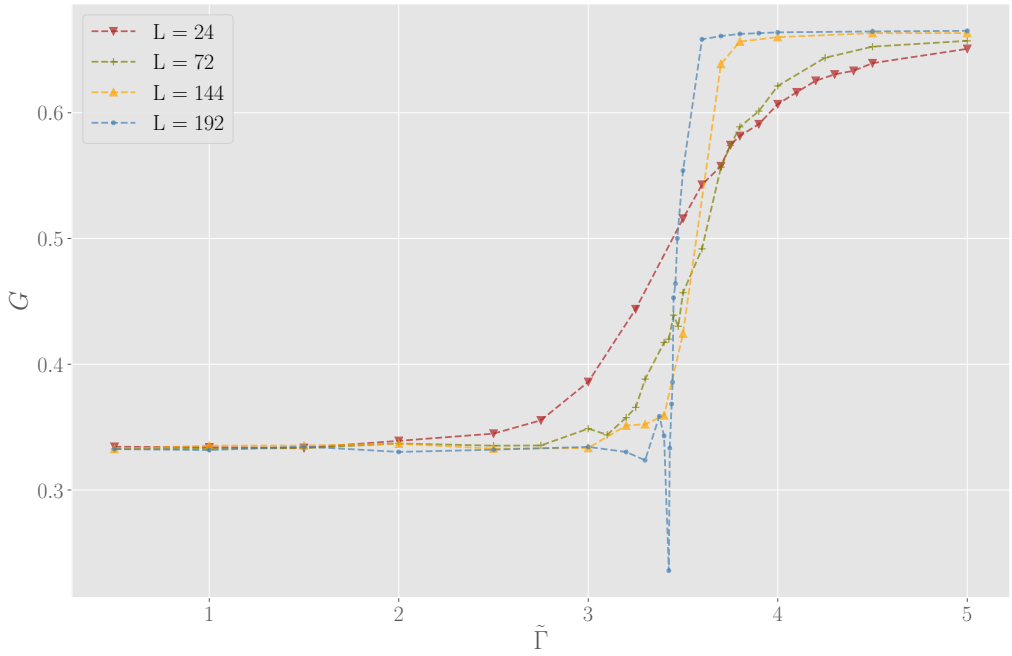

Fig. 3.3.: The Binder cumulant G in function of the dimensionless coupling factor $\tilde{\Gamma}$ for $\tilde{\rho} = 2$.

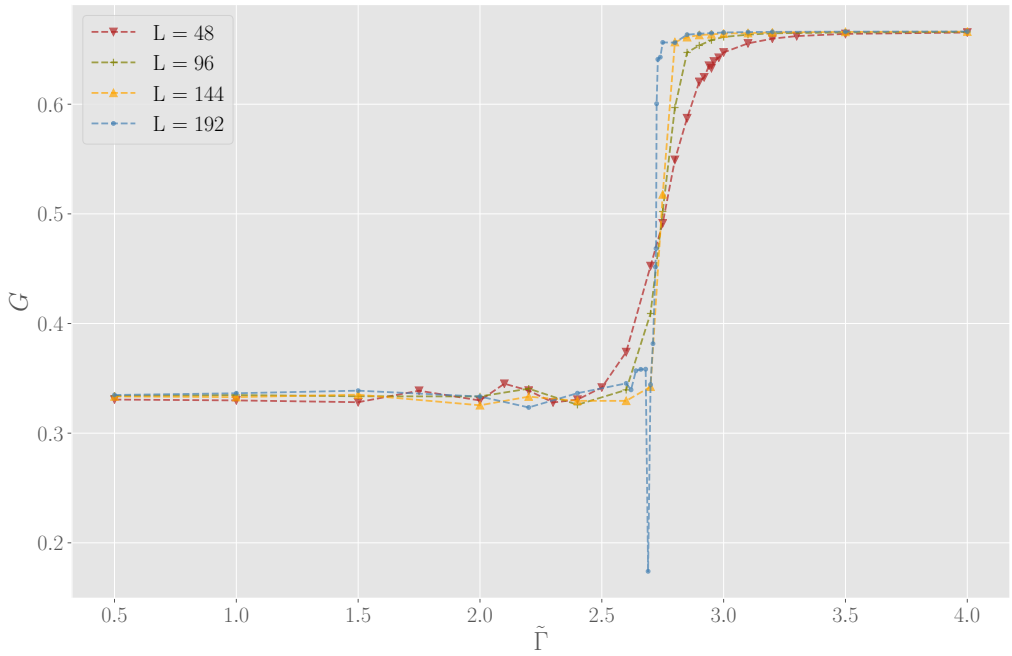

Fig. 3.4.: The Binder cumulant G in function of the dimensionless coupling factor $\tilde{\Gamma}$ for $\tilde{\rho} = 4$.

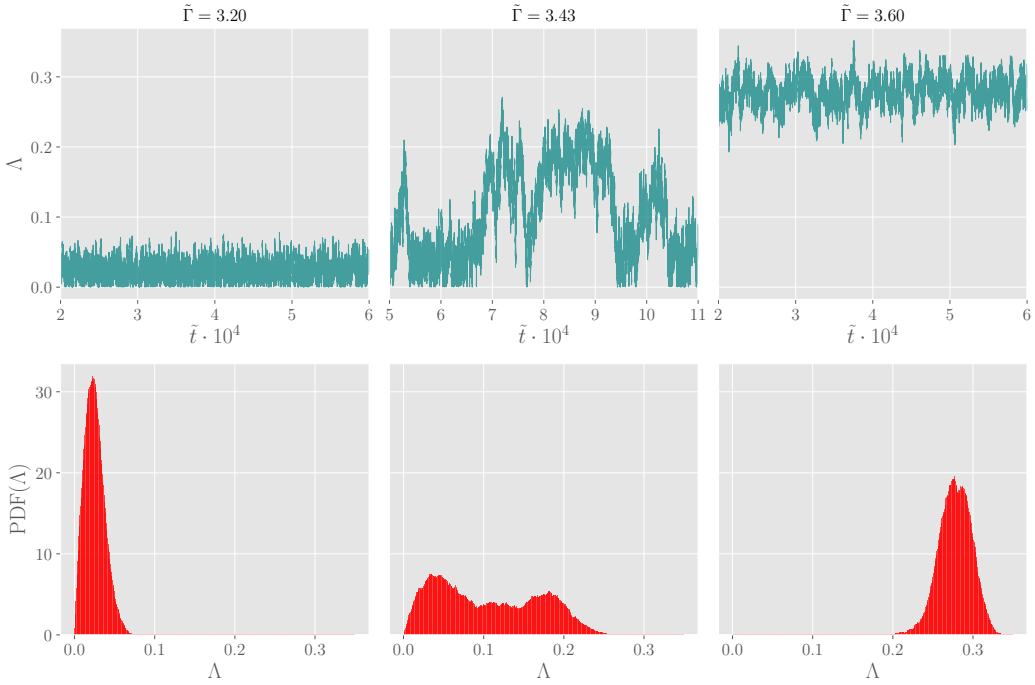

Fig. 3.5.: Time evolution (first row) and probability density function (second row) of the order parameter for a system with $L = 192$ and $\tilde{\rho} = 2$.

3.3.1 Long-range order

To illustrate the existence of long-range order (LRO) above the transition value $\tilde{\Gamma}_c$, Fig. 3.6 shows $\langle\Lambda\rangle$ for $\tilde{\Gamma} = 8 > \tilde{\Gamma}_c$, with density $\tilde{\rho} = 4$ and system sizes $L = 24, 48, 72, 96, 120, 144$. For a coupling constant below the transition point, $\langle\Lambda\rangle$ quickly decays to zero. However, it can be seen that for a coupling constant for which collective motion is present, $\langle\Lambda\rangle$ decays to a positive value, although the decay is algebraic (i.e. like a power-law) rather than exponential. This shows that this model achieves true LRO. This is in contrast with the observations in the 2D XY model, where the MWT holds and only quasi long-range order is achieved, as the order parameter decays algebraically to zero [Gin16].

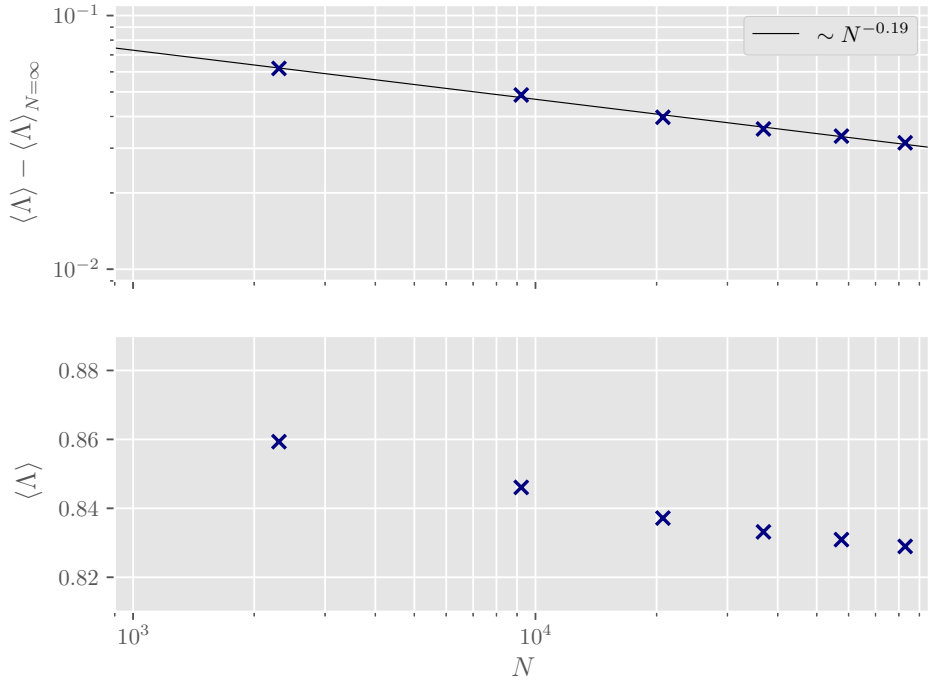

Fig. 3.6.: Decay of $\langle\Lambda\rangle$ with number of particles. For the upper graph, a value $\langle\Lambda\rangle_{N=\infty} = 0.797$ has been subtracted from $\langle\Lambda\rangle$. The fitted line shows the slow decay of $\langle\Lambda\rangle$ to $\langle\Lambda\rangle_{N=\infty}$.

3.3.2 Giant number fluctuations

A feature of collective motion is the greatly increased fluctuations in local density, often called 'giant density fluctuations' or 'giant number fluctuations' (GNF). When dividing the system in boxes of linear size l, the expected amount of particles present in a box is $\langle n\rangle = \rho l^d$, where d is the dimension of the system. In equilibrium, it follows from the central limit theorem that the standard deviation on the number of particles in such a box scales with the square root of the average: $\Delta n = \sqrt{\langle n^2\rangle - \langle n\rangle^2} \propto \sqrt{\langle n\rangle}$. However, both simulations and analytical considerations have shown that, in the phase where collective motion is present, this relation no longer holds [Cha+08a; TT98]. Instead, the observed fluctuations are much larger and $\Delta n \propto n^\alpha$ with $\alpha > \frac{1}{2}$. For active particles, this exponent $\alpha = \frac{1}{2} + \frac{d+1}{5d}$, so that $\alpha = 0.8$ in a 2D system [Gin16]. Dossetti and Sevilla noted that for collectively moving passive particles, these fluctuations are even greater [DS15]. This result is verified in Fig. 3.7. To calculate the GNF, the system is divided in boxes of size $l = L/2$, $l = L/4$,... The amount of particles in each box is then counted,

and the standard deviation is calculated with respect to ρl^2. This process was repeated for a large amount of time steps ($\approx 10^5$). As can be seen in Fig. 3.7, the same exponent as in the equilibrium situation is measured (within the margin of error) for a system in a disorderly state. When the system develops collective motion in the form of bands, GNF appear with an exponent $\alpha \approx 0.9$. The fluid phase exhibits the same behaviour. Note that system size has a large effect on the observed GNF: fluctuations for increasing box sizes will become smaller, as they contain a significant portion of the whole system.

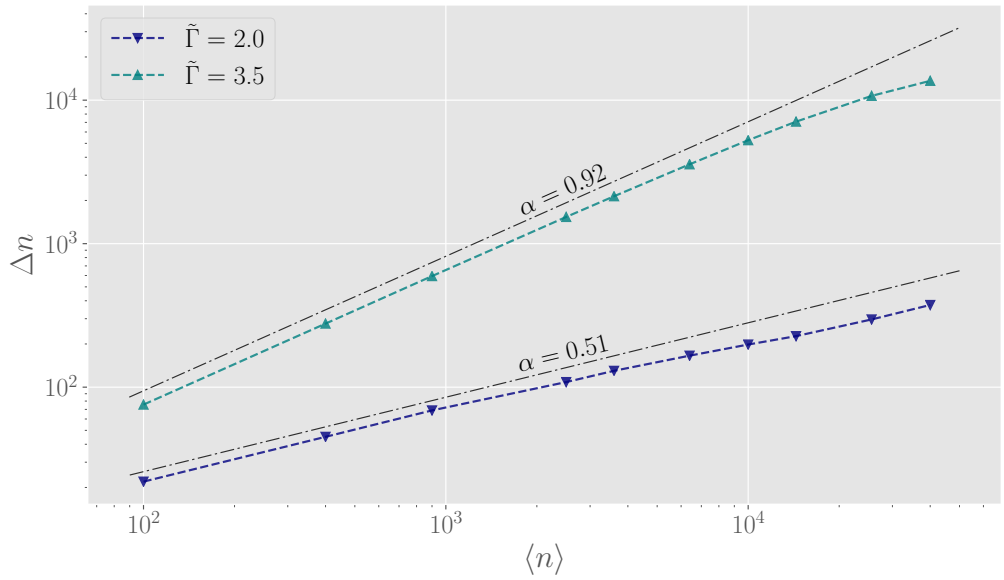

Fig. 3.7.: Expected number of particles in a box versus the fluctuations on this number, measured in a system with $L = 192$ and $\tilde{\rho} = 4$ for two different values of the coupling factor. The dash-dotted lines are fits of $\Delta n \propto \langle n \rangle^{\alpha}$.

3.3.3 Distribution of the velocity components

The distribution of the velocity components is shown in Fig. 3.8 for several values of the coupling factor $\tilde{\Gamma}$. These components are projected on the direction of the center-of-mass velocity for the system ($v_{\parallel}$) and the direction perpendicular to this ($v_{\perp}$). Their distributions $P(v_{\parallel})$ and $P(v_{\perp})$ are given, as well as the combined probability $P(v_{\parallel}, v_{\perp})$. The black curve plotted alongside the distributions of $P(v_{\parallel})$ and $P(v_{\perp})$ is the Maxwell-Boltzmann distribution from which each system initially starts. For the system considered here, the transition to collective motion happens at $\tilde{\Gamma} \approx 2.72$. For values of the coupling factor that are greater than zero but well below the critical value such as in Fig. 3.8a, the Maxwell-Boltzmann distribution is retained, indicating that the

particles do not have time to align their motion before noise again randomizes it. For values of $\tilde{\Gamma}$ just below the transition value (Fig. 3.8b), the peak of $P(v_{\parallel})$ is slightly shifted towards a positive value, which can be explained by size effects. For values of the coupling factor above the transition value, the peak strongly shifts toward a positive value, as in Fig 3.8c. Note that $P(v_{\parallel})$ becomes asymmetrical: negative values of $v_{\parallel}$ are increasingly unbalanced. The distribution of $v_{\perp}$ stays symmetrical with zero mean.

The time evolution of the entropy associated with the velocity distribution[1] of a single particle, S_v, is shown in Fig. 3.9. The system starts from a completely disordered situation and evolves to display collective motion ($\langle\Lambda\rangle \approx 0.7$). The development of order is reflected in S_v: it is maximal when the system is in complete disorder and decreases as order develops.

[1] A general introduction to entropy is given in section 5.1.

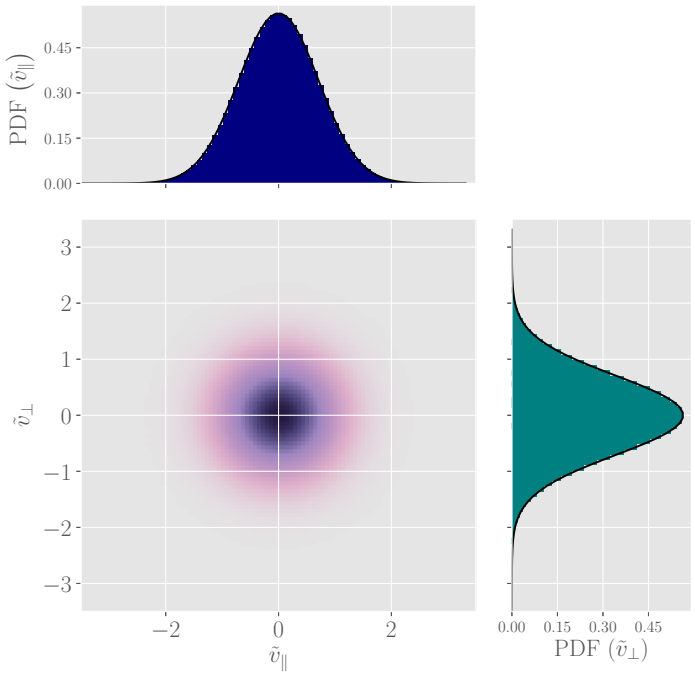

(a) $\tilde{\Gamma} = 1.5$

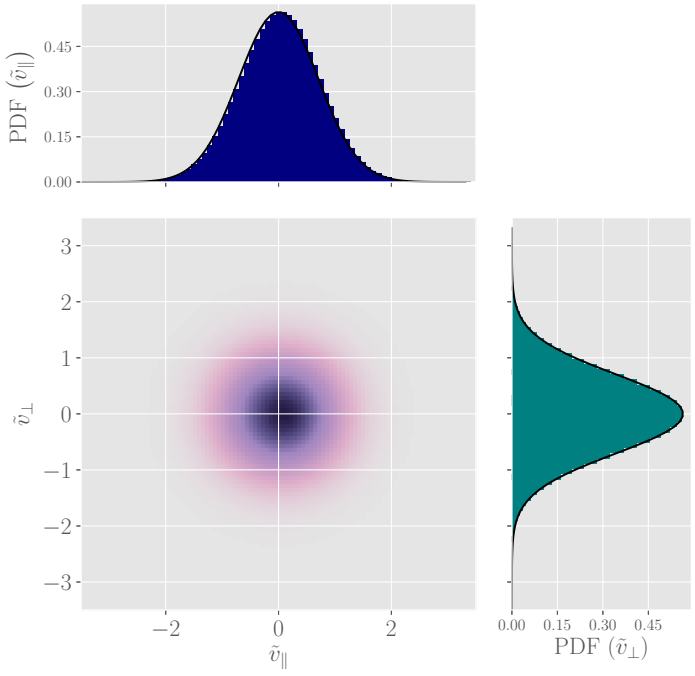

(b) $\tilde{\Gamma} = 2.5$

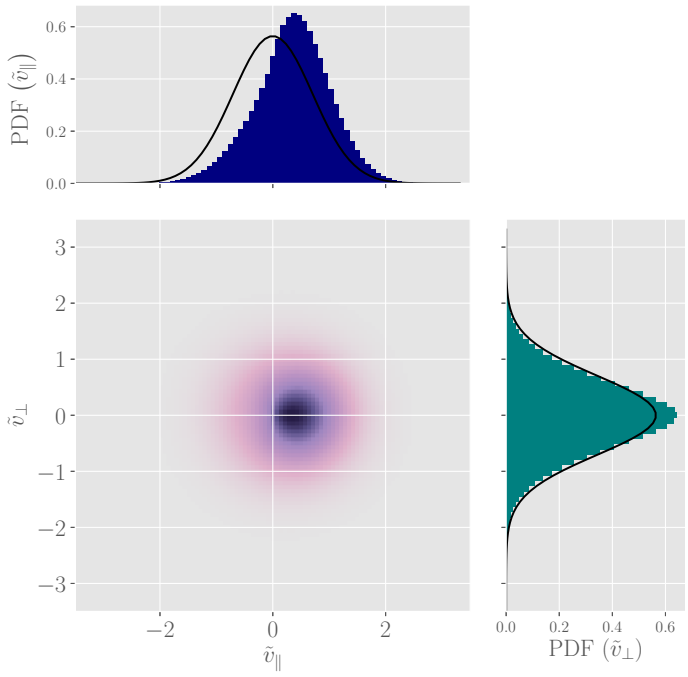

(c) $\tilde{\Gamma} = 3.0$

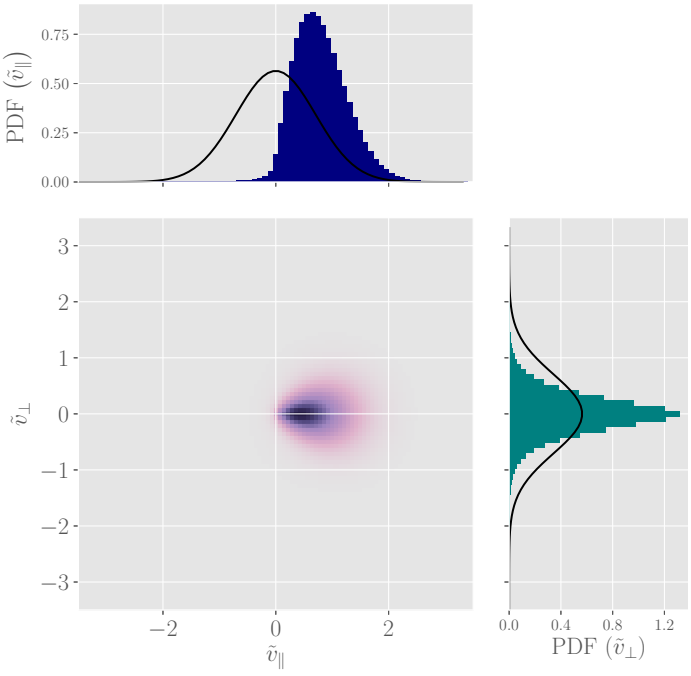

(d) $\tilde{\Gamma} = 10.0$

Fig. 3.8.: Distribution of the velocity components for several values of the coupling factor, for a system with $L = 96$ and $\tilde{\rho} = 4$. The upper and right figure show the distribution of the component parallel and perpendicular to the average direction of motion, respectively. The black line on these figures is the initial distribution. The 2D density plot is the combined probability.

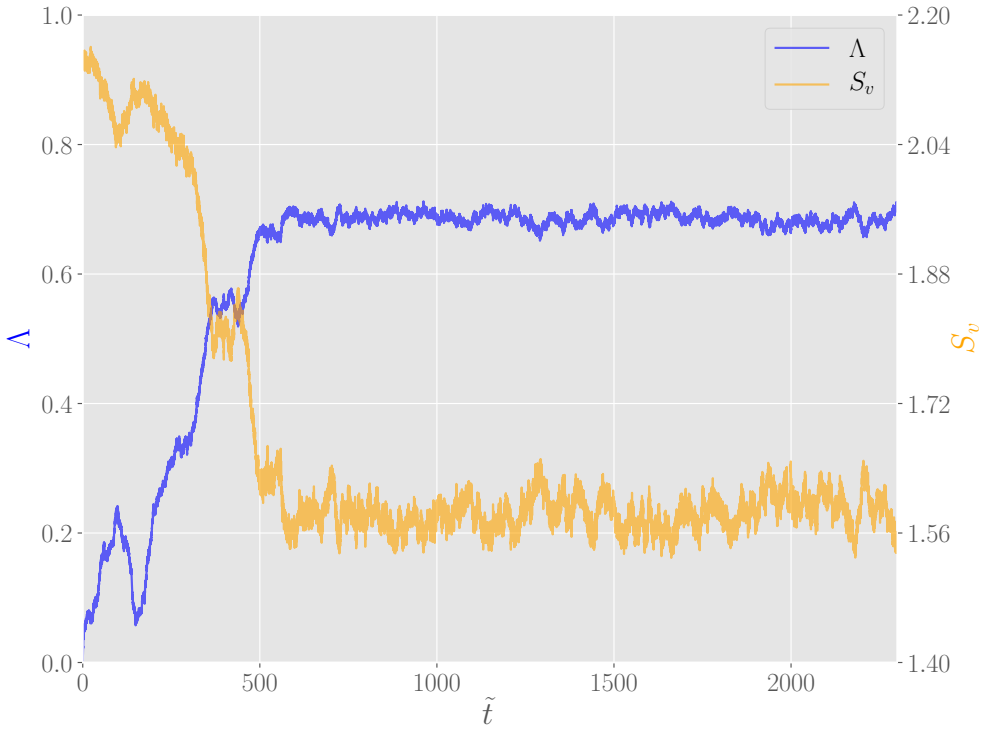

Fig. 3.9.: Time evolution of the entropy associated with the one-particle velocity distribution S_v and the order parameter $\langle\Lambda\rangle$ for a system with $L = 96$, $\tilde{\Gamma} = 4.5$ and $\tilde{\rho} = 4$.

3.3.4 Velocity autocorrelation

The velocity autocorrelation function (VACF) shows the correlation between the velocity of a particle at a reference time t' and some later time t. It is defined as

$$C_{\boldsymbol{vv}}(t) = \frac{1}{N}\sum_{i=1}^{N}\frac{\langle \boldsymbol{v}_i(t')\cdot\boldsymbol{v}_i(t'+t)\rangle_{t'}}{\langle \boldsymbol{v}_i(t')\cdot\boldsymbol{v}_i(t')\rangle_{t'}}, \tag{3.15}$$

where $\langle\cdot\rangle_{t'}$ denotes taking an average over the reference times t'. The amount of particles involved in these simulations makes calculating autocorrelations a computationally expensive procedure, but by using Fast Fourier Transforms this can be done efficiently (briefly explained in A.3)[NB99]. The decay of this function indicates how quickly a particle forgets its initial motion, as the velocity becomes independent of its initial value.

Fig. 3.10 shows the VACF for several values of the coupling factor. Note that for values of $\tilde{\Gamma}$ that are smaller than the transition value, the VACF

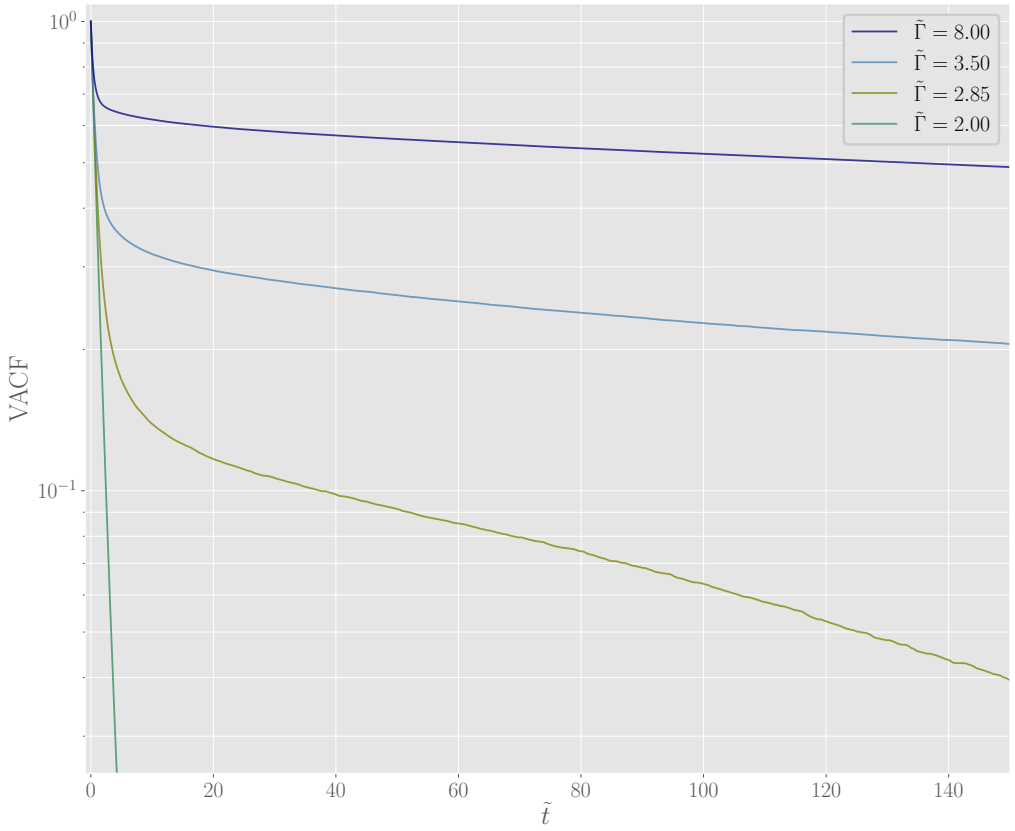

Fig. 3.10.: Velocity autocorrelation function versus time in a system with $L = 192$ and $\tilde{\rho} = 4$.

decays as $e^{-\tilde{t}}$. The same decay is expected for non-interacting Brownian particles: the particles do not have time to align their motion and thus move around randomly. For values of $\tilde{\Gamma}$ above the transition point, motion is more persistent. On a short time scale the VACF still shows a strong decay. This can be explained by considering the particles that do not belong to a band or cluster: these particles still move randomly and their contribution to the VACF is an exponential decay. The contribution of the other particles causes the long tail in the total VACF of the system.

3.3.5 Particle diffusion

Due to the Brownian dynamics, initially neighbouring particles in the system move further apart as simulation time increases. To investigate particle diffusion, the relative mean square displacement of initially neighbouring particles is measured. By looking at the relative displacement, the effect of

the global motion – should it be present – is largely subtracted. The relative mean square displacement is defined as

$$\left\langle \Delta r_{Nb}^2(t) \right\rangle = \frac{1}{N_p} \sum_{i=1}^{N_p} \left(r_{Nb,i}(t) - r_{Nb,i}(0) \right)^2 , \tag{3.16}$$

in which the sum on the right-hand side runs over all N_p initially neighbouring pairs. For Brownian motion ("normal diffusion"), this scales as [BG90]

$$\left\langle \Delta r_{Nb}^2(t) \right\rangle \sim t^\nu \text{ with } \nu = 1, \tag{3.17}$$

whereas in the case of super-diffusion,

$$\left\langle \Delta r_{Nb}^2(t) \right\rangle \sim t^\nu \text{ with } \nu > 1. \tag{3.18}$$

Nagy et al. have shown that the diffusion of self-propelled particles is anisotropic with regard to the mean direction of motion [Nag+07]. To measure this anisotropy, the mean squared displacement was projected parallel to the mean direction of motion, $\left\langle \Delta r_{Nb,\parallel}^2(t) \right\rangle$, as well as perpendicular to this direction, $\left\langle \Delta r_{Nb,\perp}^2(t) \right\rangle$. For active agents, the anisotropy A, measured as

$$A = \frac{\left\langle \Delta r_{Nb,\perp}^2(t) \right\rangle}{\left\langle \Delta r_{Nb,\parallel}^2(t) \right\rangle}, \tag{3.19}$$

was found to be highly dependent on the constant speed v_0 of the self-propelled particles, as $A \approx 1$ in the low-speed regime ($v_0 < 0.1$) and $A > 1$ for greater speeds ($v_0 > 0.3$). Measurements of the diffusion of initially neighbouring passive particles are shown in Fig. 3.11. In the disordered phase, normal diffusion occurs with an exponent $\nu \approx 1$, while for the ordered phase $\nu \approx \frac{4}{3}$ and super-diffusion is observed over long simulation periods. For small simulation times, the scaling is different as the particles are still subjected to each other's strong alignment interaction [Nag+07]. The diffusion in the ordered phase is measured for a very high value of the coupling factor. For lower values of $\tilde{\Gamma}$, the average velocity shows larger fluctuations making a projection on the parallel and perpendicular direction impossible for long simulation times. As can be seen in Fig. 3.11b, the diffusion of initially neighbouring particles is still anisotropic but, contrary to self-propelled particles, diffusion is now faster in the direction parallel to the center-of-mass velocity, so that $A < 1$. A possible explanation for this difference could be that in the case of passive particles, the speed of the agents in the direction parallel to the direction of motion is a broad distribution (Fig. 3.8d). For the active

particles, it could be expected that this velocity distribution is more peaked around the self-propelled speed v_0 for the strong alignment interactions considered here. Passive particles that move in the same direction can have a markedly different parallel velocity component, which gives an additional contribution to the mean square displacement in this direction compared to the active particle model.

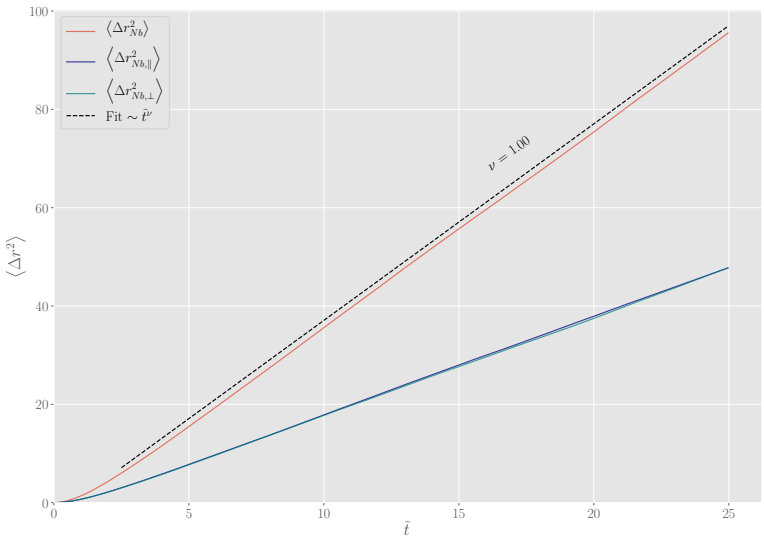

(a)

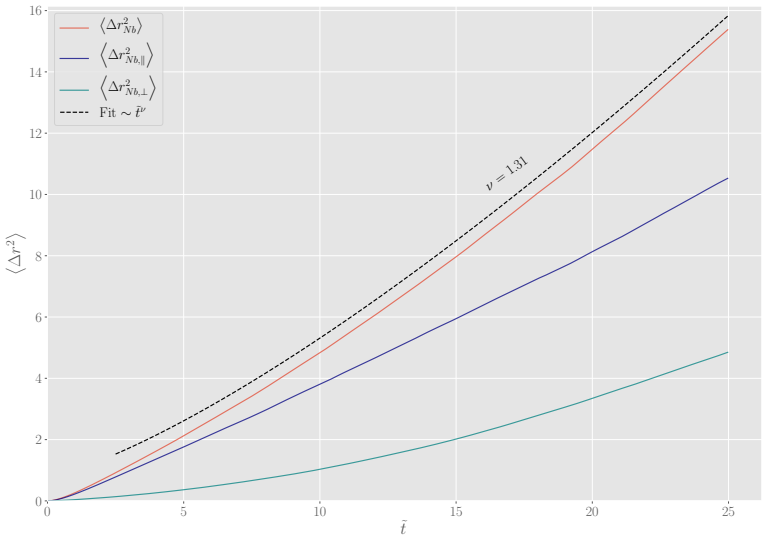

(b)

Fig. 3.11.: (a) Relative mean square displacement of initially neighbouring particles versus time in a system with $L = 96$, $\tilde{\rho} = 4$ and $\tilde{\Gamma} = 1.5$. The dotted line $\sim \tilde{t}^{\nu}$ indicates the best fit for the exponent ν. (b) Same as in (a) but with $\tilde{\Gamma} = 10$.

3.4 Globally-Coupled Version

Finally, the results for a globally-coupled version of this model are discussed here, as a verification of the work of Sevilla et al. [Sev+14]. In the globally-coupled version of this model, the interaction range is no longer a parameter so that the system size can always be rescaled to obtain $\tilde{\rho} = 1$. Only one parameter remains: the dimensionless coupling factor $\tilde{\Gamma}$.

Fig. 3.12 show the results for varying numbers of particles. Note that, in contrast to the short-range model, the Binder cumulant (Fig. 3.12b) shows no minimum, but is instead continuous around the transition point. This indicates a second-order phase transition. The size effects can be seen by the shifting of the peak of the susceptibility (located at the transition point) to lower values of $\tilde{\Gamma}$ for larger systems.

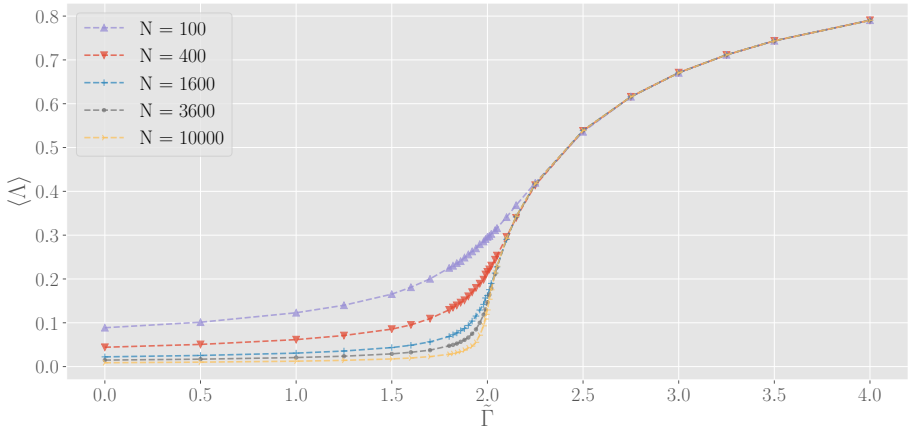

(a)

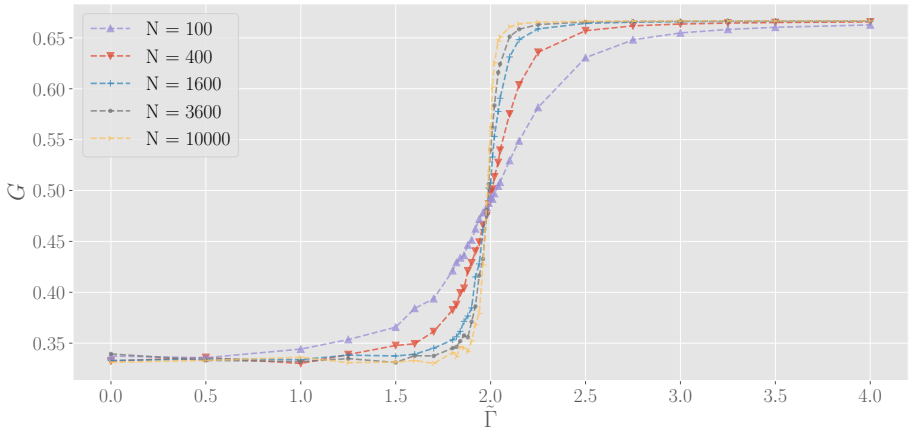

(b)

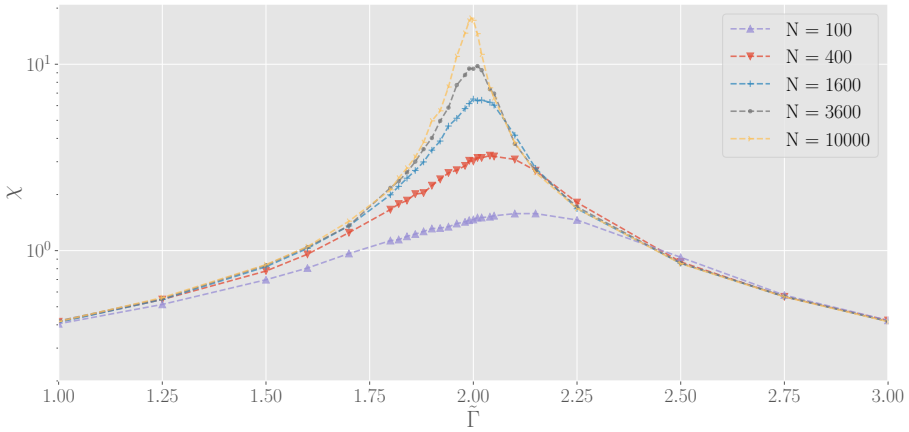

(c)

Fig. 3.12.: (a) Order parameter, (b) Binder cumulant and (c) susceptibility for a globally-coupled system.

4 Spatial Structure and Correlations

4.1 Visualization

Fig. 4.1 shows the possible spatial configurations for the model introduced in chapter 3. For values of the coupling factor well below the transition value, the system is more or less homogeneous and the particles move randomly (Fig. 4.1a). For values right below the transition point, as in Fig. 4.1b, clusters start to appear on small distance-scales, but these still move around randomly and are pulled apart easily due to the fluctuations. Bands appear right above the transition point, Fig. 4.1c and Fig. 4.1d, and move in a fixed direction, while particles outside these bands still move randomly. The highly increased density in these bands can be quantified by projecting the density on the direction parallel and perpendicular to the projection of motion as in Fig. 4.2. As mentioned by Dossetti and Sevilla, these bands are not as dense and much wider than those observed in the original Vicsek model (Fig. 2.3) [DS15]. A possible explanation for the bands being more spread out in this model is that, even though they move in the same direction, the particles can move at highly varying speeds so that the slower particles will lag behind and the bands become elongated. For very high coupling factors, clustering is stronger so that the bands disappear and the whole system will move in one direction (Fig. 4.1e).

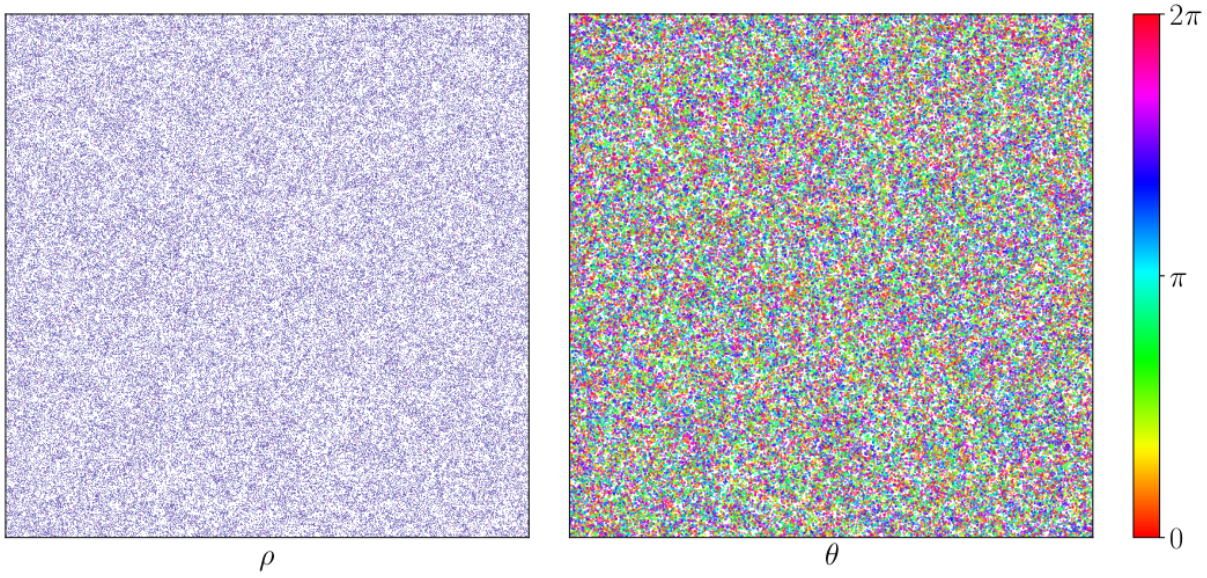

(a) $\tilde{\Gamma} = 2.00$

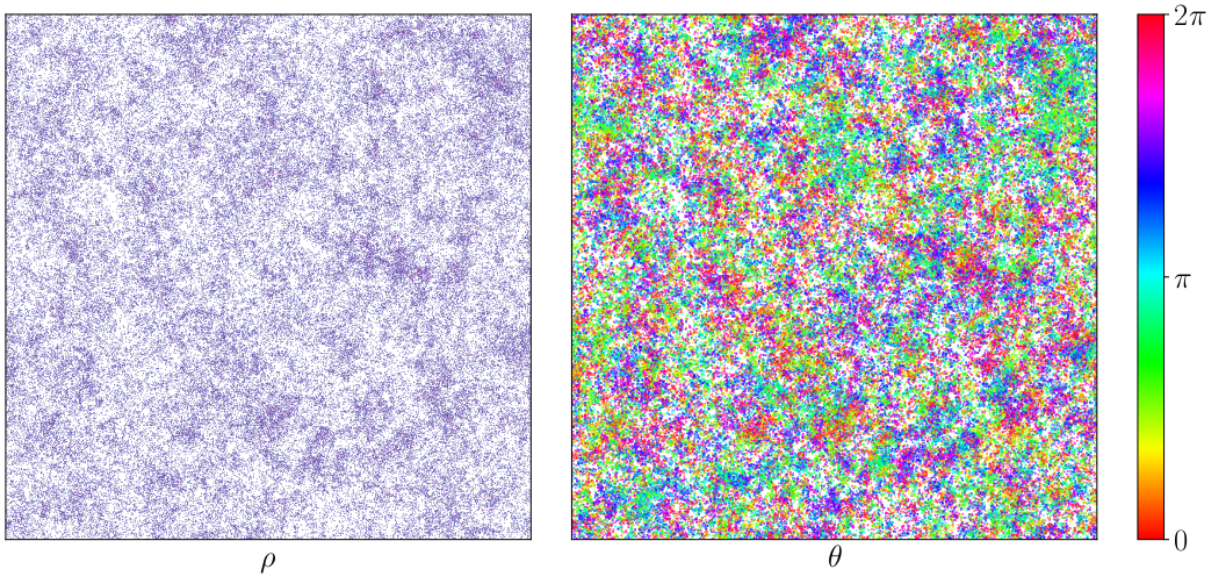

(b) $\tilde{\Gamma} = 2.64$

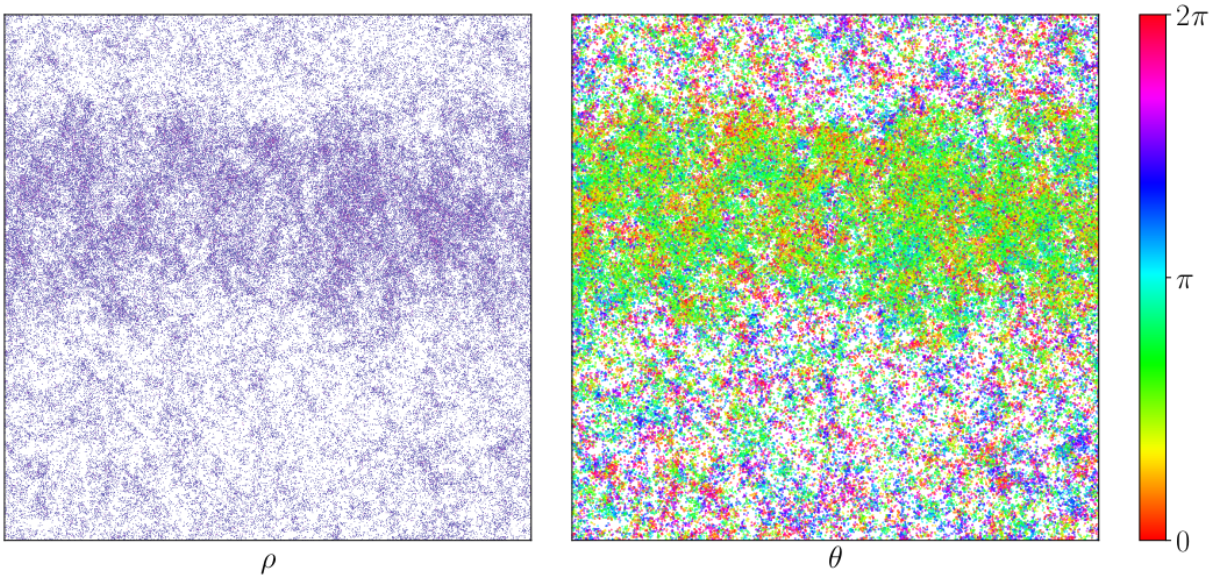

(c) $\tilde{\Gamma} = 2.90$

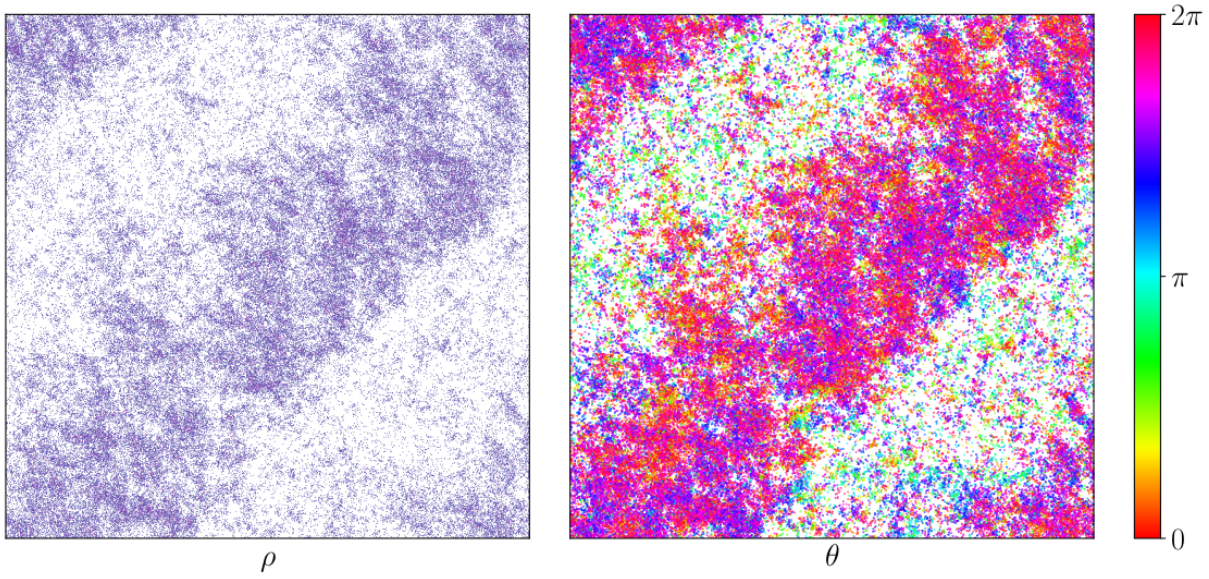

(d) $\tilde{\Gamma} = 3.50$

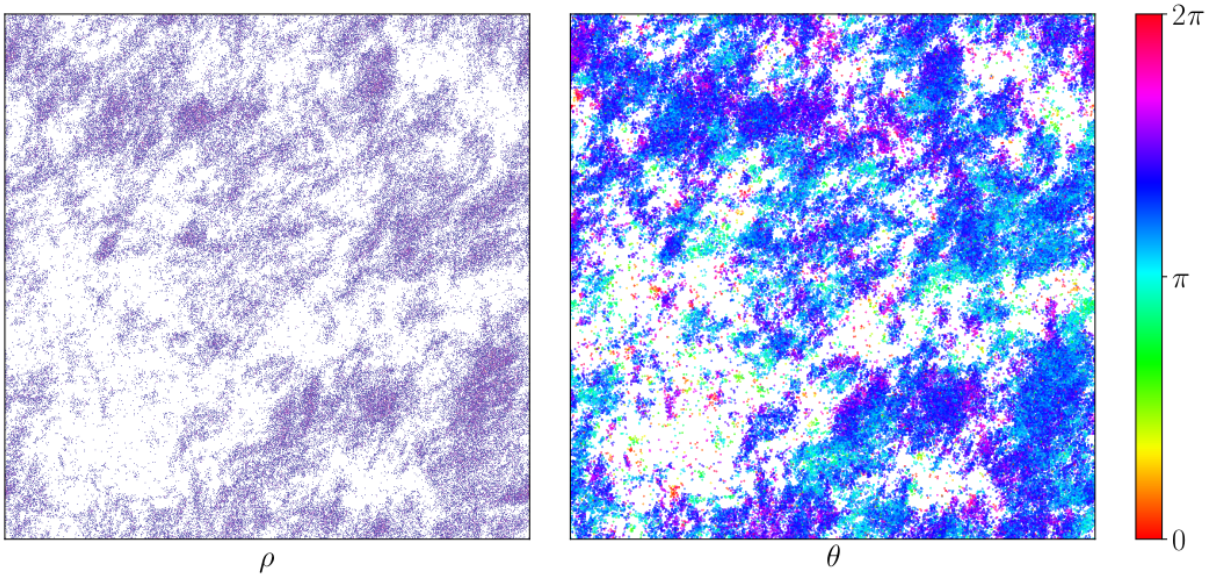

(e) $\tilde{\Gamma} = 8.00$

Fig. 4.1.: Particle density ρ and direction θ of particles in a system with $L = 192$ and $\tilde{\rho} = 4$, for different values of the coupling factor. The colourbar on right denotes a particle's direction, measured counter-clockwise with regard to the horizontal.

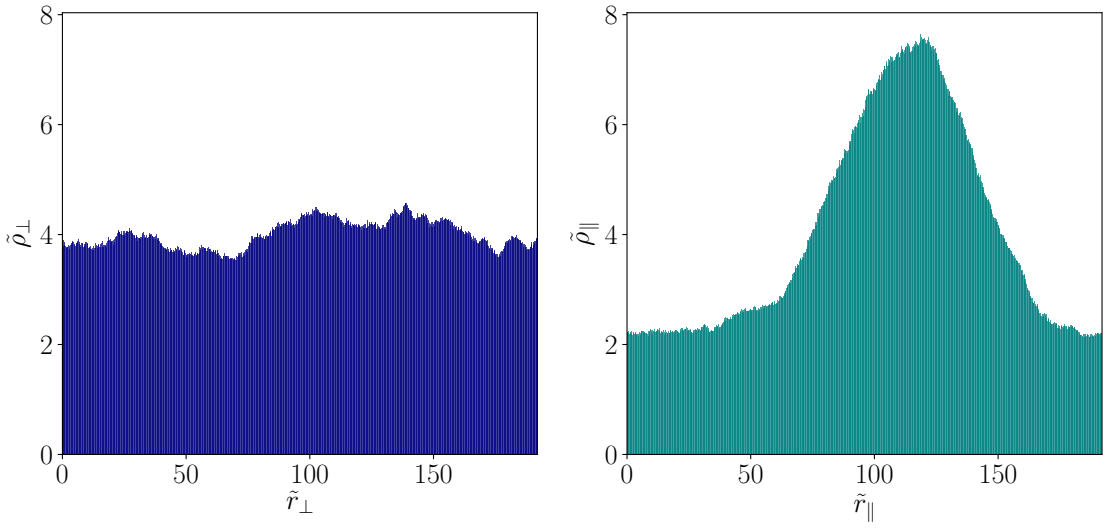

Fig. 4.2.: Density projected on the axis perpendicular to the mean direction of motion, $\tilde{\rho}_\perp$ and projected on the axis parallel to it, $\tilde{\rho}_\parallel$, for the system shown in Fig. 4.1c.

4.2 Spatial Correlations

4.2.1 Spatial correlation of the direction of motion.

Due to the aligning force, nearby particles will adopt the same direction of motion. For low values of the coupling factor, the aligning force will be cancelled out by the noise and its effect does not reach far beyond the interaction range. On the other hand, for a very strong social force, all particles will move in the same direction. This effect can be described by the following correlation function, which measures the alignment of particles separated by a distance $\tilde{r}_{ij}$:

$$C_\theta(\tilde{r}_{ij}) = \left\langle \frac{\tilde{\boldsymbol{v}}_i \cdot \tilde{\boldsymbol{v}}_j}{\tilde{v}_i \tilde{v}_j} \right\rangle_{i,j} . \tag{4.1}$$

The average is taken over all particle pairs (i, j) that are separated by the distance $\tilde{r}_{ij}$. The correlation function gives an indication of whether a change in direction of a particle has an effect on another particle separated a distance $\tilde{r}_{ij}$. It is equal to 1 for perfectly aligned particles, -1 if the particles are anti-aligned and 0 for uncorrelated particles [RL13]. Fig. 4.3 shows how this correlation function varies with the strength of the aligning force. The results shown are averaged over 100 snapshots sampled out of a simulation of 10^4 time steps after reaching steady state.

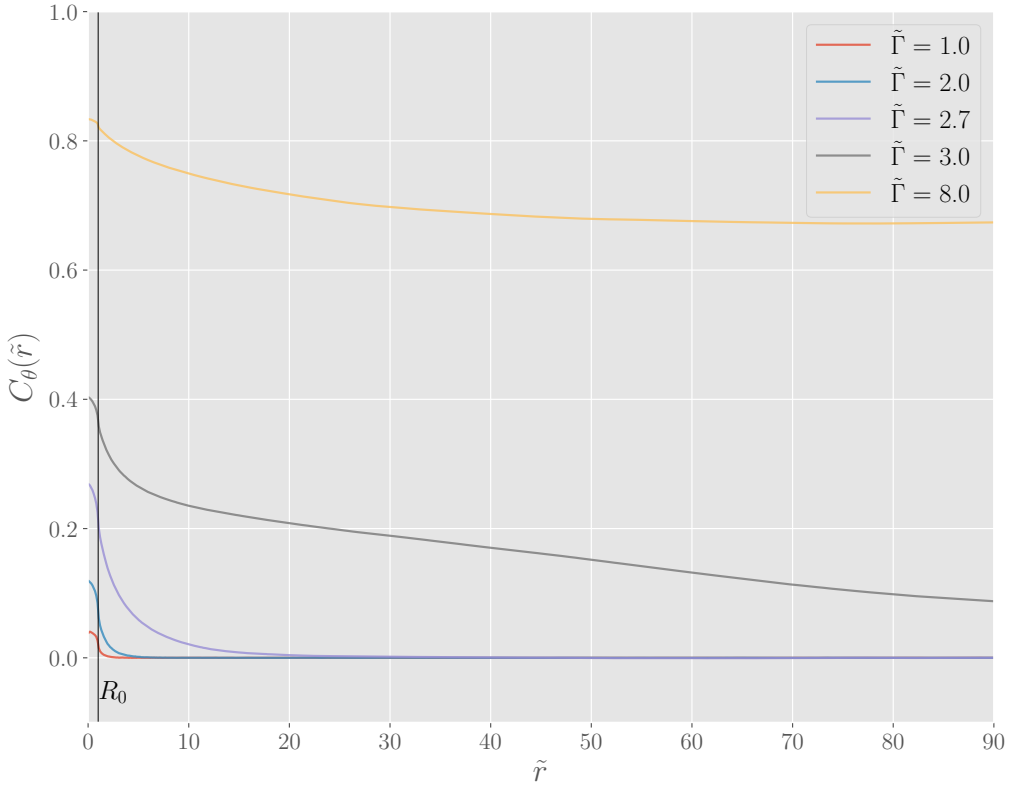

Fig. 4.3.: Time-averaged correlation function $C_\theta(\tilde{r})$ of the particle orientations in function of the distance $\tilde{r}$, for a system with $L = 192$ and $\tilde{\rho} = 4$.

Even when no collective motion is present on a macroscopic scale, the particle orientations are correlated on a small distance-scale, which increases with $\tilde{\Gamma}$. The correlations are small in this regime and the orientation of particles separated by a distance of a few times the interaction range – indicated by the vertical line – become independent of one another. After the transition to collective motion ($\tilde{\Gamma} \approx 2.72$), the orientation of particles separated by a large distance is still correlated and decays slowly.

4.2.2 Radial distribution function

To quantify the structure that gets formed due to the alignment interaction, the radial distribution function $g(r)$ is introduced in this section. This function measures the spatial correlation in the density of the particles. For uncorrelated particles, the probability of finding a particle at a distance r is simply proportional to the density ρ. Should spatial correlations appear in the system, $g(r)$ is a measure for the non-uniformity of the spatial distribu-

tion. When choosing one particular particle as the origin and working in 2 dimensions, $\rho g(r)\mathrm{d}^2 r$ is defined to be the average number of particles within a distance r and $r + \mathrm{d}r$ of the origin.

To calculate $g(r)$, a reference particle is chosen and concentric circles, separated by a distance $\mathrm{d}r$, are drawn around it [GT10]. The number of particles, $n(r)$, in every shell is counted and then divided by the area of the shell and the average particle density. The radial distribution function $g(r)$ can then be found by averaging this over all particles:

$$g(r) = \frac{\langle n(r) \rangle}{2\pi\rho r \mathrm{d}r}. \tag{4.2}$$

Fig. 4.4 shows the measured radial distribution function. As expected, it remains unity when $\tilde{\Gamma} = 0$ as the particles are non-interacting. For small but non-zero values of the coupling factor, the radial distribution function is greater than one for a small zone around the origin. The size of this zone grows as the coupling factor increases and extends the interaction range (indicated by the vertical line) even when no collective motion is yet present. In this phase, the clusters being formed are not long-lived since the alignment effect is weaker than the fluctuations. The system is still uniform on a large scale, which causes the radial distribution function $g(r)$ to decay back to one. Once the system develops collective motion in the form of bands, $g(r)$ is highly increased for a large range around the origin. The decay to values less than unity can be understood by considering that the 'average' particle is part of the band, so that at large radii the low density sea of disorderly moving particles is probed. For coupling factors that are higher still, the decay of $g(r)$ is faster since the clusters in this phase do not extend across the whole system.

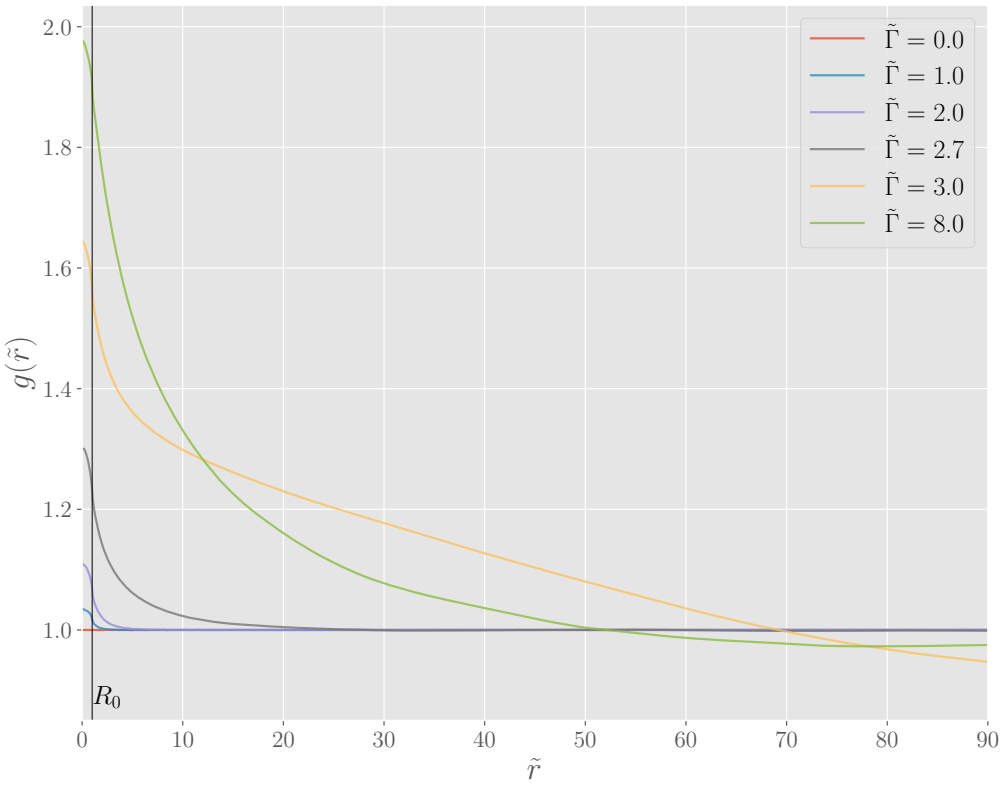

Fig. 4.4.: Time-averaged radial distribution function $g(\tilde{r})$ in function of the distance $\tilde{r}$, for a system with $L = 192$ and $\tilde{\rho} = 4$.

4.3 Cluster Size Distribution

4.3.1 Observations

For values of the coupling factor above the transition value, the particles in the system will align their motion and will move in clusters as a result. These clusters are dynamic, as they can split up due to stochastic fluctuations or merge with one another. In this section, the cluster size distribution in the bands phase of the Vicsek model for passive particles is discussed. Following the work of Huepe and Aldana, a cluster is defined recursively: two particles belong to the same cluster if they are within one another's interaction range or if there is a path of particles that connects them [HA04].

A significant difference with results obtained for the cluster size distribution in the active Vicsek model is that, for the model studied here, the much wider

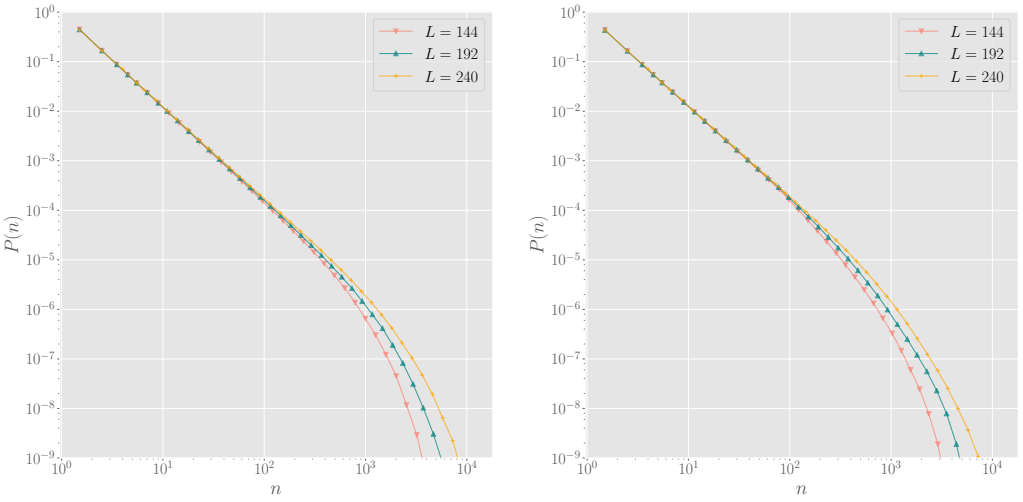

Fig. 4.5.: Distribution of cluster sizes (excluding the band) for (a) $\tilde{\rho} = 4$ and $\tilde{\Gamma} = 3.5$ and (b) $\tilde{\rho} = 3$ and $\tilde{\Gamma} = 3.8$.

band will form one giant cluster. For the densities studied here, it will contain the majority of the total particles: approximately 85% for $\tilde{\rho} = 4$ and 82% for $\tilde{\rho} = 3$. Nevertheless, there still is some structure to be found in the sea of particles in which these bands move. The cluster size distribution $P(n)$ gives the probability to find a cluster containing n particles in the system (where the band is not included). This distribution is shown for several system sizes in Fig. 4.5 in the case of $\tilde{\rho} = 4$ and $\tilde{\rho} = 3$. For both of the densities shown here, the coupling factor was chosen so that $\langle \Lambda \rangle \approx 0.5$. Using the 'powerlaw' package for Python [Als+14], a power-law distribution[1] gives an excellent fit for $4 \leq n \ll N$. The power-law exponent is dependent on the system size as, for example, it varies between $\mu \approx 1.92$ for the smallest system and $\mu \approx 1.84$ for the largest system studied with $\tilde{\rho} = 4$. However, all these distributions display a sharp cut-off in their tail. Such a cut-off is expected, as the the largest cluster that can be formed is dependent on the total number of particles. To search for the underlying distribution of these cluster sizes, a finite-size scaling analysis is performed in the next section.

[1] A short summary on the basic properties of power-law distributions is given in Append B.

4.3.2 Finite-size scaling

To explain the size-effects of the previous section and find the underlying distribution of the cluster sizes, a finite-size scaling ansatz of the following form can be proposed [CM05]:

$$\begin{aligned} P(n, L) &\propto n^{-\mu} \mathcal{G}\left(\frac{n}{n_c}\right), \\ n_c(L) &\propto L^D, \end{aligned} \tag{4.3}$$

where the cluster dimension D and a cut-off cluster size n_c were introduced. $\mathcal{G}$ is the scaling function, and should decay rapidly when n is greater than the cut-off cluster size.

The cluster-size exponent μ and dimension D can be found by comparing how the moments $\left\langle n^k \right\rangle$ vary with the system size L [DM+98; CM05]. The k-th moment is defined as

$$\left\langle n^k \right\rangle = \sum_{n=1}^{\infty} n^k P(n, L). \tag{4.4}$$

Using the finite-size scaling ansatz from Eq. 4.3, this can be rewritten as [CM05]

$$\begin{aligned} \left\langle n^k \right\rangle &= \sum_{n=1}^{\infty} n^{k-\mu} \mathcal{G}\left(\frac{n}{L^D}\right) \\ &\propto \int_1^{\infty} n^{k-\mu} \mathcal{G}\left(\frac{n}{L^D}\right) \mathrm{d}n \\ &= \int_{1/L^D}^{\infty} \left(\theta L^D\right)^{k-\mu} \mathcal{G}(\theta) L^D \mathrm{d}\theta \\ &= L^{D(1+k-\mu)} \int_{1/L^D}^{\infty} \theta^{k-\mu} \mathcal{G}(\theta) \mathrm{d}\theta. \end{aligned} \tag{4.5}$$

In the second-to-last line, the change of variable $n \to \theta = n/L^D$ was made. The rapid decay of $\mathcal{G}(\theta)$ has as effect that this integral converges in the upper limit, while if k is chosen so that $\mu < 1 + k$, it is ensured to converge in the lower limit as well. Taking the logarithm on both sides of Eq. (4.5) allows one to write

$$\log \left\langle n^k \right\rangle = D(1 + k - \mu) \log L + C, \tag{4.6}$$

with C a constant. When measuring the k-th moment in function the system size L and then plotting this on a logarithmic scale, the slope of this line gives

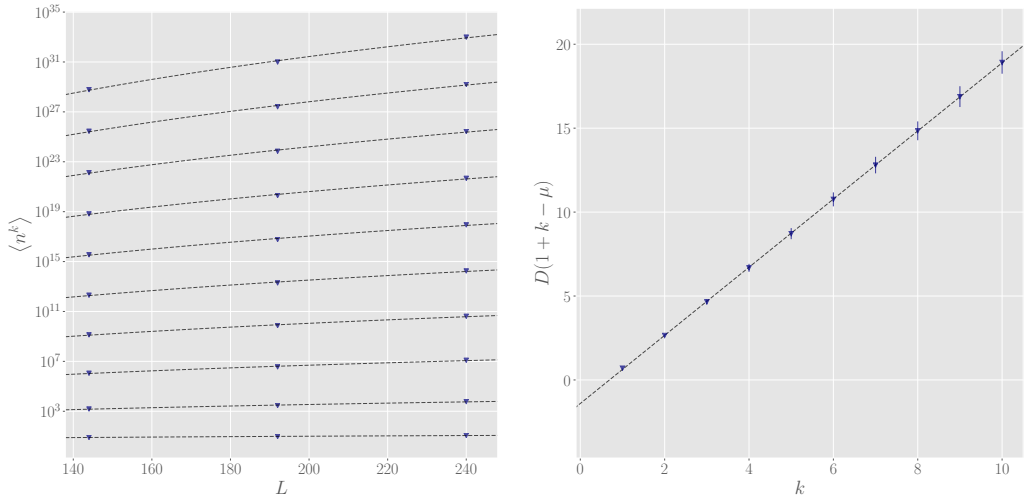

(a) **(b)**

Fig. 4.6.: (a) Scaling of the moments of the cluster size distribution with system size (b) Estimation of D and μ using the moments analysis.

an estimate for $D(1+k-\mu)$. By plotting these estimates for every moment k measured, a straight line with slope D is obtained. This line intersects the k-axis at $k = \mu - 1$, so that the cluster-size exponent μ can be found from this. Fig. 4.6 shows this analysis for $\tilde{\rho} = 4$. From this, the power-law exponent $\mu = 1.69 \pm 0.02$ and the cluster dimension $D = 2.01 \pm 0.01$ were calculated. A similar analysis for $\tilde{\rho} = 3$ leads to $\mu = 1.67 \pm 0.02$ and $D = 2.00 \pm 0.02$. This means that for both system sizes, the cut-off cluster size scales linearly with the number of particles.

Fig. 4.7 and Fig. 4.8 show a data collapse of the cluster size distribution measured for three system sizes. First, the distribution is multiplied by n^{μ} so that the distinctive tail is vertically aligned. When rescaling the variable $n \to \theta = n/L^D$, the distribution of the three system sizes falls on the same line.

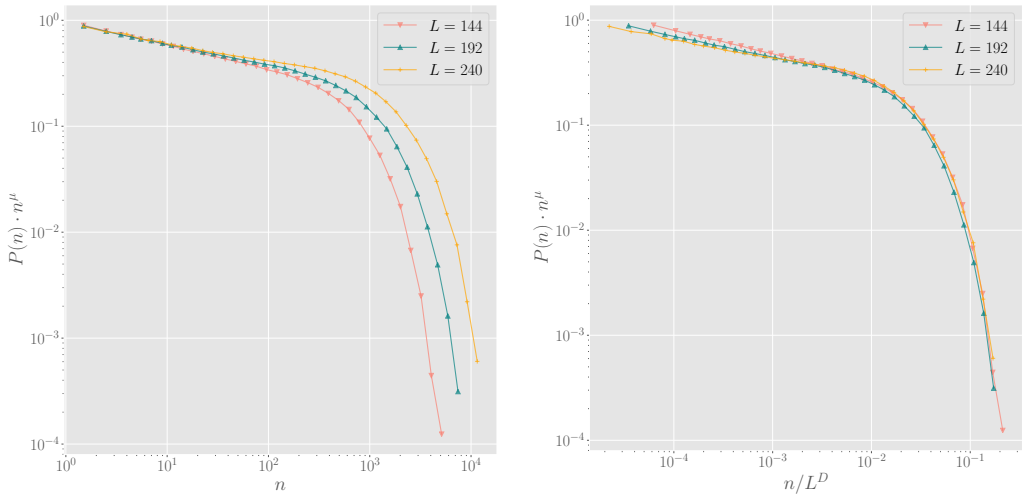

(a) **(b)**

Fig. 4.7.: Data collapse of the cluster size distribution for $\tilde{\rho} = 4$ and $\tilde{\Gamma} = 3.5$. (a) shows $P(n)n^{\mu}$ in function of the cluster size n, while (b) shows this in function of the rescaled cluster size n/L^D.

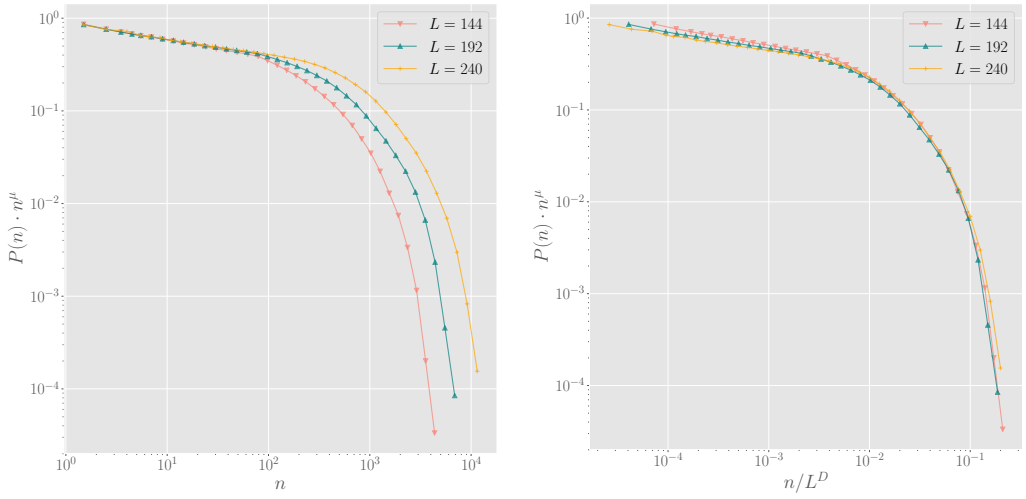

(a) **(b)**

Fig. 4.8.: Data collapse of the cluster size distribution for $\tilde{\rho} = 3$ and $\tilde{\Gamma} = 3.8$. (a) shows $P(n)n^{\mu}$ in function of the cluster size n, while (b) shows this in function of the rescaled cluster size n/L^D.

Judging by the obtained data collapse, the scaling ansatz suggested in Eq. (4.3) seems to explain the finite-size effects observed in the measurements for the three sizes studied. This would indicate that in the limit $L \to \infty$, the cluster size is distributed according to a power-law with an exponent less than 2, so that the mean cluster size would diverge. Yet, it is dangerous to draw a conclusion from the measurements made here. For systems larger than those taken under study, the original Vicsek model displays several evenly spaced bands rather than a single one. A further investigation would have to be made to observe if the bands also split up for the model by Dossetti and Sevilla and whether this has any effect on the cluster size distribution.

5 Entropy Production

5.1 Entropy and (ir)reversibility

If a system has a discrete set of microstates, labeled as i, and p_i is the probability for the microstate i to occur, then the Gibbs entropy is given by

$$S = -k_b \sum_i p_i \ln p_i, \tag{5.1}$$

where k_b is the Boltzmann constant. The entropy is related to disorder, as it increases with the amount of microstates. The second law of thermodynamics states that the entropy of a closed system does not decrease:

$$\Delta S \geq 0. \tag{5.2}$$

The equality must hold for a reversible process: should the entropy production for such a process be positive, $\Delta S > 0$, then the reversed process would have $\Delta S < 0$ – a clear violation of the second law. In a non-equilibrium system, entropy can be produced constantly, which is discussed in the next section.

5.2 Introduction to Non-Equilibrium Entropy Production

An instructive example of entropy production can be found in an overdamped Brownian particle, moving in one dimension and subjected to a position- and time-dependent force F [Sei05]. The equation of motion[1] for such a particle is given by

$$\gamma \frac{\mathrm{d}x}{\mathrm{d}t} = F(x,t) + \xi(t), \tag{5.3}$$

[1] In the remainder of this chapter, the Boltzmann constant k_B is set to unity.

where γ is the friction coefficient and ξ is Gaussian white noise with zero mean and $\langle \xi(t)\xi(t') \rangle = 2\gamma T \delta(t-t')$. The force F is a combination of an external driving force and a force derived from a conservative potential, V.

The definition of the non-equilibrium Gibbs entropy at time τ is given by

$$S(\tau) = -\int \mathrm{d}x \; p(x,\tau) \ln p(x,\tau). \tag{5.4}$$

Here, $p(x,\tau)$ is the probability to find the particle at a position x and time τ. This definition allows one to write the trajectory-dependent entropy as [Sei05; Sah+09]

$$s(\tau) = -\ln p(x(\tau),\tau), \tag{5.5}$$

where $p(x,\tau)$ is evaluated along the stochastic trajectory $x(t)$. As for all trajectories, $s(\tau)$ will depend on the initial configuration $p_0(x)$, this contains information on the whole ensemble. The Gibbs entropy can be recovered by averaging over all trajectories:

$$S(\tau) = \langle s(\tau) \rangle . \tag{5.6}$$

For a particle obeying the equation of motion given by Eq. (5.3) with a force only dependent on position and time, the entropy production is a combination of the system and the environmental entropy production [Sah+09]. The system entropy production for a trajectory of duration τ is given by

$$\Delta s_{sys} = -\ln p(x(\tau),\tau) + \ln p_0(x(0),0) = -\ln \frac{p(x(\tau),\tau)}{p_0(x(0),0)}, \tag{5.7}$$

where $p_0(x,0)$ is the initial distribution of the particle positions at $t=0$ and $p(x,\tau)$ is the distribution at $t=\tau$ evolving from the initial positions.

The work applied to the system consists of a contribution from the change in potential energy and the application of the external force [Sei08]. Sekimoto showed that an equation similar to the first law of thermodynamics can be constructed from the energy balance of the whole system: [Sek98]

$$\mathrm{d}W = \mathrm{d}V + \mathrm{d}Q, \tag{5.8}$$

where $\mathrm{d}W$ is the work applied to the system along the followed trajectory and $\mathrm{d}Q$ is the heat discarded[2] from the system to the heat bath. Furthermore,

[2]Note that the sign convention used in this definition is opposite to what is usually found in literature on macroscopic thermodynamics.

by considering the energetics of the Langevin equation, he proved that this heat can be written as

$$Q = -\left(-\gamma\frac{\mathrm{d}x}{\mathrm{d}t} + \xi\right)\mathrm{d}x. \tag{5.9}$$

The heat dissipation into the bath will produce an increase in the environmental entropy equal to

$$\Delta s_{env} = \frac{Q}{T}. \tag{5.10}$$

The increase in environmental entropy can be written in the stochastic trajectory framework used here as [Kur98]

$$\Delta s_{env} = \frac{Q}{T} = \ln\frac{\mathcal{P}[x(t)|x(0)]}{\mathcal{P}^R[x(\tau-t)|x(\tau)]}, \tag{5.11}$$

where $\mathcal{P}[x(t)|x(0)]$ is the conditional path probability of the particle evolving along the trajectory $x(t)$ during a time τ when starting at $x(0)$ for $t = 0$. The denominator is the time-reversed version of this, so that their ratio is a measure for the reversibility of the process. In an equilibrium process, time-reversibility means that Eq. (5.11) will be equal to zero.

The total entropy production, Δs_{tot}, is given by the sum of Eqs. (5.7) and (5.11):

$$\Delta s_{tot} = \ln\frac{\mathcal{P}[x(t)|x(0)]p_0(x(0),0)}{\mathcal{P}^R[x(\tau-t)|x(\tau)]p(x(\tau),\tau)}. \tag{5.12}$$

The expected value of $e^{-\Delta s_{tot}}$ can be written as [Sei05]

$$\left\langle e^{-\Delta s_{tot}}\right\rangle = \sum_{x(t),x(0)} \mathcal{P}[x(t)|x(0)]p_0(x(0),0)e^{-\Delta s_{tot}}, \tag{5.13}$$

in which the sum averages over the initial distribution and the following stochastic trajectories. Using Eq. (5.12), this can be written as

$$\begin{aligned}\left\langle e^{-\Delta s_{tot}}\right\rangle &= \sum_{x(\tau-t),x(\tau)} \mathcal{P}^R[x(\tau-t)|x(\tau)]p(x(\tau),\tau) \\ &= 1,\end{aligned} \tag{5.14}$$

which is a consequence of the normalization of the probabilities. Jensen's inequality states that for a convex function f and a random variable x the relation $\langle f(x)\rangle \geq f(\langle x\rangle)$ holds, so it follows from Eq. (5.14) that

$$\langle \Delta s_{tot}\rangle \geq 0. \tag{5.15}$$

Eq. (5.14) is called the integral fluctuation theorem. This universal theorem holds for any time duration and initial condition [Sei08]. It implies that if entropy-producing trajectories exist in a system, there must also be trajectories with a *negative* entropy production so that Eq. (5.14) still holds: the second law of thermodynamics is a statistical one.

5.3 Unconventional Entropy Production

The equation for the total entropy production,

$$\begin{aligned} \Delta S_{tot} &= \Delta S_{sys} + \Delta S_{env} \\ &= \Delta S_{sys} + \frac{Q}{T}, \end{aligned} \tag{5.16}$$

as derived in the previous section, only holds if the force is not dependent on variables that have odd-parity under time-reversal such as the momentum of the particle. If the particles in the system are subjected to momentum-dependent forces, the environmental entropy production is not solely given by the heat Q transferred to the reservoir. Instead, an additional term, called the unconventional entropy production (ΔS_{unc}) appears so that $\Delta S_{env} = \Delta S_{res} + \Delta S_{unc}$ [Kwo+16]. Here, ΔS_{res} is the entropy production related to the heat transfer. For some systems it was shown that ΔS_{res} is in fact negative, so that the addition of ΔS_{unc} is required for ΔS_{tot} to follow the second law. The study of unconventional entropy production is a very recent one, and no intuitive explanation has been provided for it as of yet.

To derive the unconventional entropy production, one starts from a general Langevin equation

$$\begin{cases} \dfrac{\mathrm{d}\boldsymbol{x}}{\mathrm{d}t} &= \dfrac{\boldsymbol{p}}{m}, \\ \dfrac{\mathrm{d}\boldsymbol{p}}{\mathrm{d}t} &= \boldsymbol{F}(\boldsymbol{q};\lambda(t)) - \gamma\dfrac{\boldsymbol{p}}{m} + \boldsymbol{\xi}, \end{cases} \tag{5.17}$$

where $\boldsymbol{q} = (\boldsymbol{x}, \boldsymbol{p})$ denotes the state in phase space of the particle and $\lambda(t)$ is an arbitrary time-dependent function on which the force depends. It is important to consider how the system behaves under time-reversal: $\boldsymbol{\epsilon q}$ denotes the behaviour of $\boldsymbol{q}$ under this operation. Since the positional coordinates have even parity under time-reversal, it follows from $\boldsymbol{p} \sim \frac{\mathrm{d}\boldsymbol{x}}{\mathrm{d}t}$ that the parity of the momentum under time-reversal is odd, so that $\boldsymbol{\epsilon q} = (\boldsymbol{x}, -\boldsymbol{p})$. The force $\boldsymbol{F}$ can consist of a reversible and irreversible part under time-reversal

$$\begin{gathered} \boldsymbol{F} = \boldsymbol{F}^{\text{rev}} + \boldsymbol{F}^{\text{ir}}, \\ \text{where} \\ \boldsymbol{F}^{\text{rev}}(\boldsymbol{q}) = \frac{1}{2}(\boldsymbol{F}(\boldsymbol{q}) + \boldsymbol{F}(\boldsymbol{\epsilon q})), \\ \boldsymbol{F}^{\text{ir}}(\boldsymbol{q}) = \frac{1}{2}(\boldsymbol{F}(\boldsymbol{q}) - \boldsymbol{F}(\boldsymbol{\epsilon q})). \end{gathered} \tag{5.18}$$

With this definition, $\boldsymbol{F}^{\text{rev}}(\boldsymbol{\epsilon q}) = \boldsymbol{F}^{\text{rev}}(\boldsymbol{q})$ and $\boldsymbol{F}^{\text{ir}}(\boldsymbol{\epsilon q}) = -\boldsymbol{F}^{\text{ir}}(\boldsymbol{q})$ [Kwo+16].

The total entropy production for a trajectory from $t = 0$ to $t = \tau$ is again given by

$$\Delta s_{tot} = \ln \frac{\mathcal{P}[\boldsymbol{q}(t); \lambda(t)|\boldsymbol{q}(0)]p(\boldsymbol{q}(0), 0)}{\mathcal{P}^R[\boldsymbol{\epsilon q}(\tau - t); \lambda(\tau - t)|\boldsymbol{\epsilon q}(\tau)]p(\boldsymbol{q}(\tau), \tau)}. \tag{5.19}$$

Here, the system starts from a configuration $\boldsymbol{q}(0)$ at time $t = 0$ and follows the stochastic path $\boldsymbol{q}(t)$. $\mathcal{P}[\boldsymbol{q}(t); \lambda(t)|\boldsymbol{q}(0)]$ is the conditional probability that this path is followed when starting from the configuration $\boldsymbol{q}(0)$. Combining this with the probability to find the initial value, $p(\boldsymbol{q}(0), 0)$, provides an expression for the forward path probability. The denominator is the time-reversed version of this. As the system entropy production over a time τ is given by

$$\Delta s_{sys} = -\ln p(\boldsymbol{q}(0), 0) + \ln p(\boldsymbol{q}(\tau), \tau), \tag{5.20}$$

the environmental entropy production can be identified by the logarithm of the ratio of the two conditional path probabilities.

An expression for the environmental entropy production is found by considering the change in the environmental entropy during a short time interval of length $\mathrm{d}t$ [Kwo+16; Yeo+16]. This quantity is given by

$$\mathrm{d}S_{env} = \ln \frac{\Gamma(\boldsymbol{q}', t + \mathrm{d}t|\boldsymbol{q}, t)}{\Gamma(\boldsymbol{\epsilon q}, t + \mathrm{d}t|\boldsymbol{\epsilon q}', t)}, \tag{5.21}$$

where $\Gamma(\boldsymbol{q}', t + \mathrm{d}t|\boldsymbol{q}, t)$ stands for the conditional probability to evolve from the state $\boldsymbol{q}$ at time t to $\boldsymbol{q}'$ at time $t + \mathrm{d}t$. Following Markovian dynamics, the conditional probability $\mathcal{P}$ over the entire time interval can be recovered from the product of these Γ's and taking the limit $\mathrm{d}t \to 0$. These transition probabilities can be calculated using a Fokker-Planck equation. Consequently, it can be shown that Eq. (5.21) can be rewritten as [Yeo+16]

$$\mathrm{d}S_{env} = \frac{\mathrm{d}t}{D}\Big(\dot{\boldsymbol{p}} - \boldsymbol{F}^{\mathrm{rev}}(\bar{\boldsymbol{q}})\Big)\left(-\gamma\frac{\bar{\boldsymbol{p}}}{m} + \boldsymbol{F}^{\mathrm{ir}}(\bar{\boldsymbol{q}})\right) - \mathrm{d}t\ \partial_{\boldsymbol{p}}\boldsymbol{F}^{\mathrm{rev}}(\bar{\boldsymbol{q}}). \tag{5.22}$$

Here, D is the diffusion coefficient, $\dot{\boldsymbol{q}} = (\boldsymbol{q}' - \boldsymbol{q})/\mathrm{d}t$ and $\bar{\boldsymbol{q}} = (\boldsymbol{q}' + \boldsymbol{q})/2$. The position and momentum are thus evaluated at the mid-point, following the Stratonovich convention.

5.4 Entropy Production for Collective Motion

Shim et al. raised a question about the relation between the entropy production on a microscopic and macroscopic level, which they studied for a globally-coupled Vicsek model [Shi+16]. On a microscopic scale, the time-irreversibility caused by the momentum-dependent force implies the production of entropy on this level. One could expect that, for both the disordered and ordered phase, the entropy produced by each particle adds up to a macroscopic amount. However, if one takes a macroscopic point of view, all configurations in the disordered phase are equally likely. This would imply that irreversibility is not present in the disordered phase and the entropy production is only sub-extensive – which is to say that it does not linearly increase with the amount of particles.

For the model introduced in chapter 3, the force is purely momentum-dependent so that $\boldsymbol{F}^{\mathrm{rev}} = 0$. The environmental entropy production rate of Eq. (5.22) becomes

$$\frac{\mathrm{d}S_{env}}{\mathrm{d}t} = -\frac{\dot{\boldsymbol{p}}}{T}\cdot\frac{\bar{\boldsymbol{p}}}{m} + \frac{\dot{\boldsymbol{p}}}{\gamma T}\cdot\boldsymbol{F}(\bar{\boldsymbol{p}}), \tag{5.23}$$

in which the Einstein relation $D = \gamma T$ is used. The environmental entropy production for the whole system during a time τ can be rewritten as

$$\Delta S_{\text{env}} = -\frac{m}{T}\sum_{i=1}^{N}\int_0^\tau \boldsymbol{v}_i(t) \circ \mathrm{d}\boldsymbol{v}_i(t) + \frac{m}{\gamma T}\sum_{i=1}^{N}\int_0^\tau \boldsymbol{F}_i(t) \circ \mathrm{d}\boldsymbol{v}_i(t). \tag{5.24}$$

The summation runs over all particles in the system and the integrals are Stratonovich integrals. This is because the phase-space variables have to be evaluated at the mid-point between two time steps. An example of such an integral is

$$\int_0^\tau \boldsymbol{F}_i(t) \circ \mathrm{d}\boldsymbol{v}_i(t) = \sum_{j=0}^{n-1} \frac{\boldsymbol{F}_i((j+1)\Delta t) + \boldsymbol{F}_i(j\Delta t)}{2} \cdot \left(\boldsymbol{v}_i((j+1)\Delta t) - \boldsymbol{v}_i(j\Delta t)\right), \tag{5.25}$$

where the time interval τ was split up in n equal parts of length Δt, and the limit $\Delta t \to 0$ has to be taken.

By using $m\mathrm{d}\boldsymbol{v}_i = (m\mathrm{d}\boldsymbol{v}_i - \boldsymbol{F}_i\mathrm{d}t) + \boldsymbol{F}_i\mathrm{d}t$, Eq. (5.24) can be written as

$$\begin{aligned}\Delta S_{\text{env}} = &-\frac{1}{T}\sum_{i=1}^{N}\int_0^\tau \boldsymbol{v}_i(t) \circ (m\mathrm{d}\boldsymbol{v}_i - \boldsymbol{F}_i\mathrm{d}t) - \frac{1}{T}\sum_{i=1}^{N}\int_0^\tau \boldsymbol{v}_i(t) \circ \boldsymbol{F}_i\mathrm{d}t \\ &+ \frac{m}{\gamma T}\sum_{i=1}^{N}\int_0^\tau \boldsymbol{F}_i(t) \circ \mathrm{d}\boldsymbol{v}_i(t).\end{aligned} \tag{5.26}$$

The second term in this equation is zero as the force does no work. Eq. (5.26) illustrates that the environmental production is not merely equal to the heat flow into the reservoir. This term is given by (see Eq. (5.9))

$$\begin{aligned}Q &= -\sum_{i=1}^{N}\int_0^\tau \boldsymbol{v}_i(t) \circ (-\gamma\boldsymbol{v}_i + \boldsymbol{\xi}_i)\mathrm{d}t \\ &= -\sum_{i=1}^{N}\int_0^\tau \boldsymbol{v}_i(t) \circ \left(m\frac{\mathrm{d}\boldsymbol{v}_i}{dt} - \boldsymbol{F}_i\right)\mathrm{d}t,\end{aligned} \tag{5.27}$$

so that the first term in Eq. (5.26) is equal to $\dfrac{Q}{T}$. Additionally, a third term is added to the entropy production: the unconventional entropy production, introduced in the previous section. The total entropy production can be written as

$$\Delta S_{tot} = \Delta S_{sys} + \frac{Q}{T} + \Delta S_{unc}. \tag{5.28}$$

The change in energy of the system is just the change in the kinetic energy of the particles. The velocity distribution is stationary in steady state, so that the energy change is zero. As no work is being done on the system either, the first law of thermodynamics implies that the heat transfer Q in Eq. (5.28) is zero in steady state, which means that there is no reservoir entropy production. In this state, the spatial distribution is stationary too, so that the system entropy production will vanish likewise. The only entropy-producing term remaining of Eq. (5.28) in the steady state is the unconventional entropy production, ΔS_{unc}.

From the previous calculations, the entropy production rate per particle, s, can be determined:

$$s = \frac{1}{N}\left\langle \frac{\mathrm{d}S_{\mathrm{tot}}}{\mathrm{d}t} \right\rangle = \frac{m}{\gamma T}\frac{1}{N}\sum_{i=1}^{N}\left\langle \boldsymbol{F}_i \circ \frac{\mathrm{d}\boldsymbol{v}_i}{\mathrm{d}t} \right\rangle, \tag{5.29}$$

where $\langle . \rangle$ denotes the steady state average and the Stratonovich product appearing here is given by

$$\boldsymbol{F}_i \circ \frac{\mathrm{d}\boldsymbol{v}_i}{\mathrm{d}t} = \frac{\boldsymbol{F}_i(t+dt) + \boldsymbol{F}_i(t)}{2} \cdot \frac{\boldsymbol{v}_i(t+dt) - \boldsymbol{v}_i(t)}{\mathrm{d}t}. \tag{5.30}$$

5.4.1 Global interactions

As it is interesting to compare the results with a short-range version of the Vicsek model, the results for the entropy production in the case of a globally-coupled system are shown below (as in [Shi+16]). Note that the entropy production rate per particle remains very small until $\tilde{\Gamma} \approx 2.0$ and then increases. This transition point coincides with the onset of collective motion, as discussed for the globally-coupled model in section 3.4.

Furthermore, the fluctuation of the entropy production is calculated, which is defined as

$$\chi_S(\tau) = \frac{1}{\tau N}\left[\left\langle \Delta S^2 \right\rangle - \langle \Delta S \rangle^2\right], \tag{5.31}$$

where ΔS is the entropy produced during a time τ. This τ is chosen so that $\chi_S(\tau')$ converges to the same value for $\tau' \geq \tau$ [Shi+16]. The observation of the sharp peak, which slightly shifts with system size, is another indication of a continuous phase transition.

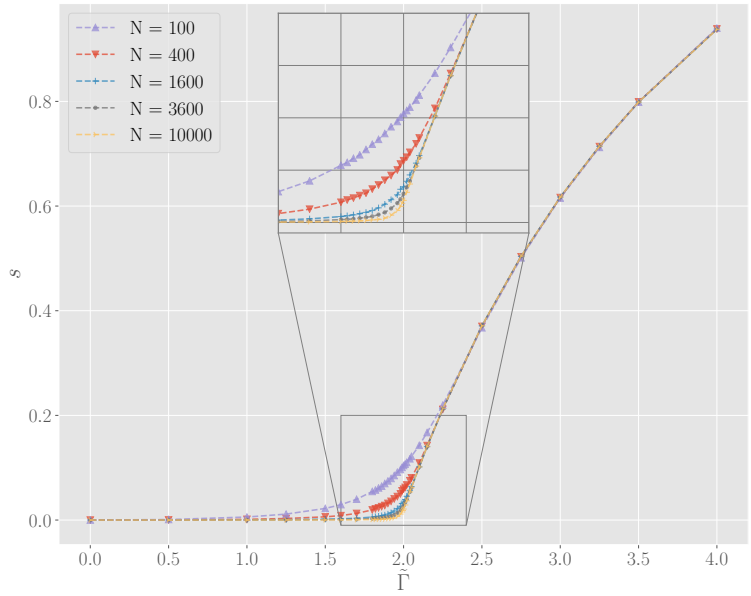

(a)

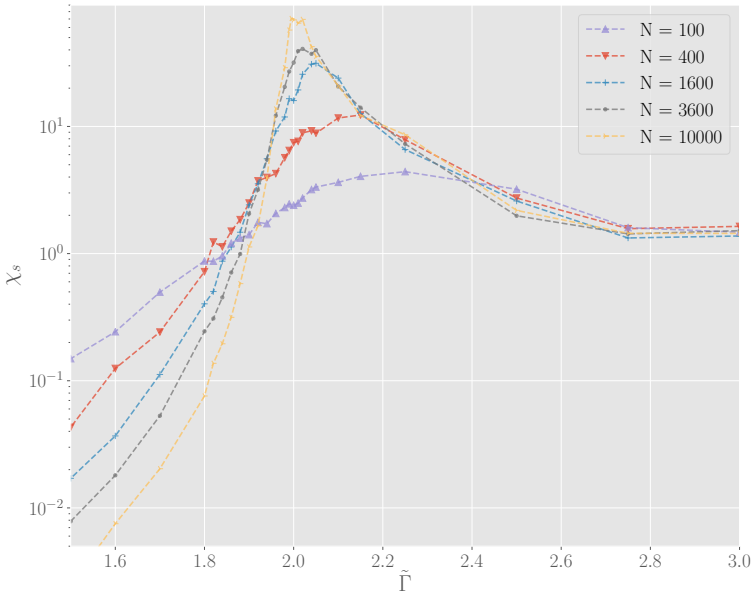

(b)

Fig. 5.1.: (a) The entropy production rate per particle s in function of the dimensionless coupling factor. (b) Susceptibility of the entropy production during a time $\tau = 200$.

Fig. 5.2 shows that the entropy production rate per particle is sub-extensive below the critical point, since s scales as $1/N$ [Shi+16]. As collective motion sets in, s remains at a constant value, indicating that the entropy production is extensive in this regime. To conclude, the entropy production rate in

the globally-coupled version of the model by Sevilla et al. displays a phase transition itself, changing from being sub-extensive to extensive at the onset of collective motion.

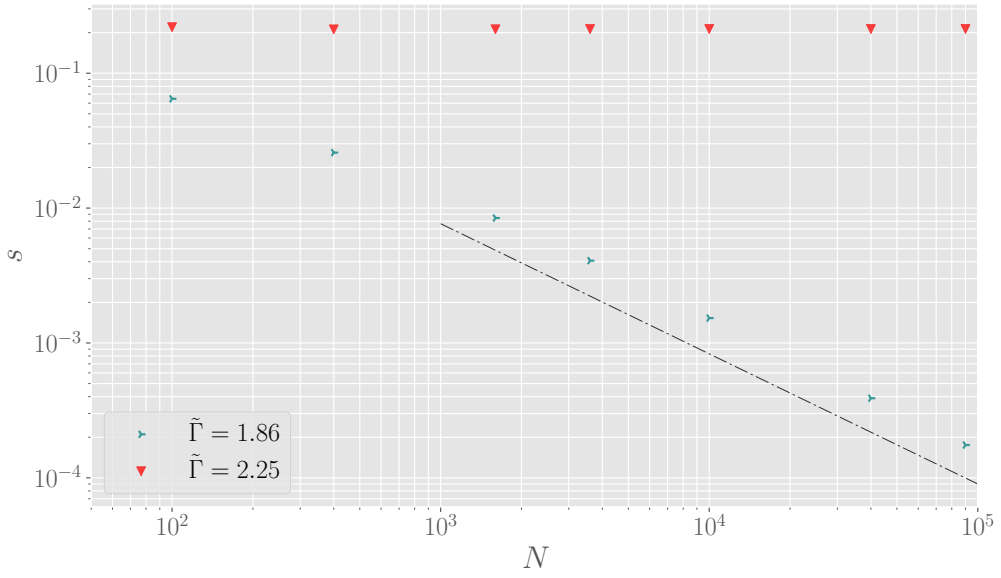

Fig. 5.2.: Scaling of the entropy production rate per particle, s, with N for a globally-coupled system. The dash-dotted line has a slope of -1.

5.4.2 Short-range interactions

When changing from global interactions – as in the previous section – to local interactions, the entropy production is drastically different. The entropy production rate per particle, s, is shown for a short-range model in Fig. 5.3. While the entropy production was sub-extensive for the disordered phase in the globally-coupled model, it is now extensive – so that s is independent of the system size. In addition, its value in this phase is much larger. At the transition to collective motion, s varies with the system size, but converges to a single value. This last effect can be understood by comparing the phase diagram of the short-range and globally-coupled model (Fig. 3.1 and Fig. 3.12). While the order parameter quickly converges to a value independent of the system size for the latter, this is not the case for the short-range model – which explains the size-dependence of the entropy production rate.

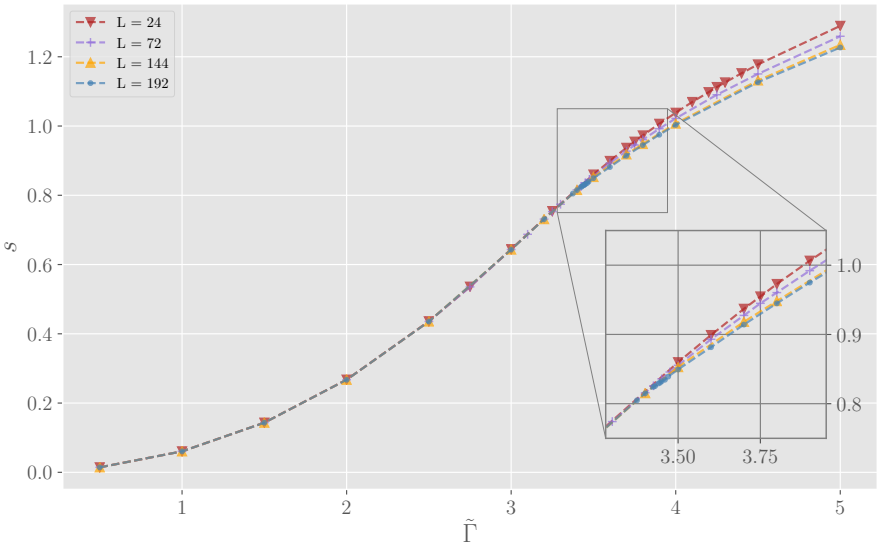

Fig. 5.3.: Entropy production rate per particle s in function of the dimensionless coupling factor $\tilde{\Gamma}$, for a system with $\tilde{\rho} = 2$.

The spatial correlations in the system could possibly explain the change from a sub-extensive to an extensive entropy production rate in the disordered phase. In the globally-coupled model, there are no such correlations as the alignment is independent of a particle's position. As discussed in section 4.2, however, the short-range force causes the directions of particles to be correlated over a small distance scale. Even though order is absent on a global level in the disordered phase of the short-range model, the denser zones in the system are locally more ordered than sparsely-packed zones. Since the previous section indicated that the onset of order was the cause of time-irreversibility, a hypothesis to explain the results obtained for the short-range model is the following: the extensive entropy production found in the disordered phase may be caused by the contribution of particles in the denser, locally ordered zones.

To test this hypothesis, the system was divided into square boxes of linear size l. The density, local order parameter and contribution to the unconventional entropy production of particles in a box were calculated. This local order parameter is defined as the norm of the average velocity in the box. The density and local order parameter are – just like the entropy production – measured at the mid-point between two time steps. If the hypothesis proposed in the previous section were to hold true, it is expected that a particle in a box with a high value of the local order parameter will, on average, also

have a relatively high contribution to the unconventional entropy production. To this aim, measurements were conducted for the system shown in Fig. 4.1b. While still not collectively moving, this system shows highly increased spatial correlations. Fig. 5.4 displays the results obtained from these measurements. Unlike what would be expected from the hypothesis, the local entropy production does not seem to increase with higher local order. The obtained results suggest that the reason for the change in the nature of the entropy production when introducing short-range interactions may lie elsewhere.

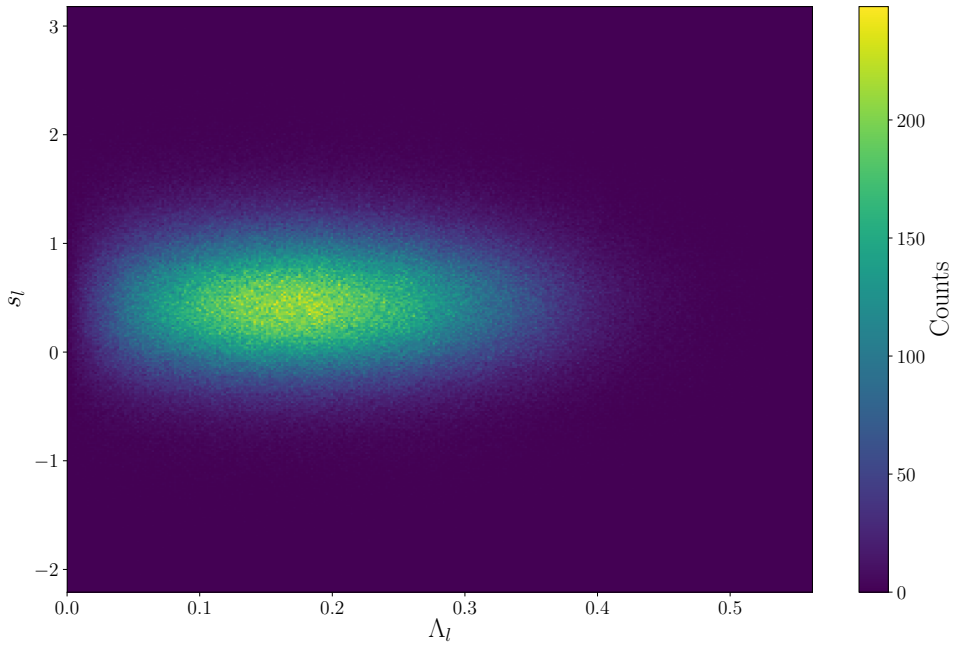

Fig. 5.4.: Local entropy production s_l, in function of the local order parameter Λ_l, for the system shown in Fig. 4.1b. These results were obtained by dividing the system in boxes of linear size $l = 8$.

6 Mean-Field Model for Passive Particles

6.1 From a Fokker-Planck Equation to Dynamical Moment Equations

The probability density function $P(\boldsymbol{r}, \boldsymbol{v}, t)$ describes the probability of finding a particle with coordinates between $\boldsymbol{r}$ and $\boldsymbol{r} + \mathrm{d}\boldsymbol{r}$, and a velocity between $\boldsymbol{v}$ and $\boldsymbol{v} + \mathrm{d}\boldsymbol{v}$ at time t. The knowledge of this probability density function allows for the calculation of the various moments of the velocity distribution. The n-th moment of the velocity component along the direction k is defined as

$$\langle v_k^n \rangle = \frac{1}{\rho(\boldsymbol{r}, t)} \int \mathrm{d}\boldsymbol{v} v_k^n P(\boldsymbol{r}, \boldsymbol{v}, t). \tag{6.1}$$

Here, the spatial particle density $\rho(\boldsymbol{r}, t)$ is equal to the zeroth moment and provides the normalization when integrating over all velocities

$$\rho(\boldsymbol{r}, t) = \int \mathrm{d}\boldsymbol{v} P(\boldsymbol{r}, \boldsymbol{v}, t). \tag{6.2}$$

Dynamical equations for these velocity moments can be expressed using the distribution $P(\boldsymbol{r}, \boldsymbol{v}, t)$, by multiplying Eq. (6.1) with the particle density and taking the time derivative

$$\frac{\partial}{\partial t} \left(\rho \langle v_k^n \rangle \right) = \int \mathrm{d}\boldsymbol{v} v_k^n \frac{\partial P}{\partial t}. \tag{6.3}$$

To obtain analytical expressions for the dynamics of these moments, working along the lines of [RE10; RSG12], the equation of motion in dimensionless variables is first considered

$$\frac{d\tilde{\boldsymbol{v}}_i}{d\tilde{t}} = \tilde{\Gamma}[\boldsymbol{f}_i - \hat{\boldsymbol{v}}_i(\hat{\boldsymbol{v}}_i \cdot \boldsymbol{f}_i)] - \tilde{\boldsymbol{v}}_i + \tilde{\boldsymbol{\xi}}_i. \tag{6.4}$$

The Fokker-Planck equation is a partial differential equation that describes the time evolution of P. With the equation of motion Eq. (6.4), it is given by [Ris84]

$$\frac{\partial P}{\partial \tilde{t}} = -\tilde{\boldsymbol{v}} \cdot \nabla_{\tilde{\boldsymbol{r}}} P - \nabla_{\tilde{\boldsymbol{v}}} \left[-\tilde{\boldsymbol{v}} P + \tilde{\Gamma} P(\boldsymbol{f}_i - \hat{\boldsymbol{v}}_i(\hat{\boldsymbol{v}}_i \cdot \boldsymbol{f}_i)) \right] + \tilde{D} \Delta_{\tilde{\boldsymbol{v}}} P, \tag{6.5}$$

where $P \equiv P(\tilde{\boldsymbol{r}}, \tilde{\boldsymbol{v}}, \tilde{t})$. D, the diffusion coefficient, equals $\frac{1}{2}$ in the dimensionless variables used here. Eq. (6.5) describes a non-linear Fokker-Planck equation. This non-linearity stems from the fact that the average direction of motion of the neighbours, $\boldsymbol{f}$, is itself dependent on the distribution $P(\tilde{\boldsymbol{r}}, \tilde{\boldsymbol{v}}, \tilde{t})$ through the following relation:

$$\boldsymbol{f}(\tilde{\boldsymbol{r}}, \tilde{t}) = \frac{1}{\int_{\Omega_{R_0}(\tilde{\boldsymbol{r}})} \rho(\tilde{\boldsymbol{r}}', \tilde{t}) \mathrm{d}\tilde{\boldsymbol{r}}'} \int_{\Omega_{R_0}(\tilde{\boldsymbol{r}})} \mathrm{d}\tilde{\boldsymbol{r}}' \int \mathrm{d}\tilde{\boldsymbol{v}}' \hat{\boldsymbol{v}}' P(\tilde{\boldsymbol{r}}', \tilde{\boldsymbol{v}}', \tilde{t}). \tag{6.6}$$

Here, the spatial integrals extend over the neighbourhood defined by radius R_0. In the following analysis all variables are considered to be dimensionless.

Working in 2D with $k = x, y$, Eq. (6.3) and Eq. (6.5) are combined to obtain the equation for the dynamics of the velocity moments:

$$\begin{aligned} \frac{\partial}{\partial t} \left(\rho \left\langle v_x^n \right\rangle \right) = \int \mathrm{d}\boldsymbol{v} v_x^n \Bigg[& -v_x \frac{\partial P}{\partial x} - v_y \frac{\partial P}{\partial y} + \frac{\partial}{\partial v_x} \left(P v_x \right) + \frac{\partial}{\partial v_y} \left(P v_y \right) \\ & - \Gamma \frac{\partial}{\partial v_x} \left(f_x P - \frac{v_x}{v_x^2 + v_y^2} (f_x v_x + f_y v_y) P \right) \\ & - \Gamma \frac{\partial}{\partial v_y} \left(f_y P - \frac{v_y}{v_x^2 + v_y^2} (f_x v_x + f_y v_y) P \right) \\ & + \frac{1}{2} \left(\frac{\partial^2 P}{\partial v_x^2} + \frac{\partial^2 P}{\partial v_y^2} \right) \Bigg]. \end{aligned} \tag{6.7}$$

In the limit of $v_k \to \pm\infty$, the distribution P becomes the probability to find a particle with infinite speed and is thus equal to zero. Eq. (6.7) can be partially integrated, eliminating all the terms containing derivatives with respect to v_y. This simplifies Eq. (6.7) to

$$\begin{aligned}\frac{\partial}{\partial t}\left(\rho\left\langle v_x^n\right\rangle\right) = &-\frac{\partial}{\partial x}\left(\rho\left\langle v_x^{n+1}\right\rangle\right) - \frac{\partial}{\partial y}\left(\rho\left\langle v_x^n v_y\right\rangle\right) \\ &- n\rho\left\langle v_x^n\right\rangle + n\rho\Gamma f_x\left\langle v_x^{n-1}\right\rangle - n\rho\Gamma f_x\left\langle\frac{v_x^{n+1}}{v_x^2+v_y^2}\right\rangle \\ &- n\rho\Gamma f_y\left\langle\frac{v_x^n v_y}{v_x^2+v_y^2}\right\rangle + \frac{1}{2}n(n-1)\rho\left\langle v_x^{n-2}\right\rangle.\end{aligned} \tag{6.8}$$

The n-th moment of the velocity distribution is dependent on higher-order moments, so that Eq. (6.8) describes a coupled set of differential equations. To obtain analytical expressions for these moments, the non-Gaussian distribution will have to be approximated by a limited amount of its moments. A closed set of equations for the velocity moments can only be achieved by making the approximation that the contribution of a certain cut-off moment can be neglected.

6.2 A Mean-Field Model

To obtain analytical expressions from the equations derived in the previous section, a mean-field model is constructed based on the framework set up in [RE10; RSG12]. In such a mean-field model, every particle interacts with an averaged velocity field instead of with its local neighbours. The velocity vector for a particle can be written as $\boldsymbol{v} = \boldsymbol{u} + \delta\boldsymbol{v}$, where $\boldsymbol{u}$ is the mean-field velocity and $\delta\boldsymbol{v}$ is a vector of deviations around this mean. The assumption is made that the deviations in different directions are independent so that

$$\left\langle \delta v_{k_1}^n \delta v_{k_2}^m \right\rangle = \left\langle \delta v_{k_1}^n \right\rangle \left\langle \delta v_{k_2}^m \right\rangle \text{ for } k_1 \neq k_2. \tag{6.9}$$

This implies that the covariance matrix in two dimensions for these deviations is given by

$$\begin{pmatrix} \left\langle \delta v_{k_1}^2 \right\rangle & \left\langle \delta v_{k_1} \delta v_{k_2} \right\rangle \\ \left\langle \delta v_{k_2} \delta v_{k_1} \right\rangle & \left\langle \delta v_{k_2}^2 \right\rangle \end{pmatrix} = \begin{pmatrix} T_{k_1} & 0 \\ 0 & T_{k_2} \end{pmatrix}. \tag{6.10}$$

T_{k_1} and T_{k_2} are commonly referred to as the "temperature" components along each direction as they are related to the second moment of the velocity distribution. Romanczuk and Schimansky-Geier have shown that in the case of active particles, it is a gair approximation to treat these deviations as symmetrical and thus considering $\langle v_x^a \rangle$ as zero for odd a [RSG12]. A first attempt of a mean-field model is made following this approach. As will

become clear, the asymmetry of the velocity distribution plays an important role in the mean-field phase transition and odd-power moments should be included in the calculation of the velocity moments, which will be discussed in section 6.4.

6.3 Symmetrical Velocity Distribution

In the case of a symmetrical velocity distribution, the following moments can easily be written down

$$\begin{aligned} \langle v_x \rangle &= u_x, \\ \left\langle v_x^2 \right\rangle &= u_x^2 + T_x, \\ \left\langle v_x^2 \right\rangle &= u_x^3 + 3u_x T_x. \end{aligned} \tag{6.11}$$

The mixed moments can be calculated in the same way

$$\begin{aligned} \langle v_x v_y \rangle &= u_x u_y, \\ \left\langle v_x^2 v_y \right\rangle &= u_x^2 u_y + T_x u_y. \end{aligned} \tag{6.12}$$

Combining these with Eq. (6.8) allows for the calculation of the dynamical equations for the velocity moments. For $n = 0$, this results in

$$\frac{\partial \rho}{\partial t} = -\nabla_{\boldsymbol{r}}(\rho \boldsymbol{u}), \tag{6.13}$$

which is a continuity equation. Doing the same for $n = 1$ and utilizing the continuity equation will only result in a closed expression when the following approximation is made, as done in [RSG12]

$$\begin{aligned} \left\langle \frac{v_x^n}{\sqrt{v_x^2 + v_y^2}} \right\rangle &\approx \frac{\langle v_x^n \rangle}{\left\langle \sqrt{v_x^2 + v_y^2} \right\rangle} \\ &\approx \frac{\langle v_x^n \rangle}{\sqrt{\left\langle v_x^2 + v_y^2 \right\rangle}} \\ &\approx \frac{\langle v_x^n \rangle}{\sqrt{u_x^2 + u_y^2 + T_x + T_y}} \equiv \frac{\langle v_x^n \rangle}{v_T}, \end{aligned} \tag{6.14}$$

which then results in

$$\frac{\partial u_x}{\partial t} + \boldsymbol{u} \cdot \nabla_{\boldsymbol{r}} u_x = -u_x + \Gamma f_x - \Gamma f_x \frac{u_x^2 + T_x}{v_T^2} - \Gamma f_y \frac{u_x u_y}{v_T^2} - \frac{\partial T_x}{\partial x} - \frac{T_x}{\rho}\frac{\partial \rho}{\partial x}. \tag{6.15}$$

Finally, for $n = 2$, combining the results for $n = 0$ and $n = 1$ with Eq. (6.8) leads to

$$\frac{1}{2}\left(\frac{\partial T_x}{\partial t} + \boldsymbol{u} \cdot \nabla_{\boldsymbol{r}} T_x\right) = \left(-1 - 2\Gamma f_x \frac{u_x}{v_T^2} - \Gamma f_y \frac{u_y}{v_T^2}\right) T_x + \frac{1}{2} - T_x \frac{\partial u_x}{\partial x}. \tag{6.16}$$

In the previous equations, the moments of the velocity along the x-axis were considered. Interchanging $x \leftrightarrow y$ in these equations leads to the dynamical equations of the moments along the y-axis.

In the case of a globally-coupled or high-density system, it is a good approximation to treat the system as spatially homogeneous. With the assumption of spatial homogeneity, the average direction of motion $f_x = u_x/v_T$, so that these last equations simplify to

$$\frac{\partial u_x}{\partial t} = -u_x + \Gamma \frac{u_x}{v_T} - \Gamma \frac{u_x(u_x^2 + T_x)}{v_T^3} - \Gamma \frac{u_x u_y^2}{v_T^3}, \tag{6.17}$$

and

$$\frac{1}{2}\frac{\partial T_x}{\partial t} = \left(-1 - 2\frac{u_x^2}{v_T^3} - \Gamma \frac{u_y^2}{v_T^3}\right) T_x + \frac{1}{2}. \tag{6.18}$$

Naturally, this does not describe a low-density system well: it was shown earlier that in these systems clustering occurs between collectively moving particles, so that spatial homogeneity is no longer a valid assumption.

A change of basis can be made from the (x, y) frame to one where the axes are parallel and perpendicular to the direction of the mean-field velocity, so that $u = u_\parallel$ and $u_\perp = 0$. The dynamics for the moments then simplify to

$$\begin{aligned}
\frac{\partial u_\parallel}{\partial t} &= -u_\parallel + \Gamma \frac{u_\parallel}{v_T} - \Gamma \frac{u_\parallel (u_\parallel^2 + T_\parallel)}{v_T^3}, \\
\frac{1}{2}\frac{\partial T_\parallel}{\partial t} &= \left(-1 - 2\Gamma \frac{u_\parallel^2}{v_T^3} \right) T_\parallel + \frac{1}{2}, \\
\frac{1}{2}\frac{\partial T_\perp}{\partial t} &= \left(-1 - \Gamma \frac{u_\parallel^2}{v_T^3} \right) T_\perp + \frac{1}{2},
\end{aligned} \tag{6.19}$$

where now

$$v_T = \sqrt{u_\parallel^2 + T_\parallel + T_\perp}. \tag{6.20}$$

Results

The Python software package PyDSTool was used for the integration of the differential equations [CR07], and the software package XPPAUT was used for a bifurcation analysis [Erm02]. Fig. 6.1 shows the solution for $u_\parallel$ in function of the coupling factor for the mean-field model. Initial conditions are either the ordered phase with $u_\parallel(0) = 1$, or the disordered phase with $u_\parallel(0) = 10^{-4}$. Note that the totally disordered phase with $u_\parallel(0) = 0$ is an unstable fixed point at $\Gamma \geq 2.0$ in the mean-field model. Contrary to what simulations with a globally-coupled Vicsek model have shown, hysteresis is present in the system. When starting from the disordered phase, the transition to the ordered phase occurs at $\Gamma \approx 2.0$. However, when starting from the ordered phase, the transition to disorder occurs for $\Gamma \approx 1.9$. As will be shown in the following section, this can be linked to the approximation of a symmetrical velocity distribution.

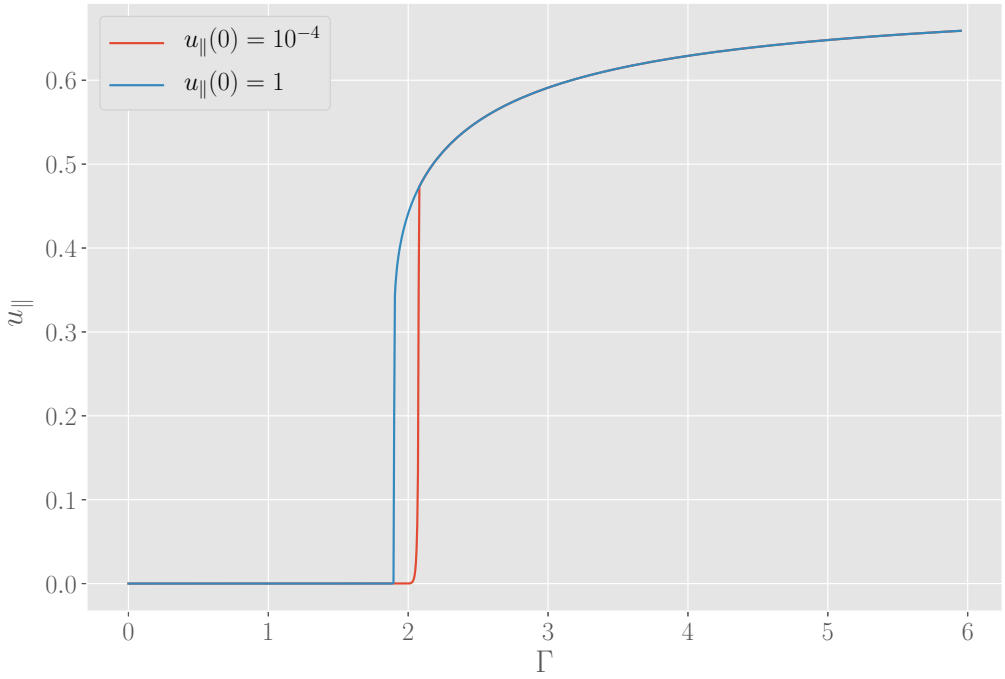

Fig. 6.1.: The value of $u_\parallel$ in function of the coupling factor for the mean-field model with a symmetrical velocity distribution. The solution starting from a disordered phase (red line) is different from the solution starting in the ordered phase (blue line).

6.4 Asymmetrical Velocity Distribution

When considering an asymmetrical velocity distribution, the moments for $n > 2$ become

$$\begin{aligned} \left\langle v_x^3 \right\rangle &= u_x^3 + 3u_x T_x + S_x, \\ \left\langle v_x^4 \right\rangle &= u_x^4 + 6u_x^2 T_x + 4u_x S_x + K_x, \end{aligned} \tag{6.21}$$

and so on for higher moments. Here, $S_x = \langle \delta v_x^3 \rangle$ and $K_x = \langle \delta v_x^4 \rangle$ as they are related to the skewness and kurtosis of the velocity distribution, respectively. To calculate higher-order moments that will appear for an asymmetrical velocity distribution, calculations are made in the $(\parallel, \perp)$-frame and under the

condition of a spatially homogeneous system. The first five moments in this reference frame are given by

$$\begin{aligned}
\frac{\partial u_\parallel}{\partial t} &= -u_\parallel + \Gamma\frac{u_\parallel}{v_T} - \Gamma\frac{u_\parallel(u_\parallel^2 + T_\parallel)}{v_T^3},\\
\frac{\partial T_\parallel}{\partial t} &= -2T_\parallel - 4\frac{\Gamma u_\parallel^2 T_\parallel}{v_T^3} - 2\frac{\Gamma u_\parallel S_\parallel}{v_T^3} + 1,\\
\frac{\partial S_\parallel}{\partial t} &= -3S_\parallel - 6\frac{\Gamma u_\parallel^2 S_\parallel}{v_T^3} - 3\frac{\Gamma u_\parallel K_\parallel}{v_T^3} + 3\frac{\Gamma u_\parallel T_\parallel^2}{v_T^3},\\
\frac{\partial K_\parallel}{\partial t} &= -4K_\parallel - 8\frac{\Gamma u_\parallel^2 K_\parallel}{v_T^3} - 4\frac{\Gamma u_\parallel F_\parallel}{v_T^3} + 6T_\parallel + 4\frac{\Gamma u_\parallel T_\parallel S_\parallel}{v_T^3},\\
\frac{\partial F_\parallel}{\partial t} &= -5F_\parallel - 10\frac{\Gamma u_\parallel^2 F_\parallel}{v_T^3} - 5\frac{\Gamma u_\parallel \sigma_\parallel}{v_T^3} + 10S_\parallel + 5\frac{\Gamma u_\parallel T_\parallel K_\parallel}{v_T^3}.
\end{aligned} \tag{6.22}$$

Here, $F = \langle \delta v^5 \rangle$ and $\sigma = \langle \delta v^6 \rangle$. To obtain closure for this series of moments, the approximation is made that $\sigma - S^2 = 0$. This means that the variance of the skewness of the velocity distribution is set to zero. By doing this, the dynamical equation for the fifth moment in Eq. (6.22) simplifies to

$$\frac{\partial F_\parallel}{\partial t} = -5F_\parallel - 10\frac{\Gamma u_\parallel^2 F_\parallel}{v_T^3} + 10S_\parallel + 5\frac{\Gamma u_\parallel (T_\parallel K_\parallel - S_\parallel^2)}{v_T^3}. \tag{6.23}$$

The dynamical equations describing the perpendicular moments of the velocity distribution are given by

$$\begin{aligned}
\frac{\partial T_\perp}{\partial t} &= -2T_\perp - 2\frac{\Gamma u_\parallel^2 T_\perp}{v_T^3} + 1,\\
\frac{\partial S_\perp}{\partial t} &= -3T_\perp - 3\frac{\Gamma u_\parallel^2 S_\perp}{v_T^3},\\
\frac{\partial K_\perp}{\partial t} &= -4T_\perp - 4\frac{\Gamma u_\parallel^2 K_\perp}{v_T^3} + 6T_\perp,\\
\frac{\partial F_\perp}{\partial t} &= -5T_\perp - 5\frac{\Gamma u_\parallel^2 F_\perp}{v_T^3} + 10S_\perp.
\end{aligned} \tag{6.24}$$

Results

In Fig. 6.2, the results from the mean-field model for $u_\parallel$ and the two temperature components are compared to numerical results obtained from a globally-coupled system with $N = 90000$. A bifurcation analysis using the PyCont [RH10] package indicates the existence of a branching point at

$\Gamma = 2.0$, which is in agreement with the value of $\Gamma = 1.991$ obtained for a globally-coupled system [Sev+14]. Hysteresis is no longer present in the system when working with an asymmetrical velocity distribution. Several factors can explain the deviations between these numerical results and the mean-field model. First, the approximation in Eq. (6.14) will play a part in this. Furthermore, as collective motion sets in, the velocity distribution is non-Gaussian, but is here described by only its first five moments. Lastly, the mean-field model ignores the fluctuations on the skewness of the velocity distribution. As ultimately all moments are coupled, this will have an effect on the solution for the mean-field velocity and temperature shown in Fig. 6.2. The seemingly better fit for models involving active Brownian particles (e.g. [RE10]) can be explained by the fact that the approximation in Eq. (6.14) has to be made less often. The active nature of the particles in such a model also invokes the additional criterion that the mean-field speed $u_{\parallel}$ has to converge to the self-propelled speed v_0 in the limit of zero noise.

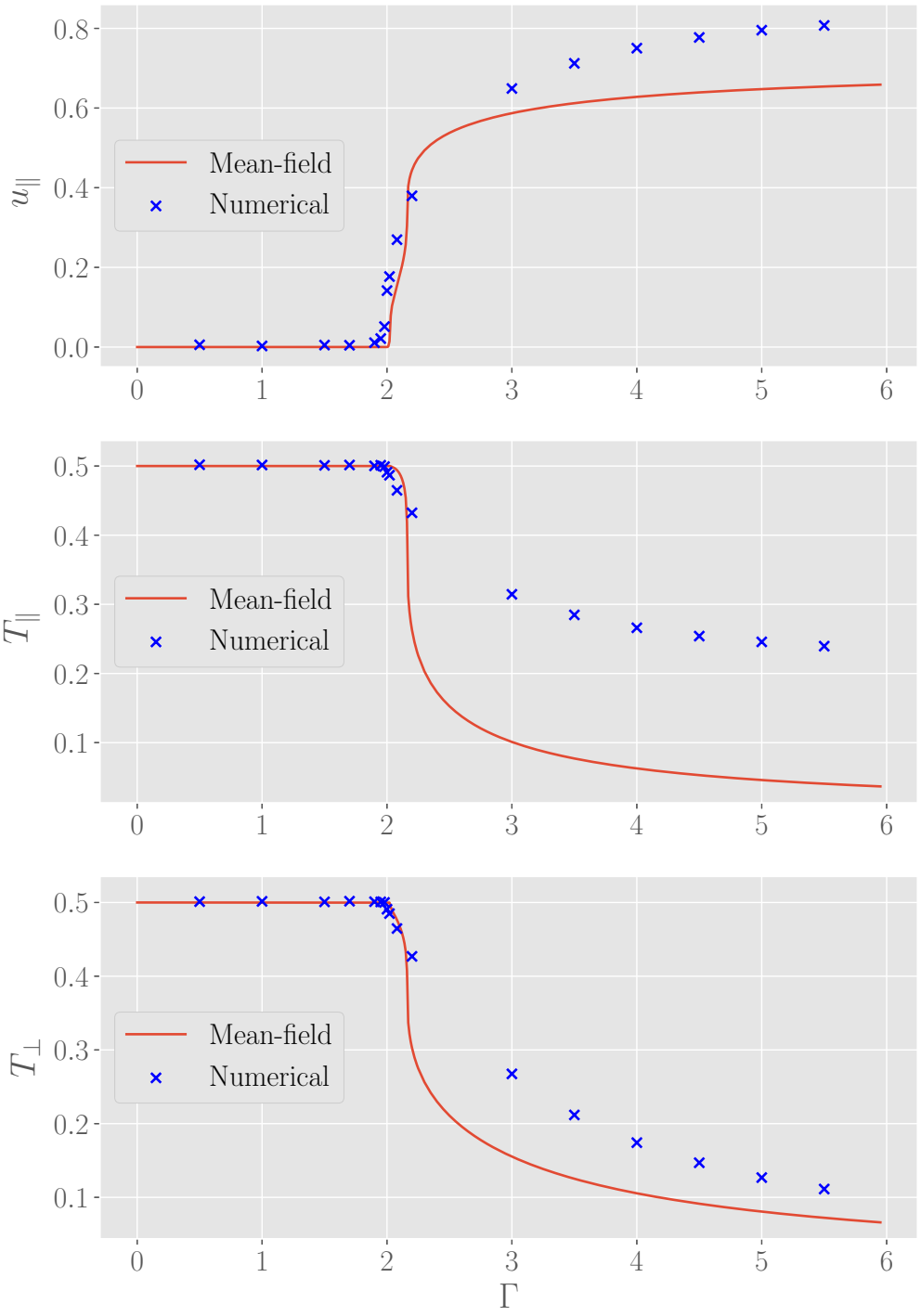

Fig. 6.2.: Comparison between the first two moments of the velocity distribution for the mean-field model and a numerically simulated globally-coupled system with $N = 90000$.

7 Conclusion and Outlook

Collective motion is a form of collective behaviour that can arise in complex systems. Observations indicate that the patterns of collective motion can be categorized in only a few distinct classes. This could indicate universal underlying mechanisms. In this thesis, a minimal model was used to investigate the features required to develop collective motion.

The Vicsek model – introduced in chapter 2 – is among the best-known of these minimal models. It describes self-propelling Brownian particles that align their direction of motion to that of their neighbours under the influence of a short-range force. This model shows a discontinuous phase transition and the transition to collective motion occurs when the social force becomes strong enough to overcome the effect of noise.

In order to determine whether collective motion needs a self-propelling nature of particles, Dossetti and Sevilla developed a model that describes passive Brownian particles rather than self-propelling ones [DS15]. This model was the focus of the remainder of this thesis.

In chapter 3, the results of Dossetti and Sevilla were verified. In addition, particle diffusion was studied for this model. If collective motion was present in the system, particle diffusion turned out to be anisotropic with regard to the directions parallel and perpendicular to the mean direction of motion. This is in contrast with the original Vicsek model, in which the anisotropy is reversed. The mechanism behind this difference remains unclear.

In chapter 4, the spatial correlations between particles were studied. Particles were found to be spatially correlated at all times – over small ranges in the absence of collective motion and large distances when it was present. As with the original Vicsek model, phase separation occurred for coupling factors right above the transition point. For a 2D system with periodic boundary conditions, this phase separation took on the form of dense bands travelling collectively through a region of disorderly moving particles. These bands also appeared in the original Vicsek model. In the model of Dossetti and Sevilla, they were found to be wider and less dense. Additionally, particles in the

disorganized regions formed small clusters. The size of these clusters was proven to follow a power-law with a cut-off size dependent on the number of particles. A finite-size scaling analysis was performed for the cluster-size distribution, resulting in a power-law exponent of less than 2.

In chapter 5, the entropy production was examined. The entropy production was shown to be a combination of three things: the change in system entropy, the entropy production linked to the heat dissipation to the reservoir and an unconventional entropy production, linked to the odd-parity variables included in the force. When averaged in the steady state, only the unconventional entropy production was non-zero. The entropy production was measured for a globally-coupled and a short-range version of the model by Dossetti and Sevilla. For the globally-coupled model, the entropy production was confirmed to be sub-extensive in the disordered phase. It became extensive at the onset of collective motion. This could be explained by considering that in the disordered phase all particle trajectories are equally likely so that detailed balance still holds true on a macroscopic scale. When a short-range force was implemented instead, the nature of the entropy production changed drastically: extensive in the disordered phase and depending on the system size at the transition point. While the latter effect can be explained by size effects, no intuitive explanation was found for the former. Its cause may lie in the spatial correlations inherent to the short-range model, but results on this remain inconclusive.

Finally, a mean-field version was developed in chapter 6 for the model by Dossetti and Sevilla. This version was inspired by the work of Romanczuk and Schimansky-Geier and assumes spatial homogeneity [RSG12]. Compared to numerical results of a globally-coupled model, the mean-field model made good predictions for coupling factors of the disordered phase and around the transition point. For higher values of the coupling factor, the mean-field model showed larger deviations when compared to the numerical results. These can be attributed to the approximations made in the mean-field model, as it e.g. neglects fluctuations on the skewness of the velocity distribution.

These results conclude the work done for this thesis on the Vicsek model for passive particles. Self-propulsion was confirmed to be unnecessary for the development of collective motion. Experiments on passive particles such as some shaken rods could test this claim further.

For systems larger than those studied in the analysis of the cluster size distributions, the original Vicsek model displays several evenly spaced bands rather than the single band found in all performed simulations. Further studies are required to observe if the bands also split up for the model used here and whether this has any effect on the cluster size distribution.

An investigation of the entropy production in the system produced results that are difficult to explain. A further study of the entropy production could deepen our understanding of the effect of spatial inhomogeneities on the entropy production. Such a study has recently been undertaken for field theories of active matter [Nar+17].

The mean-field adaptation of the Vicsek model properly described homogeneous systems, but no existing model takes spatial fluctuations into account. To account for spatial fluctuations in a mean-field model, perhaps an extension similar to the Bethe approximation in the Ising model could be created. The topological version of the Vicsek model, in which the number of neighbours is fixed, may be especially suitable for this.

While the last decade brought much progress in the understanding of the Vicsek model, the temporal mechanisms underlying the emergence of long-range order remain unclear. The time-evolution could be quantified by using temporal network theory. This has proven useful to understand the large-scale features in a connected system. Applying it would lead to an informative picture of how information spreads through the system. A recent development for analysing the structural differences of these time-evolving networks is the change-point detection technique. The onset of collective motion alters the network topology and by using a Bayesian hypothesis test, this technique could allow for the identification of the times at which large-scale pattern changes occur.

Nederlandse Samenvatting

Collectieve beweging is een alomtegenwoordig fenomeen in onze wereld. Observaties tonen aan dat de patronen van collectieve beweging kunnen onderverdeeld worden in een beperkt aantal klassen. Het is dus interessant voor fysici om het onderliggende mechanisme dat dit universeel gedrag veroorzaakt te onderzoeken. Hiervoor wordt gebruik gemaakt van een minimaal model dat met zo weinig mogelijk eigenschappen collectieve beweging kan veroorzaken.

Hoofdstuk 1 begint met een introductie tot complexiteit, fasetransities en collectieve beweging. In hoofdstuk 2 wordt het Vicsek model geïntroduceerd: een populair model voor het beschrijven van collectieve beweging. Dit model beschrijft actieve Browniaanse deeltjes die onderhevig zijn aan kortedrachtinteracties. Deze interacties zorgen ervoor dat de bewegingsrichting van deeltjes gealigneerd wordt met die van hun buren. Eens deze kracht sterk genoeg is om de ruis inherent aan dit model te overwinnen, ontstaat collectieve beweging.

Hoofdstuk 3 beschrijft de verificatie van een model ontwikkeld door Sevilla et al., waarbij wordt nagegaan of de deeltjes wel degelijk actief moeten zijn voor de ontwikkeling van collectieve beweging. De spatiale correlaties die optreden in dit model worden verder onderzocht in hoofdstuk 4. Hier wordt onder meer de verdeling van de clustergroottes in een van de fasen van dit model bestudeerd.

Hoofdstuk 5 bestudeert de entropieproductie in het model van Sevilla et al., zowel voor kortedrachtinteracties als voor globale interacties. De entropieproductie toont grote verschillen voor beide soorten interacties, hetgeen verder

onderzocht moet worden om tot een intuïtieve verklaring te komen. Tenslotte wordt in hoofdstuk 6 een mean-fieldversie bestudeerd van het model van Sevilla et al. In dit model worden alle interacties uitgemiddeld, wat voor een simpelere beschrijving zorgt aangezien het veeldeeltjesprobleem wordt gereduceerd tot een ééndeeltjesprobleem.

Numerical Considerations

A

A.1 Integrating the Equation of Motion

To study the time evolution of the system, the equation of motion Eq. (3.11) is integrated using a modified velocity-Verlet algorithm as introduced by Groot and Warren, where it was applied for dissipative particle dynamics [GW97]. This algorithm is given by

$$\begin{aligned}
\boldsymbol{r}_i(t+\Delta t) &= \boldsymbol{r}_i(t) + \Delta t \boldsymbol{v}_i(t) + \frac{1}{2}(\Delta t)^2 \boldsymbol{F}_i(t), \\
\overline{\boldsymbol{v}}_i(t+\Delta t) &= \boldsymbol{v}_i(t) + \lambda \Delta t \boldsymbol{F}_i(t), \\
\boldsymbol{F}_i(t+\Delta t) &= \boldsymbol{F}_i\left(\boldsymbol{r}(t+\Delta t), \overline{\boldsymbol{v}}(t+\Delta t)\right), \\
\boldsymbol{v}_i(t+\Delta t) &= \boldsymbol{v}_i(t) + \frac{1}{2}\Delta t \left(\boldsymbol{F}_i(t) + \boldsymbol{F}_i(t+\Delta t)\right),
\end{aligned} \tag{A.1}$$

where $\boldsymbol{F}$ is the sum of the frictional, velocity-aligning and stochastic force. As in [GW97], the empirical factor λ was set to be $\lambda = 1/2$, as integration with this factor and the integration scheme (A.1) corresponded very well with the results obtained with a simple Euler-algorithm.

For the time step Δt appearing in this scheme, generally the choice $\Delta t = 0.01$ (in dimensionless variables) was made. Integration with this time step reproduced the features of Brownian motion if no velocity-aligning force was included, while the important criterion $v_i \Delta t \ll R_0$ is also valid. This last criterion means that a particle does not move through another particle's interaction range in-between two time steps. However, for low-density systems ($\tilde{\rho} \leq 2$), the increased fluctuations have as effect that reaching the steady state is a much slower process. For these systems, $\Delta t = 0.02$ was used.

A.2 Force Calculation

For the calculation of the velocity-aligning force, a linked-cell method inspired by molecular dynamics is used. With this method, the system is divided in square boxes with a length of R_0. This implies that, for a particle in a certain box, all its neighbours will be either in the box itself or in one of the neighbouring boxes (8 in 2D, 26 in 3D). Here, periodic boundary conditions are applied. This method reduces the scaling of the force calculations from $O(N^2)$ to $O(NN_c)$, where N_c is the average amount of particles for every cell (which does not change on increasing the system size or number of particles at a fixed particle density). Naturally, for every box, only half of the neighbouring boxes has to be considered. Fig. A.1 and the pseudo-code below illustrate this method.

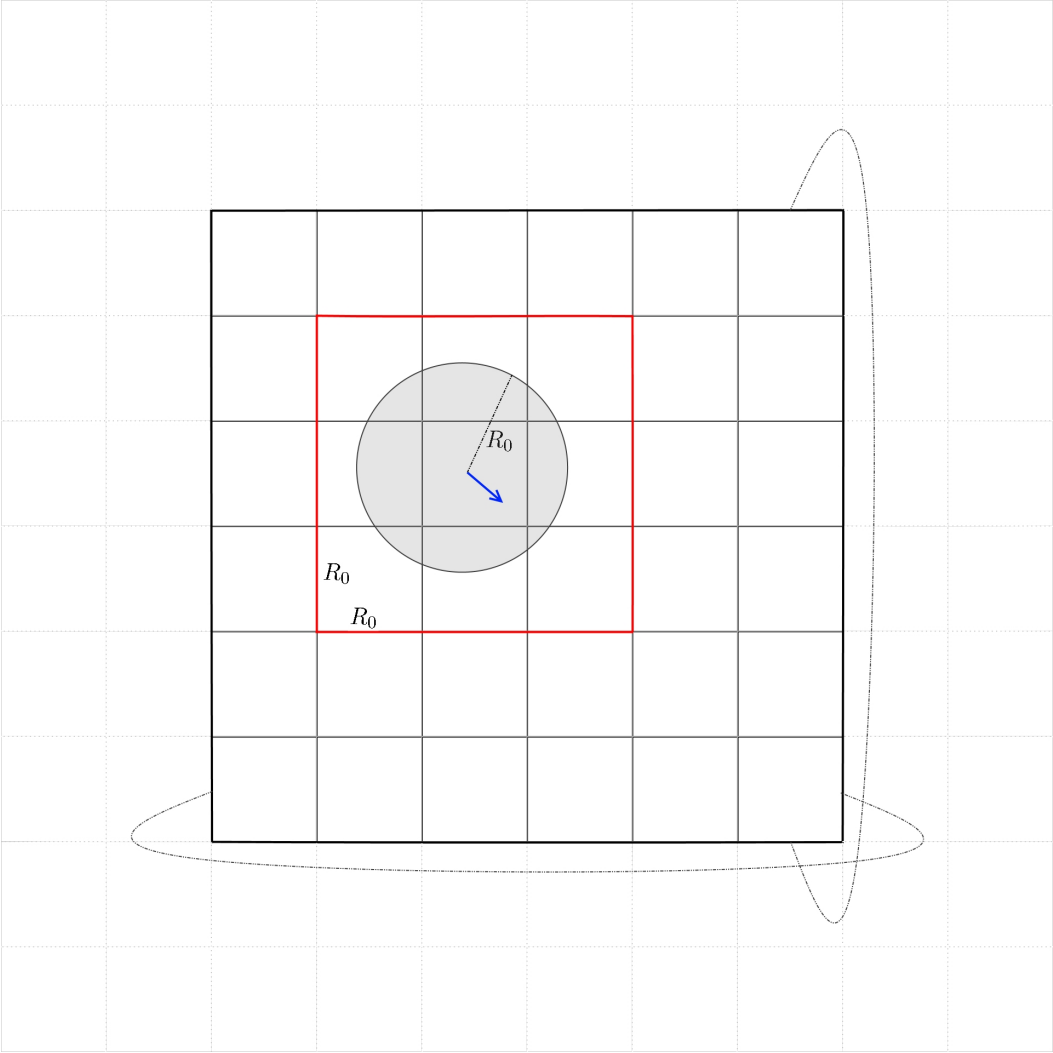

Fig. A.1.: Illustration of the linked-cell method. The neighbours of the central particle (blue) are all contained in the red square.

Algorithm 1 Initializing Link and Header

NoB = systemSize $\leftarrow$ Number of boxes
Header[NoB][NoB] = -1
Link[N] = -1

for $i = 1 \dots N$ **do**
    xIndex = **Floor**(x_i)
    yIndex = **Floor**(y_i)
    Link[i] = Header[xIndex][yIndex]
    Header[xIndex][yIndex] = i

Now, 'Header' contains the highest particle index for every box (or -1 if there are no particles in the box) and 'Link[i]' is another particle in the same box as i, but with a lower index (if there is no such particle, it is equal to -1). With these two structures, the neighbours of every particle can be found quickly and the force calculation is done with the following algorithm:

Algorithm 2 Force Calculation

averageDirection[N] = 0
Neighbourcount[N] = 0
for all boxes **do**
    Using Header, Link: determine particles in central box
    for half of neighbouring boxes **do**
        Using Header, Link: determine particles in neighbouring boxes
    for particles i in central box **do**
        if any particle j from central or neighbouring box in range **then**
            add direction of particle j to averageDirection[i] and vice-versa
            Neighbourcount[i] += 1
            Neighbourcount[j] += 1
for $i = 1 \dots N$ **do**
    calculate force on particle i using averageDirection, Neighbourcount

For the stochastic force appearing in (6.4), care has to be taken with the Dirac-delta function appearing here. To circumvent the singular nature of this function, it is deemed constant during one time step, so that

$$\delta(t - t') = \begin{cases} \frac{1}{\Delta t} & \text{if } t' \in [t, t + \Delta t], \\ 0 & \text{otherwise.} \end{cases} \tag{A.2}$$

A first simulation attempt with C++'s pseudo-random number generator showed periodic peaks in the autocorrelation of the order parameter over long time scales. These appeared because of the insufficient period of the PRNG. Hence, the random numbers used throughout the simulations in this thesis were generated with a Mersenne-Twister pseudo-random number generator. Normally distributed random numbers were then generated using C++'s Box-Muller transform.

A.3 Autocorrelation with FFT

As in section 3.3.4, we often wish to compute a quantity of the type

$$\chi_i(t) = \langle x_i(t_0) x_i(t_0 + t) \rangle_{t_0} , \tag{A.3}$$

where the average is over the arbitrary reference times. If n samples are available, the computation of this autocorrelation is of the order of n^2, which can become very costly for large samples and certainly so if we also wish to average over all particles in the system. To speed up this process, one can make use of the Fast Fourier Transform (FFT) algorithm, so that the calculation of the autocorrelation function scales as $n \log n$ [NB99]. The Fourier transform of (A.3) is given by

$$\begin{aligned} \tilde{\chi}(\omega) &= \int \mathrm{d}t \; \mathrm{e}^{i\omega t} \int \mathrm{d}t' \; x(t') x(t' + t) \\ &= \int \mathrm{d}t \; \int \mathrm{d}t' \; \mathrm{e}^{-i\omega t'} x(t') \mathrm{e}^{i\omega(t'+t)} x(t' + t) \\ &= \tilde{x}(\omega) \tilde{x}(-\omega) = |\tilde{x}(\omega)|^2, \end{aligned} \tag{A.4}$$

where $\tilde{x}(\omega)$ is the Fourier transform of $x(t)$. Hence, the Fourier transform of $x(t)$ is calculated using the FFT algorithm and after applying the inverse FFT on $|\tilde{x}(\omega)|^2$, the autocorrelation function of $x(t)$ is obtained.

Power-law Distributions

B

A variable x is said to follow a power-law if its distribution is of the form

$$p(x) \propto x^{-\alpha}, \tag{B.1}$$

where α is commonly referred to as the exponent of the power-law [New05]. A power-law distribution comes in two forms, depending on whether x is a continuous or discrete variable. As the cluster sizes in section 4.3 can only take on integer values, this appendix is concerned with power-law distribution for the latter. The probability distribution is in this case given by

$$p_x = Cx^{-\alpha}, \tag{B.2}$$

where C is a normalization constant. Note that this distribution diverges for $x = 0$, so that there must be a lower-bound, x_{min} on this distribution [Cla+09]. The normalization constant can be found by requiring that all the probabilities sum to one:

$$1 = C \sum_{x=x_{min}}^{\infty} x^{-\alpha} = C\zeta(\alpha, x_{min}), \tag{B.3}$$

where $\zeta(\alpha, x_{min})$ is the generalized Riemann ζ-function, so that

$$p_x = \frac{x^{-\alpha}}{\zeta(\alpha, x_{min})}. \tag{B.4}$$

Power-law distributions are an example of a "heavy-tailed" distribution: events that would be considered outliers for a Gaussian distribution occur with a relatively large probability for a power-law distribution. They are also said to be "scale-free", meaning the distribution has the same appearance when a change of scale is made [Als+14; New05]. This can be easily verified, as when x is scaled by a certain factor b, the distribution in Eq. (B.4) becomes

$$\begin{aligned} p_{bx} &= \frac{b^{-\alpha}x^{-\alpha}}{\zeta(\alpha, x_{min})} \\ &= b^{-\alpha}p_x, \end{aligned} \tag{B.5}$$

so that upon a change of scale, the distribution gets multiplied by a constant, but its shape remains unchanged. The power-law distribution is the only distribution with this feature [New05].

The k-th moment of a power-law distribution can be calculated as

$$\left\langle x^k \right\rangle = \frac{1}{\zeta(\alpha, x_{min})} \sum_{x=x_{min}}^{\infty} x^{k-\alpha}, \tag{B.6}$$

so that it is divergent if $\alpha \leq k$.

Bibliography

[Ach99] Muktish Acharyya. “Nonequilibrium phase transition in the kinetic Ising model: Existence of a tricritical point and stochastic resonance”. In: *Physical Review E* 59.1 (1999), p. 218 (cit. on p. 25).

[Ald+07] Maximino Aldana, Victor Dossetti, Christian Huepe, VM Kenkre, and Hernán Larralde. “Phase transitions in systems of self-propelled agents and related network models”. In: *Physical Review Letters* 98.9 (2007), p. 095702 (cit. on p. 11).

[Ald+09] M Aldana, H Larralde, and B Vázquez. “On the emergence of collective order in swarming systems: a recent debate”. In: *International Journal of Modern Physics B* 23.18 (2009), pp. 3661–3685 (cit. on p. 14).

[Als+14] Jeff Alstott, Ed Bullmore, and Dietmar Plenz. “powerlaw: a Python package for analysis of heavy-tailed distributions”. In: *PLOS ONE* 9.1 (2014), e85777 (cit. on pp. 49, 87).

[BA08] Gabriel Baglietto and Ezequiel V Albano. “Finite-size scaling analysis and dynamic study of the critical behavior of a model for the collective displacement of self-driven individuals”. In: *Physical Review E* 78.2 (2008), p. 021125 (cit. on p. 11).

[BA09a] Gabriel Baglietto and Ezequiel V Albano. “Computer simulations of the collective displacement of self-propelled agents”. In: *Computer Physics Communications* 180.4 (2009), pp. 527–531 (cit. on p. 11).

[BA09b] Gabriel Baglietto and Ezequiel V Albano. “Nature of the order-disorder transition in the Vicsek model for the collective motion of self-propelled particles”. In: *Physical Review E* 80.5 (2009), p. 050103 (cit. on p. 11).

[Bal+08] Michele Ballerini, Nicola Cabibbo, Raphael Candelier, et al. “Interaction ruling animal collective behavior depends on topological rather than metric distance: Evidence from a field study”. In: *Proceedings of the National Academy of Sciences* 105.4 (2008), pp. 1232–1237 (cit. on p. 18).

[Ber+09] Eric Bertin, Michel Droz, and Guillaume Grégoire. “Hydrodynamic equations for self-propelled particles: microscopic derivation and stability analysis”. In: *Journal of Physics A: Mathematical and Theoretical* 42.44 (2009), p. 445001 (cit. on p. 12).

[BG90] Jean-Philippe Bouchaud and Antoine Georges. “Anomalous diffusion in disordered media: statistical mechanisms, models and physical applications”. In: *Physics Reports* 195.4-5 (1990), pp. 127–293 (cit. on p. 37).

[Bin81] Kurt Binder. “Critical properties from Monte Carlo coarse graining and renormalization”. In: *Physical Review Letters* 47.9 (1981), p. 693 (cit. on p. 24).

[Bla+03] Daniel L Blair, T Neicu, and Arshad Kudrolli. “Vortices in vibrated granular rods”. In: *Physical Review E* 67.3 (2003), p. 031303 (cit. on p. 2).

[BY02] Yaneer Bar-Yam. “General features of complex systems”. In: *Encyclopedia of Life Support Systems (EOLSS), UNESCO, EOLSS Publishers, Oxford, UK* (2002) (cit. on p. 1).

[Cha+07] Hugues Chaté, Francesco Ginelli, and Guillaume Grégoire. “Comment on “phase transitions in systems of self-propelled agents and related network models””. In: *Physical Review Letters* 99.22 (2007), p. 229601 (cit. on pp. 10, 12).

[Cha+08a] Hugues Chaté, Francesco Ginelli, Guillaume Grégoire, and Franck Raynaud. “Collective motion of self-propelled particles interacting without cohesion”. In: *Physical Review E* 77.4 (2008), p. 046113 (cit. on pp. 11–13, 30).

[Cha+08b] Hugues Chaté, Francesco Ginelli, Guillaume Grégoire, Fernando Peruani, and Franck Raynaud. “Modeling collective motion: variations on the Vicsek model”. In: *The European Physical Journal B-Condensed Matter and Complex Systems* 64.3 (2008), pp. 451–456 (cit. on pp. 14, 19).

[Cha01] Serena Chan. “Complex adaptive systems”. In: *ESD. 83 Research Seminar in Engineering Systems*. Vol. 31. 2001 (cit. on p. 1).

[Cla+09] Aaron Clauset, Cosma Rohilla Shalizi, and Mark EJ Newman. “Power-law distributions in empirical data”. In: *SIAM Review* 51.4 (2009), pp. 661–703 (cit. on p. 87).

[CM05] Kim Christensen and Nicholas R Moloney. *Complexity and criticality*. Vol. 1. Imperial College Press, 2005 (cit. on p. 50).

[Cou+05] Iain D Couzin, Jens Krause, Nigel R Franks, and Simon A Levin. “Effective leadership and decision-making in animal groups on the move”. In: *Nature* 433.7025 (2005), pp. 513–516 (cit. on p. 19).

[CR07] LaMar MD Guckenheimer JM Clewley RH Sherwood WE. *PyDSTool, a software environment for dynamical systems modeling*. 2007. URL: `http://pydstool.sourceforge.net` (cit. on p. 72).

[CV00] András Czirók and Tamás Vicsek. "Collective behavior of interacting self-propelled particles". In: *Physica A: Statistical Mechanics and its Applications* 281.1 (2000), pp. 17–29 (cit. on p. 9).

[Czi+96] András Czirók, Eshel Ben-Jacob, Inon Cohen, and Tamás Vicsek. "Formation of complex bacterial colonies via self-generated vortices". In: *Physical Review E* 54.2 (1996), p. 1791 (cit. on p. 15).

[DM+98] M De Menech, AL Stella, and C Tebaldi. "Rare events and breakdown of simple scaling in the Abelian sandpile model". In: *Physical Review E* 58.3 (1998), R2677 (cit. on p. 50).

[DS15] Victor Dossetti and Francisco J Sevilla. "Emergence of collective motion in a model of interacting Brownian particles". In: *Physical Review Letters* 115.5 (2015), p. 058301 (cit. on pp. 22, 26, 30, 41, 53, 77, 78).

[Erm02] Bard Ermentrout. *Simulating, analyzing, and animating dynamical systems: a guide to XPPAUT for researchers and students*. SIAM, 2002 (cit. on p. 72).

[GC04] Guillaume Grégoire and Hugues Chaté. "Onset of collective and cohesive motion". In: *Physical Review Letters* 92.2 (2004), p. 025702 (cit. on pp. 10, 11, 15, 17).

[GC10] Francesco Ginelli and Hugues Chaté. "Relevance of metric-free interactions in flocking phenomena". In: *Physical Review Letters* 105.16 (2010), p. 168103 (cit. on p. 18).

[Gin16] Francesco Ginelli. "The Physics of the Vicsek model". In: *The European Physical Journal Special Topics* 225.11-12 (2016), pp. 2099–2117 (cit. on pp. 4, 8–10, 15, 29, 30).

[Gro+12] Robert Grossmann, Lutz Schimansky-Geier, and Pawel Romanczuk. "Active Brownian particles with velocity-alignment and active fluctuations". In: *New Journal of Physics* 14.7 (2012), p. 073033 (cit. on p. 15).

[Gré+03] Guillaume Grégoire, Hugues Chaté, and Yuhai Tu. "Moving and staying together without a leader". In: *Physica D: Nonlinear Phenomena* 181.3 (2003), pp. 157–170 (cit. on pp. 4, 11, 15, 17, 18).

[GT10] Harvey Gould and Jan Tobochnik. *Statistical and thermal physics: with computer applications*. Princeton University Press, 2010 (cit. on p. 47).

[GW97] Robert D Groot and Patrick B Warren. "Dissipative particle dynamics: Bridging the gap between atomistic and mesoscopic simulation". In: *The Journal of Chemical Physics* 107.11 (1997), pp. 4423–4435 (cit. on p. 83).

[HA04] Cristián Huepe and Maximino Aldana. “Intermittency and clustering in a system of self-driven particles”. In: *Physical Review Letters* 92.16 (2004), p. 168701 (cit. on p. 48).

[Ibe+09] Michael Ibele, Thomas E Mallouk, and Ayusman Sen. “Schooling Behavior of Light-Powered Autonomous Micromotors in Water”. In: *Angewandte Chemie International Edition* 48.18 (2009), pp. 3308–3312 (cit. on p. 2).

[Jen03] Henrik Jeldtoft Jensen. “Lecture notes on Kosterlitz-Thouless transition in the XY model”. In: *Imperial College Lectures* (2003) (cit. on p. 9).

[Kur98] Jorge Kurchan. “Fluctuation theorem for stochastic dynamics”. In: *Journal of Physics A: Mathematical and General* 31.16 (1998), p. 3719 (cit. on p. 57).

[Kwo+16] Chulan Kwon, Joonhyun Yeo, Hyun Keun Lee, and Hyunggyu Park. “Unconventional entropy production in the presence of momentum-dependent forces”. In: *Journal of the Korean Physical Society* 68.5 (2016), pp. 633–638 (cit. on pp. 58, 59).

[MW66] N David Mermin and Herbert Wagner. “Absence of ferromagnetism or antiferromagnetism in one-or two-dimensional isotropic Heisenberg models”. In: *Physical Review Letters* 17.22 (1966), p. 1133 (cit. on p. 9).

[Nag+07] Máté Nagy, István Daruka, and Tamás Vicsek. “New aspects of the continuous phase transition in the scalar noise model (SNM) of collective motion”. In: *Physica A: Statistical Mechanics and its Applications* 373 (2007), pp. 445–454 (cit. on pp. 11, 37).

[Nag+15] Ken H Nagai, Yutaka Sumino, Raul Montagne, Igor S Aranson, and Hugues Chaté. “Collective motion of self-propelled particles with memory”. In: *Physical Review Letters* 114.16 (2015), p. 168001 (cit. on p. 21).

[Nar+17] Cesare Nardini, Étienne Fodor, Elsen Tjhung, et al. “Entropy production in field theories without time-reversal symmetry: quantifying the non-equilibrium character of active matter”. In: *Physical Review X* 7.2 (2017), p. 021007 (cit. on p. 79).

[NB99] MEJ Newman and GT Barkema. *Monte Carlo Methods in Statistical Physics*. Oxford University Press: New York, USA, 1999 (cit. on pp. 35, 86).

[New05] Mark EJ Newman. “Power laws, Pareto distributions and Zipf’s law”. In: *Contemporary physics* 46.5 (2005), pp. 323–351 (cit. on pp. 87, 88).

[RE10] Pawel Romanczuk and Udo Erdmann. “Collective motion of active Brownian particles in one dimension”. In: *The European Physical Journal-Special Topics* 187.1 (2010), pp. 127–134 (cit. on pp. 67, 69, 75).

[Rey87] Craig W Reynolds. “Flocks, herds and schools: A distributed behavioral model”. In: *ACM SIGGRAPH Computer Graphics* 21.4 (1987), pp. 25–34 (cit. on p. 4).

[RH10] Clewley RH. *PyCont*. 2010. URL: `http://www2.gsu.edu/~matrhc/PyCont.html` (cit. on p. 74).

[Ris84] Hannes Risken. “Fokker-planck equation”. In: *The Fokker-Planck Equation*. Springer, 1984, pp. 63–95 (cit. on p. 68).

[RL13] Maksym Romenskyy and Vladimir Lobaskin. “Statistical properties of swarms of self-propelled particles with repulsions across the order-disorder transition”. In: *The European Physical Journal B* 86.3 (2013), p. 91 (cit. on p. 45).

[Rom+12] Pawel Romanczuk, Markus Bär, Werner Ebeling, Benjamin Lindner, and Lutz Schimansky-Geier. “Active brownian particles”. In: *The European Physical Journal Special Topics* 202.1 (2012), pp. 1–162 (cit. on p. 16).

[RSG12] Pawel Romanczuk and Lutz Schimansky-Geier. “Mean-field theory of collective motion due to velocity alignment”. In: *Ecological Complexity* 10 (2012), pp. 83–92 (cit. on pp. 4, 67, 69, 70, 78).

[Sah+09] Arnab Saha, Sourabh Lahiri, and AM Jayannavar. “Entropy production theorems and some consequences”. In: *Physical Review E* 80.1 (2009), p. 011117 (cit. on p. 56).

[Say15] Hiroki Sayama. *Introduction to the modeling and analysis of complex systems*. Open SUNY Textbooks, 2015 (cit. on p. 1).

[Sei05] Udo Seifert. “Entropy production along a stochastic trajectory and an integral fluctuation theorem”. In: *Physical Review Letters* 95.4 (2005), p. 040602 (cit. on pp. 55–57).

[Sei08] Udo Seifert. “Stochastic thermodynamics: principles and perspectives”. In: *The European Physical Journal B-Condensed Matter and Complex Systems* 64.3 (2008), pp. 423–431 (cit. on pp. 56, 58).

[Sek98] Ken Sekimoto. “Langevin equation and thermodynamics”. In: *Progress of Theoretical Physics Supplement* 130 (1998), pp. 17–27 (cit. on p. 56).

[Sev+14] Francisco J Sevilla, Victor Dossetti, and Alexandro Heiblum-Robles. “Synchronization and collective motion of globally coupled Brownian particles”. In: *Journal of Statistical Mechanics: Theory and Experiment* 2014.12 (2014), P12025 (cit. on pp. 21, 22, 39, 64, 75).

[Shi+16] Pyoung-Seop Shim, Hyun-Myung Chun, and Jae Dong Noh. “Macroscopic time-reversal symmetry breaking at a nonequilibrium phase transition”. In: *Physical Review E* 93.1 (2016), p. 012113 (cit. on pp. 60, 62, 63).

[Shi+96] Naohiko Shimoyama, Ken Sugawara, Tsuyoshi Mizuguchi, Yoshinori Hayakawa, and Masaki Sano. “Collective motion in a system of motile elements”. In: *Physical Review Letters* 76.20 (1996), p. 3870 (cit. on p. 17).

[Sid+98] SW Sides, PA Rikvold, and MA Novotny. “Kinetic Ising model in an oscillating field: Finite-size scaling at the dynamic phase transition”. In: *Physical Review Letters* 81.4 (1998), p. 834 (cit. on p. 26).

[Sil+13] Jesse L Silverberg, Matthew Bierbaum, James P Sethna, and Itai Cohen. “Collective motion of humans in mosh and circle pits at heavy metal concerts”. In: *Physical Review Letters* 110.22 (2013), p. 228701 (cit. on p. 2).

[Sol+15] Alexandre P Solon, Hugues Chaté, and Julien Tailleur. “From phase to microphase separation in flocking models: The essential role of nonequilibrium fluctuations”. In: *Physical Review Letters* 114.6 (2015), p. 068101 (cit. on pp. 12, 13).

[Str11] Daniel Strömbom. “Collective motion from local attraction”. In: *Journal of Theoretical Biology* 283.1 (2011), pp. 145–151 (cit. on p. 5).

[Ton+05] John Toner, Yuhai Tu, and Sriram Ramaswamy. “Hydrodynamics and phases of flocks”. In: *Annals of Physics* 318.1 (2005), pp. 170–244 (cit. on p. 9).

[TT98] John Toner and Yuhai Tu. “Flocks, herds, and schools: A quantitative theory of flocking”. In: *Physical review E* 58.4 (1998), p. 4828 (cit. on p. 30).

[Vic+95] Tamás Vicsek, András Czirók, Eshel Ben-Jacob, Inon Cohen, and Ofer Shochet. “Novel type of phase transition in a system of self-driven particles”. In: *Physical Review Letters* 75.6 (1995), p. 1226 (cit. on pp. 5, 7, 11, 14).

[Vic08] Tamas Vicsek. “Universal patterns of collective motion from minimal models of flocking”. In: *Self-Adaptive and Self-Organizing Systems, 2008. SASO’08. Second IEEE International Conference on*. IEEE. 2008, pp. 3–11 (cit. on p. 3).

[VZ12] Tamás Vicsek and Anna Zafeiris. “Collective motion”. In: *Physics Reports* 517.3 (2012), pp. 71–140 (cit. on p. 3).

[Yeo+16] Joonhyun Yeo, Chulan Kwon, Hyun Keun Lee, and Hyunggyu Park. “Housekeeping entropy in continuous stochastic dynamics with odd-parity variables”. In: *Journal of Statistical Mechanics: Theory and Experiment* 2016.9 (2016), p. 093205 (cit. on pp. 59, 60).

[YM17] David Yllanes and M Cristina Marchetti. “How many dissenters does it take to disorder a flock?” In: *arXiv preprint arXiv:1701.05477* (2017) (cit. on p. 19).

List of Figures

List of Symbols

v_0	Self-propelled speed in the Vicsek model
R_0	Interaction range in the metric Vicsek model
η	Noise strength in the Vicsek model
Λ	Order parameter to describe collective motion
L	Linear size of a system
N	Number of particles in the system
Δt	Time step of the simulation
ρ	Particle density of the system
γ	Coefficient of friction in the Langevin equation
T	Temperature
D	Diffusion coefficient
$\boldsymbol{\xi}$	Vector of which the components are Gaussian white noise
k_B	Boltzmann constant
Γ	Coupling factor in the continuous-time Vicsek model
G	Binder cumulant
χ	Susceptibility of the order parameter
S	Entropy
$C_{\boldsymbol{vv}}$	Velocity autocorrelation function
$g(r)$	Radial distribution function
s	Rate of the entropy production per particle